Technical Physics Letters, Vol. 31, No. 9, 2005, pp. 719–721. Translated from Pis'ma v Zhurnal Tekhnicheskoĭ Fiziki, Vol. 31, No. 17, 2005, pp. 1–6.

Spatial Distribution of a Small Readily Ionized Additive in the Plasma of a Thermoelectronic Laser Energy Converter

V. A. Zherebtsov* and I. I. Kasikov

Leĭpunsky Institute of Physics and Power Engineering, State Scientific Center of the Russian Federation, Obninsk, Russia

** e-mail: zherebtsov@ippe.ru*

Received April 12, 2005

Abstract—The spatial distribution of a small additive of readily ionized atoms was studied in plasma of a continuous optical discharge (COD) between electrodes of a thermoelectronic laser energy converter. It is shown that the additive both in the equilibrium core of the COD and in nonequilibrium near-electrode plasma regions is driven toward the periphery of the discharge. As a result, the concentration of this additive at the electrodes is several orders of magnitude higher than that at the discharge center. © *2005 Pleiades Publishing, Inc.*

Introduction. Experimental [1] and theoretical [2–4] investigations of the process of thermoelectronic laser energy conversion showed that practically significant characteristics can be achieved provided that the converter has an emitter ensuring a thermoelectron current density on the order of 10^2 A/cm^2 and a collector with sufficiently low work function (~1.6 eV). In practice, the only means of satisfying these requirements is to introduce a readily ionized additive—for example, cesium vapor—into the interelectrode space filled with an inert gas.

Under the conditions of operation of a thermoelectronic laser energy converter, the temperatures of electrons and the heavy plasma components (ions and neutral species) in the central region (core) of a continuous optical discharge (COD) are nearly equal and the discharge plasma is virtually equilibrium. In the narrow (10^{-2} cm thick) near-electrode regions, an increase in the heat flux density carried by heavy particles and in the ion current density make the electron and ion temperatures different and lead to a drop in the density of charged particles, so that plasma in these regions becomes nonequilibrium [2, 5].

The presence of a readily ionized additive in the interelectrode space may, besides decreasing the work function of the emitter and collector, give rise to processes (both in the equilibrium COD core and in the nonequilibrium near-electrode regions) significantly influencing the laser energy conversion. In order to estimate the role of these processes, it is necessary to know the distribution of atoms and ions of the additive in the interelectrode space of the energy converter. This paper considers the features of this distribution on a qualitative level in the case of a small concentration of the additive, whereby it is possible to ignore its effect on the parameters of the working inert gas and electrons.

COD core. Let us consider an axisymmetric thermoelectronic laser energy converter with an inner electrode (emitter) of external radius r_1 and an outer electrode (collector) of internal radius r_2. The COD maintained in the interelectrode space is weakly inhomogeneous along the axis of symmetry coinciding with the z axis. Taking into account the high degree of ionization for the additive in the COD core, the radial profile of the density of additive ions can be described by the relation

$$\frac{n_{\mathrm{i}}^{(\mathrm{a})}}{n_{\mathrm{i}T1}^{(\mathrm{a})}} = \frac{n_{T1}}{n}\left(\frac{T_{T1}}{T}\right)^{1+k_{\mathrm{e}}^{(T)}} \exp\left[-\int_{r_{T1}}^{r} eJ_{T1}\frac{r_1}{r}\frac{1}{nTu_{\mathrm{e}}}dr\right], \quad (1)$$

where $n_{\mathrm{i}}^{(\mathrm{a})}$ is the ion density, n is the electron density, T is the plasma temperature, J is the electron flux density, $k_{\mathrm{e}}^{(T)}$ is the thermal diffusion ratio for electrons, u_{e} is the electron mobility, and e is the electron charge; the subscripts $T1$ and $T2$ refer to the quantities characterizing the near-emitter (inner) and near-collector (outer) boundaries of the COD core.

In the absence of a current via discharge, the additive ion concentration in the COD core decreases from its boundaries to the center in inverse proportion to the electron density and to approximately the square of the plasma temperature ($k_{\mathrm{e}}^{(T)} \approx 0.7$). Since the plasma temperature T_M at the COD core center weakly depends on the regime of operation of the energy converter, the ratio of the additive density at the COD core boundary to that at the core center increases with decreasing plasma temperature at the core boundary. An increase in the discharge current up to $J_{T1} \approx 400$ A/cm^2 does not produce qualitative changes in the distribution of additive ions in the COD core, albeit somewhat decreasing

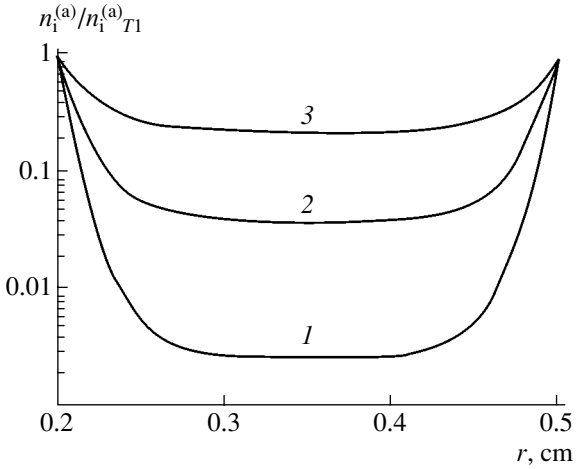

Fig. 1. Profiles of the relative density of cesium ion in the COD core calculated for $r_1 = 0.2$ cm, $r_2 = 0.5$ cm, $J_{T1} = 0$, and $T_{T1} = T_{T2} = 8000$ (*1*), 10 000 (*2*), and 12 000 K (*3*).

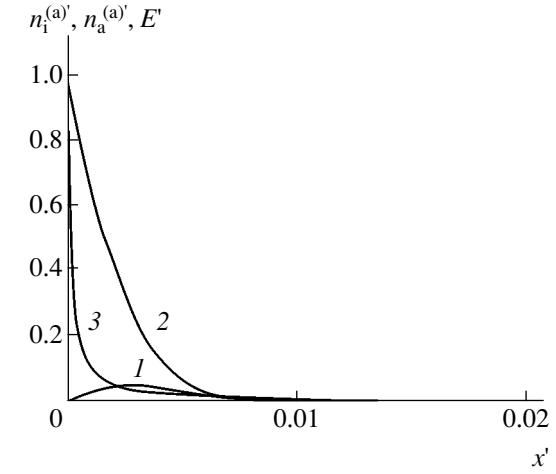

Fig. 2. Profiles of the (*1*) cesium ion density $n_i^{(a)'}$, (*2*) cesium atom density $n_a^{(a)'}$, and (*3*) electric field strength E' in the near-electrode region at $J_T = 0$.

their density at the core center and in the near-collector regions.

Figure 1 shows cesium ion density profiles in the core of a COD in argon at a pressure of 5×10^4 Pa and various plasma temperatures at the near-electrode core boundaries. As can be seen from these curves, the density of cesium ions in the middle of the COD core can be lower by one to two orders of magnitude than at the boundaries.

The near-electrode COD regions. The near-electrode COD regions will be described within the framework of a one-dimensional model [5], according to which these regions are flat and thin and the electron temperature variations within these regions are ignored. Let us consider the case of not very high temperatures of plasma at the COD core boundaries, whereby the main working gas in the near-electrode regions is weakly ionized. Distributions of the density of electrons (and the working gas ions) n, the temperature T of the heavy plasma components, and the electric field potential φ in the near-electrode regions have been recently studied in [5]. The flux densities of additive ions and neutrals obey the relations

$$\frac{dj_i^{(a)}}{dx} = -\frac{dj_a^{(a)}}{dx} = \Gamma_i^{(a)},$$
$$j_i^{(a)} = -D_i^{(a)}\frac{dn_i^{(a)}}{dx} - n_i^{(a)}u_i^{(a)}\frac{d\varphi}{dx}, \quad j_a^{(a)} = -D_a^{(a)}\frac{dn_a^{(a)}}{dx}. \qquad (2)$$

Here, $n_i^{(a)}$, $n_a^{(a)}$ are the concentrations and $j_i^{(a)}$, $j_a^{(a)}$ are the flux densities of the additive ions and atoms, respectively; $\Gamma_i^{(a)}$ is the additive ionization–recombination velocity [6]; $D_i^{(a)}$, $D_a^{(a)}$ are the diffusion coefficients for the additive ions and atoms, respectively; and $u_i^{(a)}$ is the mobility of additive ions.

At a boundary between the quasi-neutral plasma and the Langmuir layer ($x = 0$), Eqs. (2) are supplemented by the well known boundary conditions for the flux densities of additive ions and atoms [6] and for the total concentration of these ions and atoms, $n_1^{(a)} = n_{i1}^{(a)} + n_{a1}^{(a)}$. At the near-electrode COD core boundary ($x \longrightarrow \infty$), we use the condition of equilibrium for the additive. Here and below, the subscript "1" refers to the values of variables at the boundaries between the quasi-neutral plasma and the Langmuir layer and the subscript "T" refers to the near-electrode boundary of the COD core.

Using relations (2), we obtained a system of two equations of the first and second order, which were numerically solved using the Runge–Kutta method. The calculation procedure was analogous to that used in [5].

Figure 2 shows the characteristic profiles of the dimensionless concentrations of cesium ions ($n_i^{(a)'} = n_i^{(a)}/n_1^{(a)}$) and atoms ($n_a^{(a)'} = n_a^{(a)}/n_1^{(a)}$) and the electric field strength ($E' = (d\varphi/dx)/(d\varphi/dx)_1$) in the near-electrode regions of a thermoelectronic laser energy converter operating at an argon pressure of 5×10^4 Pa, electrode temperature of $T_E = 1000$ K, and a thermionic current of $J_E = 0$. The profiles are potted versus a dimensionless coordinate $x' = x/L_{iT}$, where L_{iT} is the ionization relaxation length for the working gas. The latter value, calculated under the conditions set at the near-electrode boundary of the COD core, characterizes the width of the near-electrode region [5]. As can be seen, the concentration of cesium atoms rapidly drops with increasing distance from the electrode, which is explained by intense ionization. The concen-

tration of ions first slightly increases and then exhibits decay. As a result, the total density of cesium ions and atoms at a distance from the electrode on the order of $10^{-2}L_{iT}$ decreases by two orders of magnitude, not reaching a level corresponding to the ionization equilibrium.

Thus, atoms desorbed from the electrode exhibit almost complete ionization in the near-electrode region with a thickness on the order of the ionization length for atoms of the additive ($L_{ia}^{(a)} \sim 10^{-2}L_{iT}$). The large potential difference between the ionization region and the COD core boundary prevents the penetration of ions into the COD core. The low (relative to $n_1^{(a)}$) density of ions in the ionization region is related to the large value of the electric field strength driving ions to the electrode. Switching on the electric field qualitatively changes the additive distribution in the near-electrode region. The density of cesium atoms drops rapidly with increasing distance from the electrode, while the density of cesium ions increases almost to $n_1^{(a)}$, after which both values reach the state of ionization equilibrium over a distance from the electrode on the order of $10^{-2}L_{iT}$.

The localization of a readily ionized additive on the periphery of discharge can be also observed under other discharge conditions, provided that the electron temperature is sufficiently high to ensure the intense ionization of additive atoms and the electric field formed by electrons and atoms of the main working gas is sufficiently strong.

Conclusions. We studied the spatial distribution of a small additive of readily ionized atoms in the COD plasma of a thermoelectronic laser energy converter filled with an inert gas. It is established that the additive both in the equilibrium core of the COD and in nonequilibrium near-electrode plasma regions is driven toward the periphery of the discharge and concentrated within a narrow near-electrode layer. As a result, the concentration of this additive at the electrodes is several orders of magnitude higher than that at the discharge center.

Acknowledgments. This study was supported in part by the Government of the Kaluga Region and the Russian Foundation for Basic Research, joint project no. 04-02-97218.

REFERENCES

1. N. P. Kozlov, A. V. Pekshev, Yu. S. Protasov, and V. I. Suslov, *Radiation Plasmadynamics* (Énergoatomizdat, Moscow, 1991), Vol. 1, pp. 462–498 [in Russian].
2. I. V. Alekseeva, A. P. Budnik, P. P. D'yachenko, *et al.*, Zh. Tekh. Fiz. **70** (11), 91 (2000) [Tech. Phys. **45**, 1462 (2000)].
3. A. P. Budnik and V. A. Zherebtsov, Zh. Tekh. Fiz. **71** (6), 60 (2001) [Tech. Phys. **46**, 704 (2001)].
4. I. V. Alekseeva, A. P. Budnik, and V. A. Zherebtsov, At. Energ. **96** (2), 98 (2004).
5. V. A. Zherebtsov, Teplofiz. Vys. Temp. **42** (4), 1 (2004).
6. F. G. Baksht, G. A. Dyuzhev, A. M. Martsinovskiĭ, B. Ya. Moĭzhes, G. E. Pikus, É. B. Sonin, and V. G. Yur'ev, *Thermoelectronic Converters and Low-Temperature Plasma* (Nauka, Moscow, 1973; Technical Information Center, US Dept. of Energy, Springfield, 1978).

Translated by P. Pozdeev

Technical Physics Letters, Vol. 31, No. 9, 2005, pp. 722–724. Translated from Pis'ma v Zhurnal Tekhnicheskoĭ Fiziki, Vol. 31, No. 17, 2005, pp. 7–12.

Transverse Magnetoconductivity in a Semiconductor Superlattice under the Stark Quantization Conditions

D. V. Zav'yalov, S. V. Kryuchkov, and E. I. Kukhar'

Volgograd State Pedagogical University, Volgograd, Russia

e-mail: sed@fizmat.vspu.ru

Received April 4, 2005

Abstract—The transverse magnetoconductivity has been calculated for a one-dimensional semiconductor superlattice under the action of an external quantizing electric field. The dependence of the conductivity on the electric and magnetic fields is analyzed and found to exhibit a strongly pronounced resonance character. The maximum values of conductivity are evaluated. © *2005 Pleiades Publishing, Inc.*

In recent years, processes related to charge transfer in low-dimensional structures have been given much attention. Of special interest in this respect are semiconductor superlattices (SLs), because these systems exhibit nonlinear electromagnetic properties even in relatively weak fields. Constant electric fields with strength above 10^3 V/cm may lead to the Stark quantization in SLs [1, 2]. Convincing experimental evidence for the existence of Stark–Wannier states in SLs was presented in [3].

A general theory of the electric conductivity in semiconductors under the action of arbitrary quantizing electric fields was developed in [4–6] and then further generalized so as to take into account the magnetic field [7]. It was established that the most interesting effects must be observed when the direction of the quantizing electric field coincides with the high-symmetry axes of a crystal. The interest in such effects was stimulated by the results of experimental investigations [8–10]. In particular, the electron–phonon resonance theoretically predicted by Bryxin *et al.* [4, 5] was experimentally observed in [10].

In experiment, however, it is very difficult to orient the electric field vector **E** strictly along an arbitrary preset direction, for example, along a certain crystallographic axis or an SL axis. There always exists at least a small transverse component of the applied electric field **E**. The problem of non-coincidence of the electric field vector and the crystal axis was formulated in [11] and it is still under discussion. For example, strong dependence of the spectrum of Bloch oscillations on the orientation of an applied electric field was pointed out in [12].

In this context, it was of interest to calculate the transverse magnetoconductivity in a semiconductor SL in the presence of a weak transverse electric field in addition to a strong longitudinal field parallel to the SL axis. The transverse field component can either be related to uncertainty of the field orientation along the SL axis or it can be specially applied so as to obey certain conditions. This field results in an electric current appearing in the transverse direction, that is, in the SL plane. It should be emphasized that, according to the results of theoretical analysis, the dependence of the transverse magnetoconductivity on the electric and magnetic fields exhibits a strongly pronounced resonance character. The problem of calculating the current along the SL axis in the presence of a longitudinal electric field and a magnetic field oriented at a certain angle to the SL axis was solved in [13], where Stark cyclotron resonance was predicted in this system.

Let us calculate the transverse magnetoconductivity for an SL with a period of d along the Oz axis in the presence of quantizing electric and magnetic fields applied along this axis and a small transverse electric field component: $\mathbf{E} = (E_\perp, 0, E_\parallel)$, where $E_\perp \ll E_\parallel$. We assume that electrons are scattered on the acoustic phonons and the following conditions are satisfied: $\omega_q \ll \omega_{st}, \Omega$, where ω_q is the acoustic phonon frequency, $\omega_{st} = edE_\parallel/\hbar$ is the Stark frequency, $\Omega = eH/mc$ is the cyclotron frequency, and H is the magnetic field strength. Using the method developed in [14], we can express the magnetoconductivity as

$$\sigma_\perp = \frac{2\pi e^2}{\hbar}\sum_{\mathbf{q}}\sum_{n\nu k_y n'\nu' k_y'}\sum\left[-\frac{\partial f}{\partial\varepsilon}\bigg|_{\varepsilon=\varepsilon_0}\right]\frac{\lambda^4}{2}(k_y - k_y')^2 \times \left|\langle n\nu k_y|W|n'\nu' k_y'\rangle\right|^2\delta[\hbar\Omega(n-n') + \hbar\omega_{st}(\nu-\nu')], \quad (1)$$

where $\varepsilon_0 = \hbar\Omega\left(n' + \frac{1}{2}\right) - \hbar\omega(\nu - \nu')$; $W = V_{\mathbf{q}}\exp(i\mathbf{q}\cdot\mathbf{r}) = \sqrt{\hbar\Lambda^2|\mathbf{q}|/2\rho sV}\exp(i\mathbf{q}\cdot\mathbf{r})$ is the operator of the elec-

tron–phonon interaction; ρ is the crystal density; s is the velocity of sound in the crystal; Λ is the constant of the deformation potential; $\lambda^2 = \hbar c/eH$; $n = 0, 1, 2 \ldots$; $\nu = 0, \pm 1, \pm 2 \ldots$; ε is the energy of the transverse motion of electrons; and $f(\varepsilon)$ is the electron distribution function with respect to this energy, describing the heating of electrons. In the general case, calculation of the latter distribution function requires a special consideration [5, 6]. However, under the condition $\omega_{st}\omega_q \ll (\Delta/\hbar)^2$, this function can be written as $f(\varepsilon) = A\exp(-\varepsilon/\theta)$, where Δ is the halfwidth of the conductivity miniband and θ is the effective electron gas temperature expressed in the energy units. The normalization condition yields $A = 2\pi n_0 d^3 \sinh(\beta x/2\theta)/x$, where $x = \hbar\Omega/\beta$, $\beta = \hbar^2/md^2$, and n_0 is the free electron density in the superconductor.

The square modulus of the matrix element calculated between two electron states can be written as [6, 15]

$$\left|\langle n\nu k_y|W|n'\nu' k_y'\rangle\right|^2 = \frac{2^n n!}{2^{n'} n!}|V_{\mathbf{q}}|^2\left(\frac{\lambda^2 q_\perp^2}{4}\right)^{|n-n'|} e^{-\frac{\lambda^2 q_\perp^2}{4}} \times \left[L_{n'}^{|n-n'|}\left(\frac{\lambda^2 q_\perp^2}{4}\right)\right]^2 J_{\nu-\nu'}^2\left(\frac{2\Delta}{\hbar\omega_{st}}\sin\frac{q_z d}{2}\right)\delta_{k_y - k_y', q_{y-}}, \quad (2)$$

where $q_\perp^2 = q_x^2 + q_y^2$ is the square of the transverse component of the wavevector of the phonon and $J_\gamma(z)$ is the Bessel function.

Let the lattice temperature be small ($kT \ll \hbar\Omega$), so that only a level with the minimum energy ($n' = 0$) be populated in the initial state. Using this approximation and taking into account smearing of the energy levels within $\hbar/\tau$, where τ is the electron mean free path time, we obtain the following expression for the transverse magnetoconductivity of the superlattice:

$$\sigma_\perp = \sigma_\perp^0 + \sigma_0\sqrt{x}\left(1 - \exp\left(-\frac{\beta}{2\theta}x\right)\right)S(x, z), \quad (3)$$

where

$$S(x, z) = \sum_{n=1}^{\infty} 2^n \int_{-\pi/2}^{+\pi/2} R_n(x, y)Q_n(x, y, z)dy, \quad (4)$$

$$R_n(x, y) = \frac{1}{n!}\Gamma\left(n + \frac{5}{2}\right){}_1F_1\left(-\frac{1}{2}; -n - \frac{3}{2}; \frac{y^2}{x}\right) - \frac{n+1}{2\sqrt{\pi}}\Gamma\left(-n - \frac{5}{2}\right)\left(\frac{y^2}{x}\right)^{n+5/2} {}_1F_1\left(n + 2; n + \frac{7}{2}; \frac{y^2}{x}\right), \quad (5)$$

$$Q_n(x, y, z) = \sum_{\gamma=-\infty}^{+\infty} J_\gamma^2\left(\frac{2\Delta}{\beta}\frac{\sin y}{z}\right)\exp\left(\frac{\beta}{\theta}z\gamma\right)\exp\left(-\frac{(xn + z\gamma)^2}{\alpha^2}\right), \quad (6)$$

$$\sigma_\perp^0 = \sigma_0\sqrt{x}\left(1 - \exp\left(-\frac{\beta}{2\theta}x\right)\right) \times \int_{-\pi/2}^{+\pi/2} R_0(x, y)J_0^2\left(\frac{2\Delta}{\beta}\frac{\sin y}{z}\right)dy, \quad (7)$$

$\alpha = \hbar/\beta\tau$, $x = \hbar\Omega/\beta$, $z = \hbar\omega_{st}/\beta$, $\gamma = \nu - \nu'$, $\Gamma(z)$ is the gamma function, ${}_1F_1(x; y; z)$ is the hypergeometric function, $y = q_z d/2$, and $\sigma_0 = 4e^2\Lambda^2 n_0\tau/\pi^{5/2}\hbar\theta\rho s d^2$.

The first term ($\sigma_\perp^0$) in expression (3) is a monotonic function of the magnetic and electric fields. This quantity grows with the magnetic field strength H. In ultimately strong magnetic fields ($\hbar\Omega/\beta \gg 1$), $\sigma_\perp^0$ is pro-

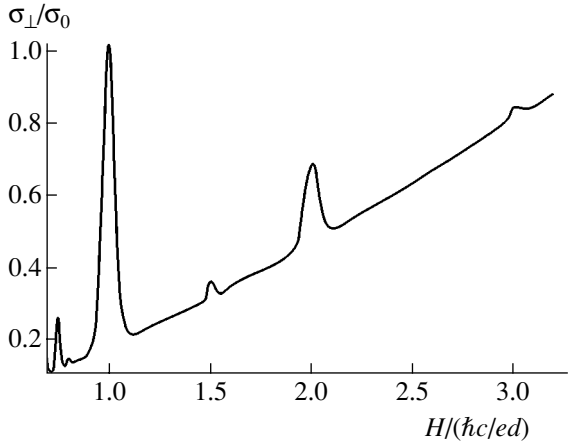

Fig. 1. A plot of the transverse conductivity versus magnetic field strength for an SL with $d \sim 3 \times 10^{-6}$ cm, θ ~ 0.05 eV, Δ ~ 0.01 eV, $\omega_{st} \sim 10^{13}$ s^{-1}, ρ ~ 5 g/cm^3, $s \sim 10^5$ cm/s, $n_0 \sim 10^{16}$ cm^{-3}, $\tau \sim 10^{-12}$ s, and Λ ~ 10 eV.

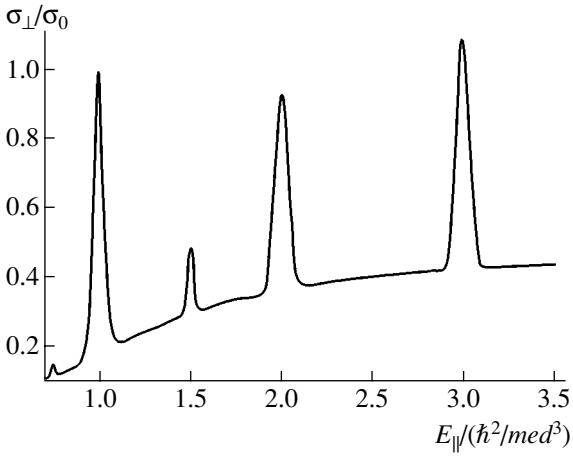

Fig. 2. A plot of the transverse conductivity versus longitudinal electric field strength for an SL with $d \sim 3 \times 10^{-6}$ cm, θ ~ 0.05 eV, Δ ~ 0.01 eV, Ω ~ 10^{13} s^{-1}, ρ ~ 5 g/cm^3, $s \sim 10^5$ cm/s, $n_0 \sim 10^{16}$ cm^{-3}, $\tau \sim 10^{-12}$ s, and Λ ~ 10 eV.

portion al top $H^{1/2}$. In contrast, in ultimately strong electric fields ($\hbar\omega_{st}/\beta \gg 1$), $\sigma_\perp^0$ ceases to depend on $E_\parallel$. The second term in expression (3) is responsible for the resonance part of the conductivity.

We have studied the behavior of function (3) by means of computer calculations. Figures 1 and 2 show the transverse conductivity as a function of the magnetic and electric field, respectively. As can be seen from Eqs. (3)–(6) and Figs. 1 and 2, the resonance behavior is observed when the ratio of the Stark and cyclotron frequencies is an integer. A numerical estimate for $d \sim 3 \times 10^{-6}$ cm, $\theta \sim 0.05$ eV, $\Delta \sim 0.01$ eV, $\rho \sim 5$ g/cm^3, $s \sim 10^5$ cm/s, $n_0 \sim 10^{16}$ cm^{-3}, $\tau \sim 10^{-12}$ s, and $\Lambda \sim 10$ eV is $\sigma_0 \sim 0.1$ (Ω m)$^{-1}$.

Acknowledgments. This study was supported jointly by the Volga Region Administration and the Russian Foundation for Basic Research, project no. 04-02-96505.

REFERENCES

1. G. Wannier, Phys. Rev. **125**, 1910 (1962).
2. J. Leo and A. MacKinnon, J. Phys.: Condens. Matter **1**, 1449 (1989).
3. K. Fujiwara, H. Schneider, R. Cingolani, and K. Ploog, Solid State Commun. **72**, 935 (1989).
4. V. V. Bryxin and Yu. A. Firson, in *Proceedings of the 10th International Conference on the Physics of Semiconductors, Boston, 1970*, pp. 767–771.
5. V. V. Bryksin and Yu. A. Firsov, Fiz. Tverd. Tela (Leningrad) **13**, 3246 (1971) [Sov. Phys. Solid State **13**, 2729 (1971)].
6. I. B. Levinson and Ya. Yasevichyute, Zh. Éksp. Teor. Fiz. **62**, 1902 (1972) [Sov. Phys. JETP **35**, 991 (1972)].
7. Yu. A. Firsov, *Polarons* (Nauka, Moscow, 1975) [in Russian].
8. V. N. Bogomolov and T. N. Pavlova, in *Multilayer Semiconductor Structures and Superlattices* (IPF AN SSSR, Nizhni Novgorod, 1984), pp. 53–62.
9. D. N. Mirlin, V. F. Sapega, and V. M. Ustinov, Fiz. Tekh. Poluprovodn. (St. Petersburg) **38**, 598 (2004) [Semiconductors **38**, 576 (2004)].
10. V. I. Sankin and A. V. Naumov, Pis'ma Zh. Tekh. Fiz. **16** (7), 91 (1990) [Sov. Tech. Phys. Lett. **16**, 281 (1990)].
11. S. A. Ktitorov, G. S. Simin, and V. Ya. Sindalovskiĭ, Fiz. Tverd. Tela (Leningrad) **18**, 1140 (1976) [Sov. Phys. Solid State **18**, 654 (1976)].
12. R. A. Suris, in *Future Trends in Microelectronics: Reflections on the Road to Nanotechnology*, Ed. by S. Luryi, J. Xu, and A. Zaslavsky (Kluwer Academic, Dordrecht, 1996), pp. 197–208.
13. F. G. Bass, V. V. Zorchenko, and V. I. Shashora, Pis'ma Zh. Éksp. Teor. Fiz. **31**, 345 (1980) [JETP Lett. **31**, 314 (1980)].
14. E. Adams and T. Holdstein, in *A Collection of Scientific Works: Quantum Theory of Irreversible Processes* (Inostrannaya Literatura, Moscow, 1961) [in Russian].
15. P. S. Zyryanov and M. I. Klinger, *Quantum Theory of Electron Transport Phenomena in Crystalline Semiconductor* (Nauka, Moscow, 1976) [in Russian].

Translated by P. Pozdeev

Technical Physics Letters, Vol. 31, No. 9, 2005, pp. 725–727. Translated from Pis'ma v Zhurnal Tekhnicheskoĭ Fiziki, Vol. 31, No. 17, 2005, pp. 13–18.

Dynamics of a Nonlinear Oscillator under Quasi-Periodic Drive Action

E. P. Seleznev* and A. M. Zakharevich

Saratov Branch, Institute of Radio Engineering and Electronics, Russian Academy of Sciences, Saratov, 410019 Russia
Saratov State University, Saratov, 410026 Russia
** e-mail: seleznev@sgu.ru*

Received February 16, 2005

Abstract—The dynamics of a nonlinear oscillator under quasi-periodic drive action is studied using the model of an excitable electric circuit with a nonlinear diode. In the space (plane) of control parameters, the system dynamics is described by the torus doubling lines and the lines of transition to a strange nonchaotic attractor, which connect the so-called torus doubling terminal points. The transition to chaos in this system proceeds either via the formation of a strange nonchaotic attractor or via a torus-to-chaos intermittency regime. © *2005 Pleiades Publishing, Inc.*

Investigations into the dynamics of nonlinear oscillators under quasi-periodic external action are of interest in the context of studying the features of the transition to chaos via breakage of quasi-periodic oscillations [1, 2]. On the passage from regular dynamics to chaos, such systems frequently feature an intermediate type of behavior corresponding to the formation of a strange nonchaotic attractor (SNA) [3–11]. One problem encountered in the experimental study of SNAs is how to identify them, and the small number of experimental investigations devoted to such systems is related to difficulties in this respect. Pikovsky and Feudel [9] proposed a method for the identification of SNAs which was related to bifurcations accompanying the change in the phase of action of the resonance cycles, whose rational rotation numbers belong to a sequence that converges to an irrational number. This method has been successfully verified in [10, 11], where a qualitative agreement between numerical and physical experiments was obtained.

Previous investigations of systems featuring SNAs were mostly performed using mathematical models in the form of maps [3–9] describing the dynamics of real systems within narrow regions in the space of control parameters. The structure of the space of control parameters presented in [10, 11] was also obtained in the case when the transition to chaos was realized in the course of variation of the amplitude of one partial action.

This Letter presents the results of our investigation into the structure of the space of control parameters of a nonlinear oscillator under a quasi-periodic action in the case when the system route to chaos is caused by the variation of all partial drive amplitudes.

The model system was an oscillatory circuit comprising a semiconductor diode excited by a biharmonic signal $E(t) = A_1\sin\omega_1 t + A_2\sin\omega_2 t$ [10, 11]. In order to realize the aim of this study, it was necessary that the frequencies $\omega_1 = 2\pi f_1$ and $\omega_2 = 2\pi f_2$ should fall within the main region of chaos for the driven oscillator [12, 13]. In this case, the ratio of the drive frequencies is close to unity. At the same time, in order to use the method of SNA identification proposed in [9], it is necessary that a sequence of rational numbers converging to an irrational number exist for the system under study. This situation can be realized using a product of the "golden section" and some rational multiplier (7/5 being a convenient choice).

Figure 1 shows the structure of the (A_1, A_2) drive amplitude plane for the drive frequency ratio $\frac{\omega_2}{\omega_1} = \frac{\sqrt{5}-1}{2}\frac{7}{5}$. Thick and thin solid lines indicate hard and soft bifurcations, respectively; open regions correspond to motions on the torus; differently gray-shaded regions denote regions of the existence of double toruses (*T*), SNAs (*NH*), and chaotic attractors (*H*); numbers indicate special points; and crosses indicate the torus doubling terminal (TDT) points. As can be seen from Fig. 1, the lines of transitions from torus doubling to SNAs originate and terminate at the TDT points and exhibit alternation.

Figure 2 shows a sequence of the stroboscopic sections with a period of $2\pi/\omega_1$ for the phase portrait projections onto the ($A_2\sin\omega_2 t$, i) plane (i is the diode current) constructed on motion along the *1–2* line in Fig. 1. Figure 2a corresponds to a smooth torus (point *1* in Fig. 1). On approaching a region of the existence of SNAs, the section shape begins to deform and, upon the transition to the SNA region, the section exhibits

1063-7850/05/3109-0725$26.00 © 2005 Pleiades Publishing, Inc.

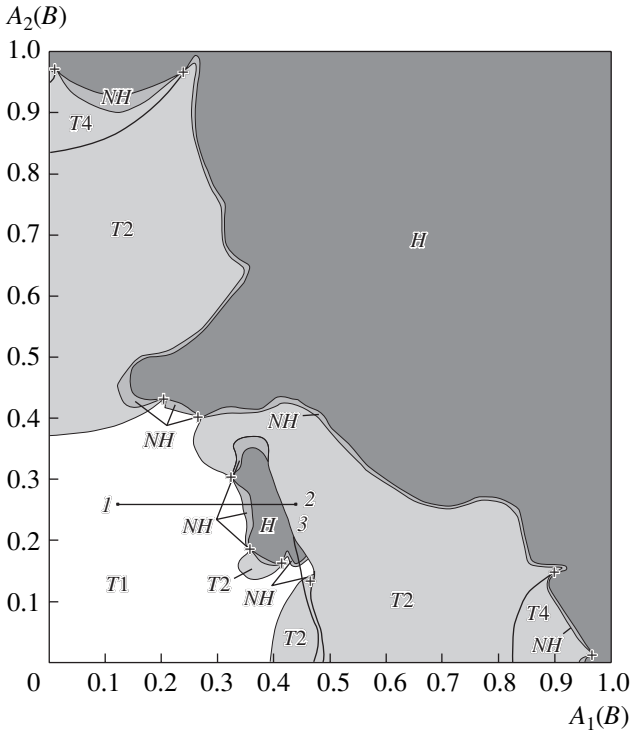

Fig. 1. The structure of the plane of control parameters for a nonlinear oscillator with diode under quasi-periodic biharmonic action with a drive frequency ratio of $\frac{\omega_2}{\omega_1} = \frac{\sqrt{5}-1}{2}\frac{7}{5}$ (see the text for explanations).

numerous breaks on various scales (Fig. 2b). Smearing of the section at the break points (reflecting the experimental noise) is indicative of a local instability in these regions of phase portraits. At the same time, there are regions free of such smearing, where the SNA is locally stable. Taking into account the particular choice of the projection, we may speak of a phase-dependent dynamics for the given attractor. According to the criterion proposed in [9], this dependence is confirmed by a rational frequency ratio of $\omega_2/\omega_1 = 13/15$ (determined from the corresponding sequence) and by a change in the phase of one partial drive component. As the A_1 value changes further, the system exhibits the transition to chaos, which is accompanied by smearing of the stroboscopic section of the phase portrait projection (Fig. 2c). Qualitatively the same transitions take place in all regions of the existence of SNAs and chaotic attractors. It should be noted that the transition from SNA to chaos cannot be clearly defined in experiment because of a complexity of each particular oscillation regime. For this reason, the boundary between the regions of existence of the SNAs and chaotic attractors is constructed using the observed power spectra. According to this method, the regime was considered chaotic if the noise pedestal on the analyzer screen was above –40 dB relative to the harmonic drive frequency ω_1 amplitude level.

On the passage from point *2* to the region of chaos (i.e., leftward along the *2–1* line in Fig. 1), we observe a different scenario of the route to chaos. In this case, the regime of oscillations observed at the boundary between order and chaos resembles an intermittency regime [14] in which a torus is the regular attractor. The appearance of such a regime is related primarily to the existence of a route to chaos via intermittency [15] in the initial system (a nonlinear harmonically driven oscillator). In the system under consideration, the situation is as follows. The plane of the control parameters

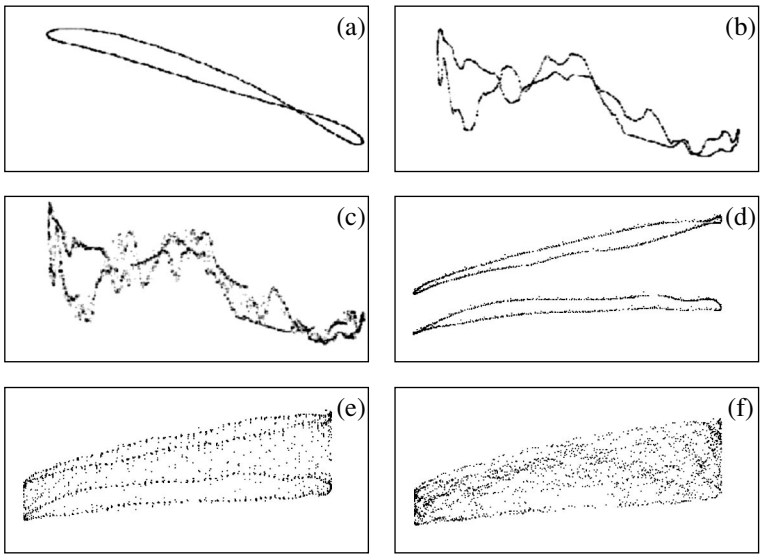

Fig. 2. A sequence of the stroboscopic sections with a period of $2\pi/\omega_1$ for the phase portrait projections onto the ($A_2\sin\omega_2 t$, i) plane (i is the diode current) for a nonlinear oscillator with diode under quasi-periodic biharmonic action (see the text for explanations).

contains a region bounded by the bifurcation lines (thick solid curves in Fig. 1), which features two stable toruses and one unstable torus. On the motion upward along the plane, these thick solid curves merge together at point *3*, thus forming a boundary between the double torus and chaos. Figure 2d shows a section corresponding to the double torus (with the values of parameters corresponding to point *2* in Fig. 1). Then, points not belonging to the double torus appear on the phase portrait section (Fig. 2e) corresponding to the boundary of the region of existence of this torus, which is reflected by short periods of chaotic oscillations on the diode current time series. On the passage from the boundary inward the region of chaos, the length of the chaotic phase increases, that of the laminar phase decreases, and their mixing leads eventually to the formation of a chaotic attractor whose section is presented in Fig. 2f.

Thus, qualitative identification of SNAs in the physical experiments with systems under quasi-periodic drive action can be performed using stroboscopic sections of the phase portrait projections onto the dynamic variable–drive phase plane. In these sections, the motion over a torus corresponds to a smooth closed curve; the motion on an SNA is represented by a closed curve containing smooth parts of local stability and breaks of local instability. The transition to chaos proceeds via the formation of an SNA or via a torus-to-chaos intermittency regime. It can be suggested that the obtained configuration of bifurcation lines on the plane of control parameters has a universal character and also takes place in other systems under quasi-periodic drive action.

Acknowledgments. This study was supported by the Russian Foundation for Basic Research (project no. 05-02-16305), the Program of Support for Post-Graduates by the Federal Agency on Education, and the U.S. Civilian Research and Development Foundation for the Independent States of the Former Soviet Union (CRDF Award No. REC-006).

REFERENCES

1. V. S. Afraimovich and L. P. Shilnikov, *Invariant Two-Dimensional Toruses, Their Breakdown and Stochasticity*, in *Methods of the Qualitative Theory of Differential Equations* (Gorki State University, Gorki, 1983); Am. Math. Soc., Ser. 2 **149**, 201 (1991).
2. V. S. Anishchenko, Zh. Tekh. Fiz. **56**, 225 (1986) [Sov. Phys. Tech. Phys. **31**, 137 (1986)].
3. C. Grebodgi, E. Ott, S. Pelican, and J. Yorke, Physica D **13**, 261 (1984).
4. M. Ding, C. Grebogi, and E. Ott, Phys. Rev. A **39**, 2593 (1989).
5. M. Ding, C. Grebogi, and E. Ott, Phys. Lett. A **137**, 167 (1989).
6. T. Nishikawa and K. Kaneko, Phys. Rev. E **54**, 6114 (1996).
7. B. R. Hunt and E. Ott, Phys. Rev. Lett. **87**, 254101 (2001).
8. R. Chacon and A. Martinez Garcia-Hoz, Europhys. Lett. **57**, 7 (2002).
9. A. Pikovsky and U. Feudel, Chaos **5**, 253 (1995).
10. B. P. Bezruchko, S. P. Kuznetsov, A. S. Pikovskiĭ, *et al.*, Izv. Vyssh. Uchebn. Zaved., Prikl. Nelin. Din. **5** (6), 3 (1997).
11. B. P. Bezruchko, S. P. Kuznetsov, and Ye. P. Seleznev, Phys. Rev. E **62**, 7828 (2000).
12. R. Buskirk and C. Jeffries, Phys. Rev. A **31**, 3332 (1985).
13. J. H. Baxter, M. F. Bocko, and D. H. Douglass, Phys. Rev. A **41**, 619 (1990).
14. C. Jeffries and J. Perez, Phys. Rev. A **26**, 2117 (1982).
15. H. Dadio, Prog. Theor. Phys. **70**, 879 (1983).

Translated by P. Pozdeev

Technical Physics Letters, Vol. 31, No. 9, 2005, pp. 728–731. Translated from Pis'ma v Zhurnal Tekhnicheskoĭ Fiziki, Vol. 31, No. 17, 2005, pp. 19–27.

Asymmetric Current Transfer in Isotype *n*-In_2Se_3/*n*-InSe Heterocontacts

S. I. Drapak and Z. D. Kovalyuk

Frantsevich Institute for Problems of Materials Science (Chernivtsy Department), National Academy of Sciences of Ukraine, Chernivtsy, Ukraine

e-mail: chimsp@unicom.cv.ua

Received February 17, 2005; in final form, May 6, 2005

Abstract—We have studied the mechanisms of current transfer and the capacitance–voltage characteristics of a radiation-resistant isotype *n*-In_2Se_3/*n*-InSe heterocontact in which the region depleted of major charge carriers is localized predominantly in a relatively low-ohmic semiconductor—the α-type In_2Se_3 with a large density of defects. The spectrum of the relative quantum efficiency of photoconversion in this structure depends on the thickness of the In_2Se_3 layer and on the geometry of illumination of the heterocontact. © *2005 Pleiades Publishing, Inc.*

Indium selenide (In_2Se_3) belongs to a broad class of layered semiconductors. The results of investigations of the physical properties of this compound in the form of both bulk single crystals and thin films are rather contradictory, which can be explained by a high defectness of the crystal structure and by the existence of various phases (α, β, δ, γ, κ), which are frequently present in the same sample [1]. It is the high density of defects in the crystal structure of In_2Se_3 that accounts for the stability of characteristics of this semiconductor under the action of ionizing radiation [2].

Investigations of the properties of double heterostructures in which In_2Se_3 was one of the component layers have been mostly devoted to the growth of films under various conditions on the surfaces of commercial semiconductors (see, e.g., [3]) or the structures in which this semiconductor (bulk single crystal or amorphous film) played the role of a low-ohmic electrode, while the space charge region occurred completely in a relatively high-ohmic component (equilibrium inversion layer) [4]. It was pointed out [5] that In_2Se_3/InSe structures obtained by thermal treatment of InSe substrates are practically insensitive to illumination.

This study was performed within the framework of a complex investigation devoted to elucidation of the possibility of using the α-type In_2Se_3 with a large density of defects in photoelectronics. Below we present the results of investigations of the electrical properties and photoelectric characteristics of photosensitive radiation-resistant isotype *n*-In_2Se_3/*n*-InSe heterocontacts. These data may be of interest for the optimization of the main photoelectric characteristics of the heterostructures based on In_2Se_3.

The heterocontacts were prepared using *n*-InSe and *n*-In_2Se_3 (E_g = 1.42 eV at room temperature) of the α-type with a hexagonal structure. The charge carrier density in the semiconductors, as determined from Hall effect measurements at T = 300 K, was ~10^{15} cm^{-3} for *n*-InSe and 4×10^{17} cm^{-3} for *n*-In_2Se_3. The heterojunctions were created by means of direct optical contact between semiconductor crystals. In order to reduce the influence of the layer of oxygen (playing the role of a dielectric gap [6]) adsorbed from air on the surfaces of both semiconductors, the heterocontacts were subjected to a short-term (20–40 s) compression at a load of $P \approx$ 70–100 kPa. The current-carrying contacts were formed by applying an In–Ga eutectic, followed by the fusion of indium on the In_2Se_3 side and by the vacuum deposition of pure indium on the InSe side. The obtained structures were characterized by current–voltage (*I–V*) characteristics and their temperature dependence, the capacitance–voltage (*C–V*) characteristics, and the spectrum of the relative quantum efficiency of photoconversion at room temperature.

Assuming that the electron affinities of InSe and In_2Se_3 are equal ($\chi_{InSe} = \chi_{In_2Se_3}$ = 3.6 eV [7], which was experimentally confirmed in [4]) and ignoring the possible influence of the surface states, we might have expected that the *I–V* curve of the isotype *n*-In_2Se_3/*n*-InSe heterocontact would be linear. However, the *I–V* curves of these structures measured in a broad temperature range have a shape typical of diode characteristics (Fig. 1, curves *1* and *2*). The forward direction of the *I–V* curve corresponds to the external bias connected with minus to the less high-ohmic component (*n*-In_2Se_3). This fact indicates that the region depleted of major charge carriers is localized predominantly in the relatively low-ohmic *n*-In_2Se_3, which is only possible provided that the semiconductor surface

1063-7850/05/3109-0728$26.00

has a potential determined by the surface acceptor states.

The *I–V* measurements showed that, in the region of forward bias voltages $V \le 0.2$ V, the dark current of the samples obeys the relation

$$I \sim \exp(eV/nkT), \quad (1)$$

with the diode coefficient $n > 2$ in the entire temperature range studied. The relatively high values of n show evidence for a tunneling-recombination mechanism of current transfer [8] in the structures studied.

The temperature dependence of the direct current at $V = 0.2$ V is rectified in coordinates of $\ln I$ versus $T^{-1/4}$ (Fig. 1, curve *4*), which corresponds to the Mott law [9],

$$I = I_0 \exp[-(T_0/T)^{1/4}], \quad (2)$$

$$T_0 = \beta(kg(E_F)a^3)^{-1}, \quad (3)$$

where $g(E_F)$ is the density of states at the Fermi level, k is the Boltzmann constant, a is the electron localization radius, β is a constant calculated using the percolation theory (in the three-dimensional case, $\beta = 0.21$). This behavior of the current as a function of the temperature shows evidence for hopping conductivity with variable jump length over states in the vicinity of the Fermi level in the depleted region localized in In_2Se_3 with a large density of defects. An analysis of the experimental data gave values of $T_0 = 4.57 \times 10^8$ K and $g(E_F) = 5.18 \times 10^{16}$ eV^{-1} cm^{-3}. According to [9], the percolation takes place within a narrow energy interval near the Fermi level, which can be evaluated using the formula

$$\Delta = -d\ln I/d(kT)^{-1}. \quad (4)$$

In our case, the average energy interval amounts to $\Delta = 0.07$ eV, which corresponds to the density of traps $N_t = g\Delta(E_F) = 3.63 \times 10^{15}$ cm^{-3}. Under such conditions, the expression for the tunneling-recombination current in the semiconductor with neglect of the energy distribution of local states and under assumption of the exponential surface potential is as follows [10]:

$$j_{t-r} = \frac{2kTW}{\varphi_0 - V} \times \frac{\omega N_t^2 \sigma_p \sigma_n v_{th} n_i^2 [\exp(eV/kT) - 1]}{\sigma_p \sigma_n v_{th}(n + n_1)(p + p_1) + \omega N_t[\sigma_n(n + n_1) + \sigma_p(p + p_1)]}. \quad (5)$$

Here, W is the thickness of the space charge region; σ_n and σ_p are the electron and hole trapping cross sections, respectively; $v_{th} = (3kT/m^*)^{1/2}$ is the thermal velocity of charge carriers; $\omega = \omega_0/N_t$ is the tunneling probability

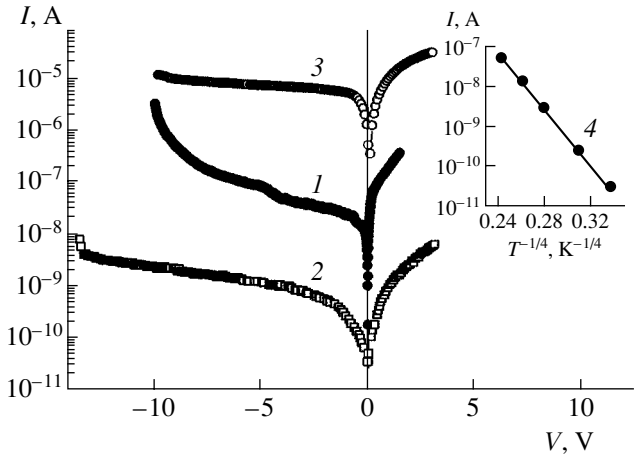

Fig. 1. The I–V curves of isotype n-In_2Se_3/n-InSe heterocontacts at $T = 285$ (*1*, *3*) and 77 K (*2*) measured (*1*, *2*) in the dark and (*3*) under illumination (~75–80 mW/cm^2) from the side of the In_2Se_3 layer having a thickness comparable with the space charge region thickness. Curve *4* in the inset shows the temperature dependence of the forward current at $V = 0.2$ V. Contact area, $S = 0.12$ cm^2.

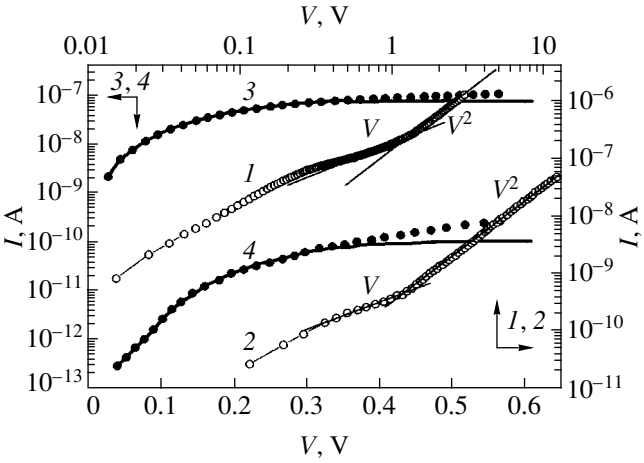

Fig. 2. Forward branches (*1*, *2*) and the experimental (points) and theoretical (solid curves) initial parts of the forward *I–V* curves (*3*, *4*) for isotype n-α-In_2Se_3/n-InSe heterocontacts at $T = 285$ (*1*, *3*) and 77 K (*2*, *4*). Contact area, $S = 0.12$ cm^2; InSe plate thickness, $L = 1.2$ mm.

per unit density of states; n_1 and p_1 are the densities of electrons and holes reduced to the local state level; and m^* is the effective mass.

Figure 2 (curves *3* and *4*) shows the results of theoretical calculations of the *I–V* curves using formula (5). As can be seen, the initial parts of these curves well agree with the experimental data plotted by black circles. In these calculations, a fitting parameter was the energy of localization of the deep centers, $E_t = E_v + 0.65$ eV, and the W value was replaced by $W–x$, representing a part of the depletion region in In_2Se_3 where the resistance was greater than that of InSe.

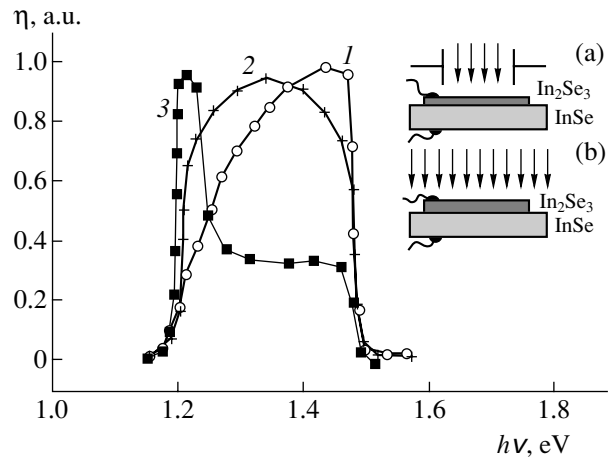

Fig. 3. The spectrum of the relative quantum efficiency of photoconversion in isotype n-In_2Se_3/n-InSe heterocontacts in the regime of (*1*) reverse and (*2*) forward bias with illumination through the In_2Se_3 layer having a thickness l comparable with the depleted region thickness W (inset (a)) and (*3*) with illumination over the entire geometric area (inset (b)) in the case when $l \gg W$; T = 285 K.

As the forward bias voltage is increased, the space charge region thickness W decreases until the resistance of this layer is comparable with that of a relatively high-ohmic component (InSe). Then, the total voltage drop across the structure is redistributed between this region (in In_2Se_3) and the InSe layer. For $V > 0.3$–0.4 V, the I–V curves of the n-In_2Se_3/n-InSe heterostructures (Fig. 2, curves *1* and *2*) are described by expressions typical of the space-charge-limited currents [11] in the regime of velocity saturation,

$$I = 2\varepsilon_2\varepsilon_0 v_s SV/L^2, \quad (6)$$

and in the regime of mobility saturation (trapless quadratic law),

$$I = 8\varepsilon_2\varepsilon_0\mu_n SV^2/L^3. \quad (7)$$

In these expressions, ε_2 is the permittivity of InSe, v_s is the saturation velocity, μ_n is the electron mobility, S is the heterocontact area, and L is the thickness of the high-ohmic layer. The L values calculated using the experimental data by formulas (6) and (7) were in good agreement with the thicknesses of InSe plates used in our samples.

The presence of regions of rapid current buildup in the characteristics of reverse-biased n-In_2Se_3/n-InSe heterocontacts observed for $|V| \sim 0.6$ and 5 V (Fig. 1, curve *1*) is characteristic of resonance tunneling via two serial tunneling-transparent barriers with the possible participation of a quantum well [12]. It is quite probable that the second barrier for electrons traveling from InSe to In_2Se_3 (the first barrier is a depleted region in InSe) is a layer of oxygen atoms (playing the role of a dielectric gap [6]) initially adsorbed on the surfaces of semiconductors. The influence of this layer on the electrical properties of the heterocontact under study confirms the conclusion [6] that the adsorbed oxygen cannot be eliminated from such structures by means of compression. The role of the quantum well in the heterocontact under study can be played by the inversion layer formed in the near-surface region of In_2Se_3 under reverse bias conditions. The illumination of such structures is equivalent to the direct displacement of the barrier into In_2Se_3 and leads to a decrease in the barrier height. In this case, the inversion layer is not formed even at a sufficiently large reverse bias and, hence, regions of rapid current buildup are no longer observed in the reverse branches of the I–V curves (Fig. 1, curve *3*).

The C–V curves of the isotype heterocontacts measured at a frequency of ≤5 kHz and 1 MHz have shapes typical of the low-frequency (LF) and high-frequency (HF) $C = f(V)$ functions for the metal–dielectric–semiconductor structures. In the region of forward bias voltages $V = 0.4$–12 V, both HF and LF capacitance exhibited saturation and was virtually completely shunted by the geometric capacitance of InSe. A decrease in the HF and LF capacitance C in the reverse-biased heterocontacts experimentally observed at $|V| \sim 8$–9 V was related to the attainment of a breakdown voltage [8], as confirmed by the results of I–V measurements. A significant increase in the reverse current (the so-called "soft" breakdown) observed at $|V| \approx 6$–7 V (Fig. 1, curve *1*) is characteristic of the electric breakdown in structures with a large density of defects, but it can also be related to the formation of surface conductivity channels in the defect structure of In_2Se_3 [8].

In the region of bias voltages V from –0.4 to 0.4 V, the HF capacitance as a function of the bias is well described by the expression typical of the surface-barrier structures [8]:

$$C = (e/2\varepsilon_1\varepsilon_0 n)^{1/2}(\varphi_0 - V)^{-1/2}, \quad (8)$$

where e is the electron charge; ε_1 and ε_0 are the permittivities of In_2Se_3 and vacuum, respectively; n is the density of the major charge carriers in In_2Se_3; and φ_0 is the barrier height. In our case, the latter value is equal to the surface potential ψ of In_2Se_3 with large density of defects. The barrier height φ_0, evaluated by extrapolating the $V = f(1/C^2)$ curve to the voltage axis, amounted to 0.64 ± 0.02 V. This estimate is in good agreement with the value of the current cutoff voltage (~0.6 V) determined from the room-temperature I–V curve. The total density of states at the interface was evaluated using the well-known relations [8] and amounted to $N_S \approx -Q_S/e \approx 2 \times 10^{12}$ cm^{-2}. The rather low value of N_S may indicate that the "maximum tight contact" is realized only at sites with a minimum density of "dangling" bonds (dominating in the surface relief of In_2Se_3 with large density of defects) rather than over the entire geometric area of the heterocontact.

The shape of the spectrum of photosensitivity of the n-In_2Se_3/n-InSe heterocontact strongly depends on the thickness l of the In_2Se_3 layer and on the geometry of illumination of the heterocontact (Fig. 3). This behavior is typical of so-called "nonideal" structures [8]. In fact, the photosensitivity of this heterocontact represents a superposition of contributions from the components, the polarities of which (determined by the external bias V) can be either added to or subtracted from the photovoltaic effect of the heterocontact proper. This may lead to inversion of the sign of photoresponse with respect to the regime of photogeneration at a zero bias voltage. For example, the maximum of photosensitivity $\eta(h\nu)$ of the reverse-biased heterocontacts illuminated through the layer of relatively wide-bandgap In_2Se_3 (Fig 3, inset (a)) in the case when l is comparable with the thickness of the depleted region is shifted toward shorter wavelengths (Fig. 3, curve *1*). In the forward-biased structure, the $\eta(h\nu)$ distribution is more "uniform" (Fig. 3, curve *2*). This behavior may indicate that the flat-band situation in forward-biased In_2Se_3 is practically never achieved: as the forward bias is increased, the W value decreases until the resistance of this region becomes comparable with that of the relatively high-ohmic component (dielectric gap or InSe plate). Then, the voltage drop is redistributed between the depleted region in In_3Se_3, dielectric gap, and InSe plate.

A decrease in W in the regime of forward bias leads to a 15–20% decrease in the absolute value of the photocurrent sensitivity in comparison to the case of reverse-biased heterocontacts. An increase in the In_2Se_3 layer thickness leads to a sharp decrease (up to a complete vanishing) in the photosensitivity in the case of illumination through this layer. The photosensitivity spectrum of n-In_2Se_3/n-InSe heterocontacts with a thick In_2Se_3 layer ($l \gg W$) illuminated over the entire geometric area (Fig. 3, inset (b)) is independent of the bias polarity (Fig. 3, curve *3*). In this case, the maximum of the $\eta(h\nu)$ curve is correlated with the spectrum of photosensitivity of InSe single crystals, and the appearance of photosensitivity in the short-wavelength range is related to the separation of photogenerated pairs in InSe by the field at the heterocontact.

In conclusion, it should be noted that the obtained data on the mechanism of current transfer in isotype n-In_2Se_3/n-InSe heterocontacts should be taken into account in applications including radiation-resistant photoconverters for the visible and near-IR spectral range and in the optimization of the design and photoelectric characteristics of structures based on α-type In_2Se_3 with a large density of defects.

REFERENCES

1. J. Wu, J. W. Ager, K. M. Yu, and W. Walukiewicz, Cond. Matter **1** (3), 1 (2003).
2. V. M. Koshkin and Yu. N. Dmitriev, *Chemistry and Physics of Compounds with Loose Crystal Structure* (Harwood Acad. Publ., Swizerland, 1994), Chem. Rev. Ser..
3. J. C. Bernede and S. Marsillac, Mater. Res. Bull. **37**, 1193 (1997).
4. S. I. Drapak, V. V. Netyaga, and Z. D. Kovalyuk, Pis'ma Zh. Tekh. Fiz. **28** (17), 8 (2002) [Tech. Phys. Lett. **28**, 711 (2002)].
5. V. P. Savchun and V. B. Kytsai, Thin Solid Films **361–362**, 123 (2000).
6. S. I. Drapak, M. O. Vorobets, and Z. D. Kovalyuk, Fiz. Tekh. Poluprovodn. (St. Petersburg) **39**, 633 (2005) [Semiconductors **39**, 600 (2005)].
7. J. Martinez-Pastor, A. Segura, J. L. Valdes, and A. Chevy, J. Appl. Phys. **62**, 1477 (1987).
8. S. Sze, *Physics of Semiconductor Devices* (Wiley, New York, 1981; Mir, Moscow, 1984).
9. N. F. Mott and E. A. Davis, *Electronic Processes in Non-Crystalline Materials* (Clarendon, Oxford, 1979; Mir, Moscow, 1982).
10. S. V. Bulyarskiĭ, V. K. Ionychev, and V. V. Kuz'min, Fiz. Tekh. Poluprovodn. (St. Petersburg) **37**, 117 (2003) [Semiconductors **37**, 115 (2003)].
11. M. Lampert and P. Mark, *Current Injection in Solids* (Academic Press, New York, 1970; Mir, Moscow, 1973).
12. G. G. Kareva, M. I. Vexler, I. V. Grekhov, and A. F. Shulekin, Fiz. Tekh. Poluprovodn. (St. Petersburg) **36**, 953 (2002) [Semiconductors **36**, 889 (2002)].

Translated by P. Pozdeev

Technical Physics Letters, Vol. 31, No. 9, 2005, pp. 732–734. Translated from Pis'ma v Zhurnal Tekhnicheskoĭ Fiziki, Vol. 31, No. 17, 2005, pp. 28–34.

Phase Transformations of Carbon Heated by a High-Power Current Pulse

N. I. Kuskova

Institute of Pulsed Processes and Technologies, National Academy of Sciences of Ukraine, Kiev, Ukraine

Received February 17, 2005

Abstract—The phase trajectories of carbon heated in various regimes by a high-power electric current pulse have been theoretically calculated. It is shown that diamond can be synthesized from a liquid phase in the regime of high-energy electric explosion. *© 2005 Pleiades Publishing, Inc.*

The investigations of processes involved in the modification of the properties of substances under the action of strong dynamic fields and currents provide a basis for the development of new promising technologies of obtaining superhard materials [1, 2]. The aim of this study was to assess the possibility of using high-power electric current pulses for heating cylindrical graphite conductors in a regime ensuring the graphite $\longrightarrow$ diamond phase transition.

According to the *P*–*T* phase diagram of carbon [3, 4], the graphite–diamond phase transition curve can be approximately described by the following expression:

$$P = 1.5 \times 10^9 + 2.1 \times 10^6 T. \quad (1)$$

This phase transition line terminates at the graphite–diamond–liquid phase triple point with the (P^*, T^*) coordinates.

For the direct graphite $\longrightarrow$ diamond phase transition, it is necessary that a carbon conductor heated by a high-power current pulse remain in the solid state. Therefore, the $\partial P/\partial T$ derivative along the phase trajectory during the entire period of heating must obey the following condition: $\partial P/\partial T > P^*/T^*$, where $P^* \approx 1.2 \times 10^{10}$ Pa and $T^* \approx 5 \times 10^3$ K. When a conductor is heated by a current pulse, the pressure and temperature grow with the current, and this condition can be written as

$$\frac{\partial P}{\partial T} \approx \frac{\Delta P}{\Delta T} \approx \frac{\partial P/\partial t}{\partial T/\partial t} > \frac{P^*}{T^*}. \quad (2)$$

The region of the phase diagram into which the substance falls upon the phase transition is characterized by the temperature (growing due to Joule heating) and the magnetic-field-induced pressure. For a slowly expanding cylindrical conductor, this pressure can be determined using the equation

$$\frac{\partial P}{\partial r} = -\frac{1}{2\mu r^2}\frac{\partial}{\partial r}(r^2 B_\varphi^2), \quad (3)$$

where μ is the magnetic permeability and B_φ is the magnetic induction. In a regime of homogeneous heating of the conductor, the magnetic induction is given by the formula

$$B_\varphi = \frac{\mu I}{2\pi a^2} r = \frac{\mu j r}{2}, \quad (4)$$

where I is the current, a is the conductor radius, and j is the current density.

The solution to Eq. (3) has the following form:

$$P(r) = P(a) + \frac{1}{4}\mu j^2 (a^2 - r^2), \quad (5)$$

where $P(a)$ is the pressure on the conductor surface. The rates of variation of the maximum pressure (at the conductor axis) and the temperature in a solid cylindrical conductor can be determined as

$$\frac{\partial P}{\partial t} \approx \frac{1}{2} a^2 \mu j \frac{\partial j}{\partial t} \approx a^2 \mu \frac{j^2}{2\tau}, \quad \frac{\partial T}{\partial t} \approx \frac{j^2}{\sigma \rho c}, \quad (6)$$

where τ is the time of current buildup to the maximum value, σ is the electric conductivity, ρ is the density, and c is the heat capacity.

Expressions (2) and (6) give the condition limiting from above the time of the current buildup to the maximum:

$$\tau < a^2 \mu \sigma \rho c \frac{T^*}{2P^*}. \quad (7)$$

Using the characteristics of graphite ($\rho = 2 \times 10^3$ kg/m^3, $\sigma = 2 \times 10^5$ S/m, and $c = 2 \times 10^3$ J/(kg K)), we obtain the inequality relating the conductor radius and the characteristic current buildup time τ at which the graphite $\longrightarrow$ diamond phase transition takes place:

$$\tau < 0.22 a^2. \quad (8)$$

1063-7850/05/3109-0732$26.00

On the other hand, the time of the current buildup to the maximum in a circuit containing inductance L and capacitance C is given by the formula $\tau \approx 0.5\pi\sqrt{LC}$. The thickness of a skin layer in a cylindrical conductor under the action of a current pulse can be expressed as $\delta = (\mu\sigma\omega/2)^{-1/2}$ [5], where $\omega = \tau^{-1}$. In order to provide for a homogeneous regime of heating, it is necessary that $\delta \gg a$. Using this inequality, the above relations, and the characteristics of graphite, we eventually obtain the condition $0.13a^2 \ll \tau < 0.22a^2$. An analysis of these inequalities shows that the graphite $\longrightarrow$ diamond phase transition in a cylindrical conductor heated in a homogeneous regime is practically impossible. In the case of a weakly inhomogeneous heating ($\delta \geq a$), we obtain $\tau \approx 0.2a^2$. For conductors of various radii, we obtain the following estimates: $a = 10^{-4}$ m, $\tau \approx 2 \times 10^{-9}$ s ($\sqrt{LC} \approx 10^{-9}$ s); $a = 10^{-3}$ m, $\tau \approx 2 \times 10^{-7}$ s; and $a = 10^{-2}$ m, $\tau \approx 2 \times 10^{-5}$ s. Evaluations showed that the direct graphite $\longrightarrow$ diamond phase transition at the axis of a thin cylindrical conductor requires the inductance and capacitance of the circuit to be very small. In the case of a thick conductor, the pressures and temperatures necessary for the diamond phase formation in the axial region according to Eq. (1) can be reached only at very high voltages (above 150 kV) applied to the conductor.

The existing level of technology does not allow a micron-grained diamond powder to be synthesized by means of the direct graphite $\longrightarrow$ diamond phase transition in a conductor heated by a high-power current pulse. Therefore, the current task is to find regimes of heating in which the diamond phase can be obtained from carbon in the other (gas or liquid) initial states.

Phase transitions of the solid $\longrightarrow$ liquid $\longrightarrow$ gas type in a current-heated conductor lead to electric explosions, which may also be accompanied by breakdown. We have performed experiments and realized various regimes of electric explosion for a graphite conductor in water or in a solar oil, which involved either the melting and evaporation of the conductor or only the sublimation of solid graphite (at a pressure not exceeding that at the graphite–liquid–gas phase triple point).

Figure 1 shows the typical oscillograms of the current and voltage observed during the electric explosions of graphite conductors in various regimes characterized by certain relations between the introduced energy W and the sublimation energy W_s: (a) $W = W_s$ (matched regime); (b) $W < W_s$ (delayed current regime); and (c) $W > W_s$ (undelayed current regime). In the case of electric explosions in the matched and undelayed current regimes, the surface layer of the conductor is sublimated, while the axial region is melted and converted into the liquid state. In the delayed current regime, the entire conductor (with the given parameters) exhibits sublimation.

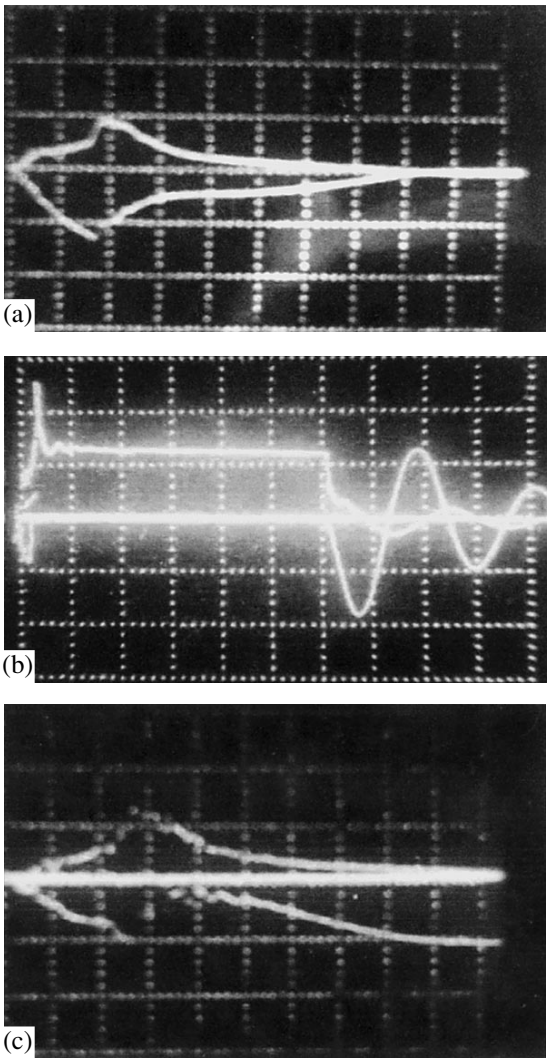

Fig. 1. Typical oscillograms of the current (lower curves) and voltage (upper curves) observed during the electric explosions of graphite conductors in various regimes: (a) $W = W_s$ (matched regime, sweep period $\tau = 1$ μs); (b) $W < W_s$ (delayed current regime, $\tau = 20$ μs); and (c) $W > W_s$ (undelayed current regime, $\tau = 0.5$ μs).

In order to construct the phase trajectories of carbon during the electric explosion in various regimes, we calculated the thermodynamic parameters (pressure and temperature) in the axial region of a cylindrical conductor. The phase trajectory represented by curve *1* in Fig. 2 corresponds to the direct graphite $\longrightarrow$ diamond phase transition considered above and in [6, 7]. The trajectories leading to graphite $\longrightarrow$ diamond phase transitions upon electric explosion in the undelayed and delayed current regimes are depicted by curves *2* and *3*, respectively. A high pressure in the axial liquid region of the semiconductor exhibiting electric explosion in the high-energy ($W \gg W_s$) undelayed current regime is achieved due to the reactive compression produced by the evaporation wave propagating from the surface

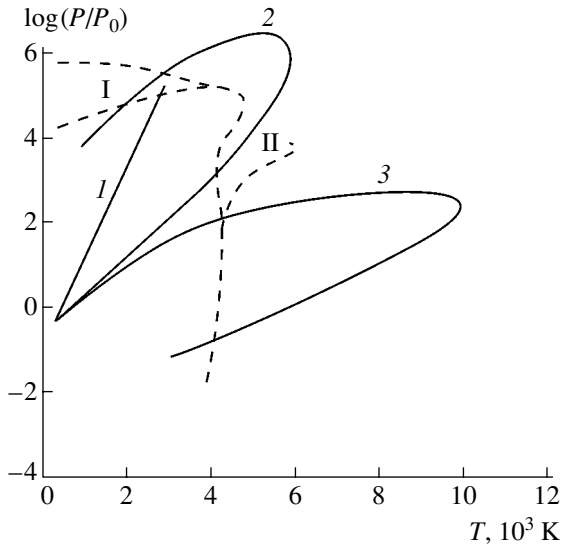

Fig. 2. The phase diagram and the phase trajectories of carbon in the axial region of a cylindrical conductor exhibiting (*1*, *2*) graphite ⟶ diamond and (*3*) graphite–fullerene phase transitions in the course of pulsed current-induced heating: (I) diamond; (II) liquid carbon; dashed curves show the lines of phase equilibria.

inward the conductor and a shock wave propagating from the discharge channel upon repeated breakdown.

The results of preliminary X-ray diffraction measurements of the products of electric explosion in the undelayed current regime with a fast evaporation of the conductor suggested that a diamondlike phase can be present in a total amount not exceeding 10 wt %. This was confirmed by the quite good coincidence of the positions of experimental interference maxima with the corresponding theoretical values for diamond. The X-ray diffraction data (reflection intensities *J* and calculated interplanar spacings *d*) for samples 1 and 2 synthesized via electric explosion in the undelayed current regime with the specific introduced energies differing by 15 MJ/kg in comparison to the values for a reference diamond powder are presented in the table.

X-ray diffraction data (reflection intensities *J* and calculated interplanar spacings *d*) for two products synthesized via electric explosion in undelayed current regimes with different specific introduced energies in comparison to analogous data for a reference diamond powder

Sample 1		Sample 2		Diamond	
J, %	*d*, Å	*J*, %	*d*, Å	*J*, %	*d*, Å
21	2.0704	30	2.0713	100	2.06
17	1.2606	20	1.2578	27	1.261
6	1.0717	8	1.0690	16	1.0754
3	0.8924	5	0.8910	7	0.8916
3	0.8155	2	0.8173	15	0.8182

The products of the electric explosion of graphite conductors in a solar oil obtained in the delayed current regime contain, according to the X-ray diffraction and spectroscopic data, soot and fullerenes [8, 9]. Graphite was not detected in the products obtained in the undelayed and delayed current regimes. The product obtained upon electric explosion in the matched current regime consists of finely dispersed graphite particles. Therefore, this regime represents a reversible thermodynamic process.

To summarize, we have demonstrated that the electric explosion of graphite conductors in high-energy regimes makes possible the synthesis of diamond (in an amount not exceeding 10 wt % of the initial material weight) from the liquid phase of carbon. Conditions realized in the course of such electric explosion fall within the range of physicochemical parameters ensuring a high probability of the spontaneous formation of new carbon phases. Therefore, further investigations into the structural transitions in carbon conductors heated by high-power current pulses are highly promising.

REFERENCES

1. A. I. Savvatimskiĭ and V. E. Fortov, High Temp. High Press. **30**, 377 (1998).
2. O. A. Bannykh, O. G. Epachintsev, and A. S. Zubchenko, Dokl. Akad. Nauk **354**, 628 (1997).
3. E. N. Marmer, *Carbon and Graphite Materials: A Handbook* (Metallurgiya, Moscow, 1985) [in Russian].
4. F. P. Bundy, W. A. Basset, and M. S. Weathers, Carbon **34**, 141 (1996).
5. S. I. Tkachenko and N. I. Kuskova, J. Phys.: Condens. Matter **11**, 2223 (1999).
6. V. V. Ivanov, V. N. Korobenko, S. N. Paranin, *et al.*, Dokl. Akad. Nauk SSSR **239**, 838 (1978) [Sov. Phys. Dokl. **23**, 269 (1978)].
7. A. V. Bushman, V. S. Vorob'ev, A. D. Rakhel', and V. E. Fortov, Dokl. Akad. Nauk SSSR **315**, 1124 (1990) [Sov. Phys. Dokl. **35**, 1079 (1990)].
8. L. Z. Boguslavskiĭ, I. P. Guk, N. I. Kuskova, *et al.*, Elektron. Obrab. Mater., No. 4, 30 (2002).
9. L. Z. Boguslavskiĭ, A. I. Vovchenko, and N. I. Kuskova, Elektron. Obrab. Mater., No. 6, 25 (2002).

Translated by P. Pozdeev

Technical Physics Letters, Vol. 31, No. 9, 2005, pp. 735–737. Translated from Pis'ma v Zhurnal Tekhnicheskoĭ Fiziki, Vol. 31, No. 17, 2005, pp. 35–41.

Jumplike Variation of the Contact Area between Randomly Rough Surfaces

A. É. Filippov[a] and V. L. Popov[a,b]

[a] *Donetsk Physicotechnical Institute, Donetsk, Ukraine*
[b] *Berlin Technical University, Berlin, Germany*

Received April 28, 2005

Abstract—A numerical model of the contact between two solid surfaces with statistically random roughness has been considered. As the two surfaces are brought in contact and pressed against each other, the real contact area initially increases in proportion to the normal force, with a proportionality factor dependent on the spectral density of the surface profile. As the pressing force grows further, the contact area exhibits two sequential jumps. This behavior is universal, being manifested for various spectral densities of the surface roughness in both two- and three-dimensional cases. The physical reasons for the observed features and their role in the mechanics of contact between soft materials (rubber, biological tissues) are discussed. The effect can be used for creating new adhesive systems capable of exhibiting strong adhesion upon application of a critical pressing force. © *2005 Pleiades Publishing, Inc.*

Introduction. Surface roughness plays a significant role in many technical systems involving friction, wear, adhesion, sealing and self-adhesive layers, and electric and thermal contacts [1]. When bodies with rough surfaces are brought in contact, the "real" contact area is usually much smaller than the "nominal" value. The real contact area determines the electric and thermal resistance of the junction. The size of microscopic contacts and the mechanical stresses developed in such contacts determine the particle size in wear products, thus influencing the wear life of materials. The real contact area also plays a decisive role in the process of friction. On a microscopic level, the friction can be considered as the rupture of microscopic bonds between contacting surfaces. According to these notions, the strength of these bonds and, hence, the friction force must be approximately proportional to the real contact area.

The dependence of the real contact area on the normal force has been considered by many researchers. In the simplest model, a rough surface appears as a regular sequence of spherical protrusions. The total force in this model is the sum of identical local forces, which can be calculated using the Hertz theory [2]. The area of each microscopic contact (and the total contact area determined as a product of this local value and a constant number of contacts) obeys the relation $A \sim F^{2/3}$. This formula contradicts both direct experiment and the Amonton law, according to which the friction force is approximately proportional to the normal force. Greenwood and Williamson [3] eliminated this discrepancy by taking into account that the roughness of real surfaces is random rather than regular. They demonstrated that, even for the same radius of curvature, allowance for a random distribution of the height of microscopic contacts leads to almost linear (with logarithmic corrections) relationship between the contact area and the normal force.

Persson *et al.* [1] showed that the contact area of rough surfaces, characterized by a random distribution of the microscopic contacts with respect to both height and curvature radii, is proportional to the normal pressing force. However, a necessary prerequisite was a small real contact density as compared to the nominal value. In this study, we go beyond this approximation and consider the dependence of the contact area on the normal forces in the entire range of their variation up to a level where the two surfaces are in contact at all points.

Model. Let us consider a simplified discrete model of elastic bodies, representing a series of equidistant material points elastically bound to a rigid surface possessing a preset geometric profile. The surface profile was generated so as to provide that both the spectral density and the height distribution of roughnesses would correspond to the typical experimental data [1]. The surface was generated by stochastically throwing Gaussians with randomly distributed peak heights and widths.

Figure 1 shows the typical spectral density and the distributions of height $z(x, y)$ (solid profile in the inset to Fig. 1) and local peaks. The asymmetry of the distribution function $P = P(z)$ corresponds to the asymmetry of peaks and wells on a real surface [1], which was reproduced by setting various positive and negative (on the average) amplitudes of randomly thrown Gaussians.

1063-7850/05/3109-0735$26.00 © 2005 Pleiades Publishing, Inc.

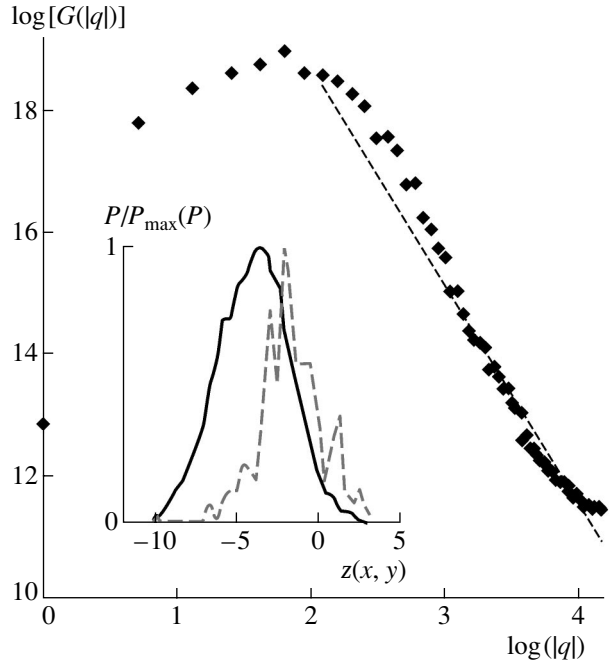

Fig. 1. The spectral density of roughness for a model surface generated by throwing Gaussians as described in the text. The dashed line has a slope corresponding to the spectral density of most real surfaces (possessing a fractal dimension of $D_f = 2.2$). The inset shows the distributions of peak heights $z(x, y)$ (solid curve) and local peaks (dashed curve) for the same model surface.

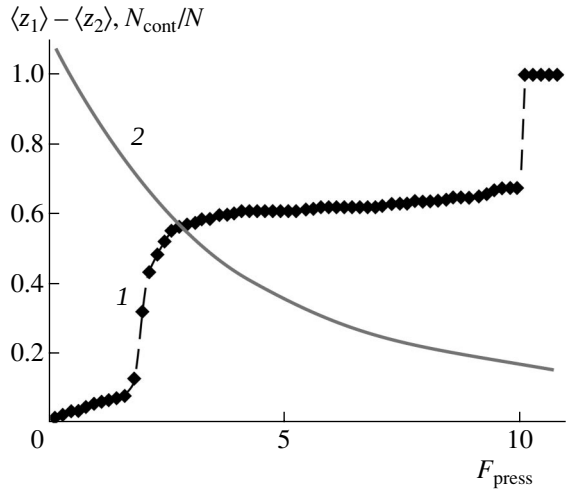

Fig. 2. A plot of the (*1*) relative contact length N_{cont}/N and (*2*) average distance between surfaces $\langle z_1\rangle - \langle z_2\rangle$ versus normal pressing force F_{press} in the 2D model.

The equations of dynamics for the model formulated above can be written as

$$\begin{aligned} \partial z_1/\partial t &= K_z(w_1(x, y) - z_1(x, y)) - F_{rep}; \\ \partial z_2/\partial t &= K_z(w_2(x, y) - z_2(x, y)) + F_{rep} - P_{ext}, \end{aligned} \quad (1)$$

where K_z is the elastic constant of the bonds between mobile elements ("material points") of the upper (subscript 2) and lower (subscript 1) surfaces, occurring in positions with the coordinates $z_{2,1}(x, y)$, and the fixed seeding forms of the same surfaces $w_{2,1}(x, y)$. The external pressure P_{ext} applied only to the upper body.

The effect of the internal (bulk) layers of the system on the mobile surface elements at the points $z_{2,1}(x, y)$ is taken into account by introducing a "soft" repulsion wall $F_{rep} = C\exp[z_1(x, y) - z_2(x, y))/\lambda]$ with amplitude C and a characteristic width λ of the interaction buildup in depth of the material.

Since we are interested only in quasistatic transformations of the contacting surfaces (their inertia is insignificant), the consideration can be restricted to a simplified (overdamped) variant of the equations of motion (1).

Contact area as a function of the pressing force. We studied both two- (2D) and three-dimensional (3D) models. In the 2D case, the role of the contact "area" is played by the contact length. Figure 2 shows a plot of this length versus applied normal pressing force F_{press}. At small pressing forces, the contact length is proportional to the force. When the normal force reaches a certain critical level, the contact length exhibits a jump. As the pressing force grows further, the contact length smoothly increases and then exhibits a second jump upon which the contact "area" becomes virtually equal to the nominal total value. This behavior with jumps is universal, being manifested for various spectral densities of the surface roughness.

A similar pattern is observed in the 3D case. Figure 3 shows a plot of the contact area versus applied normal pressing force F_{press} for the 3D model. As can be seen, the same characteristic features—linear behavior at small pressing forces and two subsequent jumps—are observed in this case as well. This phenomenon has not been previously reported in the literature.

The physical reasons for the observed jumps are as follows. In accordance with the well-known theory [1], when the pressing load is small, the surfaces are transformed insignificantly and contact each other in a very restricted number of points. As the pressing force is increased, the number of contact points slowly grows as well. The combined effect of the surface transformation in the vicinity of contacting local maxima and the appearance of additional lower peaks also entering into contact lead to virtually linear growth of the total contact area as a function of the applied force. However, the peak height distribution has a clearly pronounced maximum. When the pressing force becomes sufficiently large, the surface is transformed so that a large fraction of points from the vicinity of the distribution maximum are brought in contact. As a result, the contact area exhibits a nonlinear growth, which is determined by the structure of the roughness height distribution in the vicinity of the distribution maximum, rather than by the statistics of scatter of the separate features.

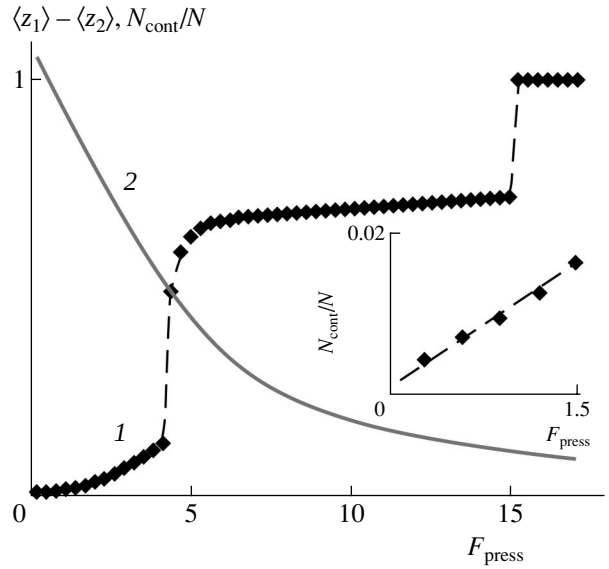

Fig. 3. A plot of the (*1*) relative contact area N_{cont}/N and (*2*) average distance between surfaces $\langle z_1 \rangle - \langle z_2 \rangle$ versus normal pressing force F_{press} in the 3D model. The inset shows a linear behavior in the region of small pressing forces.

The phenomenon of rapid (nonlinear or practically jumplike) change in the contact area is especially important for systems in which the full contact in the elastic region is really accessible. This is possible, for example, in elastic materials such as rubber and biological tissues [4, 5]. A jumplike change in the contact area must lead to the corresponding abrupt variation in the adhesion and in the friction force upon reaching the critical pressing force. After the second jump, the contact area is virtually equal to the total surface area ($N_{cont}/N \sim 1$). This phenomenon is important for sealing contacts, in which the optimum sealing effect is achieved upon reaching a certain critical pressing force. Both jumps can be used for the development of adhesive materials with discretely controlled adhesion and for designing and calculating sealing contacts.

Acknowledgments. The authors gratefully acknowledge support from Deutsche Forschungsgemeinschaft.

REFERENCES

1. B. N. J. Persson, O. Albohr, U. Tartaglino, *et al.*, J. Phys.: Condens. Matter **17**, R1 (2005).
2. L. D. Landau and E. M. Lifshitz, *Course of Theoretical Physics*, Vol. 7: *Theory of Elasticity* (Nauka, Moscow, 1987; Pergamon, New York, 1986).
3. J. A. Greenwood and J. B. P. Williamson, Proc. R. Soc. London, Ser. A **295**, 300 (1966).
4. B. N. J. Persson and S. Gorb, J. Chem. Phys. **119**, 11437 (2003).
5. A. K. Geim, S. V. Dubonos, I. V. Grigorieva, *et al.*, Nature (London) **2**, 41 (2003).

Translated by P. Pozdeev

Technical Physics Letters, Vol. 31, No. 9, 2005, pp. 738–740. Translated from Pis'ma v Zhurnal Tekhnicheskoĭ Fiziki, Vol. 31, No. 17, 2005, pp. 42–47.

Photoelectron Emission Induced by Radiation of a Nitrogen Laser

E. M. Gushchin, N. A. Mikhanchuk*, and S. G. Pokachalov

Moscow Engineering Physics Institute (State University), Moscow, 115409 Russia

** e-mail: mikhanchuk@mail.ru*

Received April 5, 2005

Abstract—The photoionization of various technological materials under the action of a pulsed nitrogen laser has been studied. It is shown that the photoeffect is produced mostly via the mechanism of two-photon ionization. The maximum photoionization efficiency was observed for a magnesium cathode. © *2005 Pleiades Publishing, Inc.*

Previously, we demonstrated [1] that radiation of a molecular nitrogen (N_2) laser produces significant photoelectron emission from metals, semiconductors, and dielectrics, even if the work function of the irradiated material exceeds the laser quantum energy ($h\nu$ = 3.68 eV). These observations can be explained either by a single-photon mechanism, whereby "hot" electrons are emitted from the "tail" of the Maxwell distribution, or by a two-photon surface ionization. In the former case, the energy of the emitted electron is $Q \sim E_l$, while in the second case, the photoelectron energy is

$$Q \sim \frac{E_l^2}{T_l S}, \qquad (1)$$

where E_l is the laser pulse energy, T_l is the pulse duration, and S is the irradiated surface area.

This Letter presents the results of experimental investigations of the electron emission from various materials (in particular, those used in charged particle detectors) exposed to radiation of a pulsed N_2 laser (LGI-503 type) with the following characteristics: pulse duration, $T_l \approx 8$ ns; pulse energy, $E_l \leq 50 \pm 0.5$ μJ; beam divergence, $\varphi < 1.5$ mrad.

The experiments were performed using a setup based on a plane-parallel, two-electrode photodiode ionization chamber intended for the investigation of correlations between the physical and biological characteristics of various chemical compounds [2]. The ionization chamber comprised a magnesium disk cathode and a grid anode made of 100-μm-thick nichrome wire. Both electrodes had a diameter of 60 mm, and the interelectrode distance was d = 10 mm. The laser beam entered into the ionization chamber through a quartz window, passed through the grid anode, and struck the cathode perpendicularly to its surface. A lens with a focal distance of F = 50 mm mounted in front of the entrance window could be moved along the laser beam axis, which allowed the laser-irradiated spot area to be controlled.

The samples of materials studied were placed on the cathode surface in the vicinity of the disk center. The entrance lens could also be moved in the transverse direction, which made it possible to measure the charge emitted both from the sample surface and from the magnesium cathode. Prior to measurements, the surfaces of the cathode and the samples were processed only by mechanical methods; therefore, in most metal samples we probably studied a surface covered by a natural oxide film rather than the corresponding pure metals.

We studied the photoelectron emission from samples both into vacuum ($<10^{-4}$ Torr) and into pure carbon dioxide. The output signal from the ionization chamber was fed directly to the input of a 1-MΩ S1-117 oscillograph with a sensitivity of 100 μV. The electric field strength in the interelectrode gap was E = 100 V/cm.

As can be seen from the data presented in Fig. 1 (curve *1*), a decrease in the distance L from the laser beam focus to the sample surface leads to an initial increase in the signal amplitude Q followed by a drop. At $L \approx 0$, the signal amplitude sharply grows (by 2–3 orders of magnitude) and exhibits significant fluctuations (reaching ~100% of the signal amplitude). In order to understand the behavior of $Q(L)$, it is necessary to take into account that the focus diameter $d_f \sim \varphi F$ does not exceed 70–80 μm. For the N_2 laser used, this corresponds to a power density of up to 400 MW/cm^2. As the focus approaches the photocathode, the sample surface exhibits local heating that leads to gas evolution. The

1063-7850/05/3109-0738$26.00

formation of such a gaseous microcloud leads to a decrease in the signal amplitude because of the scattering of photoelectrons on gas molecules and the loss of scattered photoelectrons on the cathode [3]. As long as the cloud size along the electric field lines is small, the photoelectron mean free path (with respect to the ionization events) exceeds the average distance between gas molecules, and the probability of multiplication processes is insignificant. For $L \longrightarrow 0$, the temperature on the photocathode surface and the intensity of gas evolution increase. These factors lead to an increase in the probability of impact ionization and, accordingly, in the signal amplitude. Instability of the gas pressure in the local spatial region near the cathode leads to instability of the response.

The results of a microscopic examination of the sample surface in the vicinity of the point of laser radiation focusing revealed characteristic erosion spots, which was evidence for the evaporation of the cathode material.

For $d_f \ll L$, the irradiated spot area is $S \sim L^2$. As can be seen from Fig. 1 (curve *2*), the plot of $Q^{-1/2}$ versus L is linear. According to relation (1), this is evidence for a two-photon mechanism of the laser-induced generation of free electrons.

The maximum photoionization efficiency was observed for a magnesium cathode (see table), in which the absolute value of the emitted charge at $L = \pm 5$ mm corresponded to 2.3×10^5 electrons per charge.

Analogous (although not as pronounced) behavior of $Q(L)$ was observed in the ionization chamber filled with pure carbon dioxide. The electron charge emitted under laser irradiation in vacuum was stable in time. In contrast, the charge emitted under irradiation in the carbon dioxide at a pressure of 1 and 4 bar decreased within 1 h by 10 and 40%, respectively (Fig. 2). Upon termination of the irradiation, the initial Q value was restored within several hours. This behavior is probably indicative of certain physicochemical processes occurring on the cathode surface heated by laser irradiation.

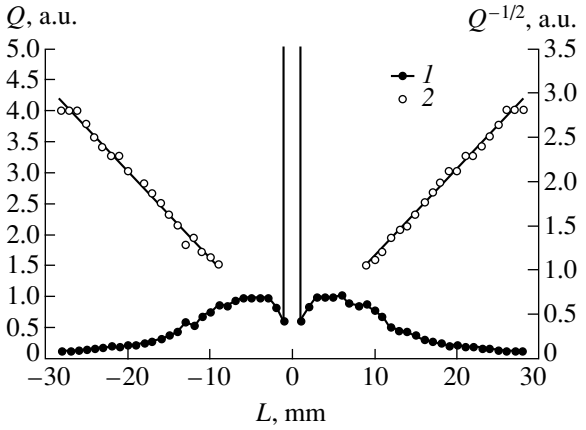

Fig. 1. Plots of (*1*) the electron charge Q emitted into vacuum and (*2*) $Q^{-1/2}$ versus focus–cathode distance L in the ionization chamber.

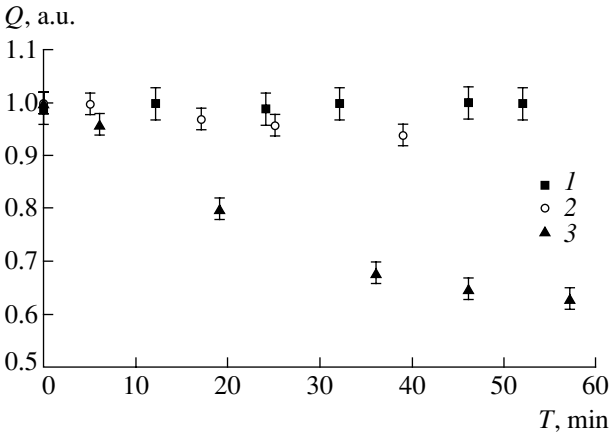

Fig. 2. Plots of the electron charge Q emitted from a magnesium cathode into (*1*) vacuum and (*2*, *3*) carbon dioxide at a pressure of 1 and 4 bar, respectively, versus time of exposure to an N_2 laser operating at a power repetition rate of 10 Hz. The electric field strength between electrodes was $E = 400$ (*1*, *2*) and 1600 V/cm (*3*).

The obtained results can be used in the experimental physics of elementary particles for the development of gas and liquid detectors, mean electron lifetime meters, and laser calibration systems, as well as in the physics of plasma and gas discharge.

Electron charge Q emitted into vacuum from various materials under the action of N_2 laser radiation

Photocathode	Ca	Mg	Be	Ti	Pb	Al	Mo	Sn	Cu	Ni	W	Si	Au	CsI	Diamond	1Kh18N10T stainless steel
Work function, eV	2.80	3.64	3.92	3.95	4.0	4.25	4.3	4.38	4.4	4.5	4.54	4.8	5.1	6.4	–	–
Q, rel. units	0.55	1	0.3	0.35	0.6	0.64	0.18	0.32	0.12	0.1	0.03	0.05	0.3	0.2	0.4	0.6

Acknowledgments. The authors are grateful to I.M. Obodovskiĭ and A.V. Ridiger for their permanent attention and valuable advice and to D.V. Semenov for his help in experimental work.

This study was performed within the framework of the project "Detection of Mutagen and Carcinogen Hazard by Physicochemical Techniques" of the International Science and Technology Center (project no. 832) and supported in part by the Ministry of Education of the Russian Federation (programs "State Support for Regional Science and Technology Policy in High School" and "Federal-Regional Policy in Science and Technology") and by the State Scientific Center "Interphysica Lab."

REFERENCES

1. E. M. Gushchin and S. V. Somov, Prib. Tekh. Éksp., No. 4, 41 (2000).
2. A. V. Brandin, E. M. Gushchin, I. M. Obodovskiĭ, *et al.*, in *Collection of Scientific Works of Moscow Institute of Engineering Physics (MIFI)* (MIFI, Moscow, 2003), Vol. 5, pp. 104–105 [in Russian].
3. E. M. Gushchin, S. V. Somov, and M. K. Timofeev, Nucl. Instrum. Methods Phys. Res. A **433**, 518 (1999).

Translated by P. Pozdeev

Technical Physics Letters, Vol. 31, No. 9, 2005, pp. 741–745. Translated from Pis'ma v Zhurnal Tekhnicheskoĭ Fiziki, Vol. 31, No. 17, 2005, pp. 48–57.

Laser Plasma Emission Spectrum Corrected for the Quantitative Analysis of Alloys

S. M. Pershin[a,*] and F. Colao[b]

[a] *Wave Research Center, Prokhorov Institute of General Physics, Russian Academy of Sciences, Moscow, 117924 Russia*

[b] *ENEA, Dipartimento Innovazione, Centro Ricerche Frascati, 00044 Frascati (Roma), Italy*

* *e-mail: pershin@orc.ru*

Received March 30, 2005

Abstract—A new approach to the quantitative elemental analysis of alloys by means of the laser induced breakdown spectroscopy (LIBS) is proposed and justified. The proposed correction taking into account the Prokhorov–Bunkin melt transparency wave ensures a good agreement between the relative intensities of LIBS analytical lines [(nm): Cu, 511; Zn, 472; Sn, 286; Pb, 406] and the alloy stoichiometry for five samples of bronze measured in various regimes of plasma excitation and signal detection. © *2005 Pleiades Publishing, Inc.*

This communication is aimed at the justification of a new approach to the correction of the laser plasma emission spectrum with allowance for the Prokhorov–Bunkin transparency wave propagating in the melt [1] for the direct quantitative analysis of alloys by laser induced breakdown spectroscopy (LIBS), and the verification of the proposed approach in application to the analysis of bronze. The choice of bronze is related to the prospects for determining the age of archeological objects by measuring the lead content [2] without special sampling procedures and without touching these objects.

Since the appearance of lasers capable of exciting plasma at the surface of a sample, the spectra of emission from laser-induced plasmas have been used for the qualitative and quantitative analysis of materials [3, 4].

A significant progress in the sensitivity of qualitative analysis was originally, to our knowledge, achieved in 1987 due to a more than tenfold increase in the contrast of spectral lines of laser plasma emission [5], which was provided by using the regime of two-pulse plasma excitation (this regime was independently realized and patented in the same year in Japan [6]). The idea of that approach has proved to be very fruitful and it is still under development [7], which allowed the impurity detection threshold to reach a record level of several ppm [8].

Despite this progress, direct quantitative analysis of solid samples using LIBS without reference standards [9] still encounters considerable difficulties because of the discrepancy between the stoichiometry of a sample and the relative intensities of the lines of elements in the plasma emission spectrum of this sample. Nevertheless, it was established that the spectrum of laser induced plasma contains the analytical lines of elements whose relative intensities are proportional to variations in the relative concentrations of elements irrespective of differences in the schemes of measurements and in the radiation loading of samples [2, 4, 8–10]. This fact is indicative of the good reproducibility of the physical processes involved in the sequential stages of formation of the plasma emission spectrum: heating–melting–evaporation–optical breakdown [3, 4]. It was also established that, during optical breakdown in polyatomic molecular gases in the field of laser radiation pulses, the relative intensities of spectral lines are proportional to the stoichiometric coefficients of gas components and increase linearly with their concentrations [11].

Based on these data, we may conclude that the intensity of analytical lines of elements in the spectrum of laser-induced optical breakdown in vapor over the melt must correspond to their relative concentrations (stoichiometry) in the vapor phase. From this we infer that the observed discrepancy between the stoichiometry of a metal alloy and the ratios of line intensities in the plasma emission spectrum [2, 7–10] most probably appears before the stage of optical breakdown. Therefore, this discrepancy arises in the stages of heating, melting, and evaporation of a multicomponent alloy. There are several factors favoring the selective evaporation of elements.

We may expect a pronounced selectivity in the course of evaporation of an alloy containing impurities in the form of grains segregating at the metal surface, provided that the thermal characteristics of components are significantly different. Then, the lower the melting temperatures, latent heats of fusion, and evaporation

1063-7850/05/3109-0741$26.00

heats, the higher the vapor pressure of such elements. In pure metals, this assumption is confirmed by an increase in the mass of a melt produced upon laser ablation of metals with lower melting temperatures [12].

As is known, differences in the saturation vapor pressure may also account for the selective evaporation of elements [1, 2]. However, this effect may be rather insignificant since, as was demonstrated in [13], the vapor pressure upon laser ablation can be several times smaller than the value calculated using the Clausius–Clapeyron equation [1, 2]. For example, the measured vapor pressure (600 bar) over nickel ablated by pulses of an excimer KrF laser (λ = 248 nm) was only about one third of the calculated value even in the vicinity of the critical temperature (7810 K) [13].

Another mechanism contributing to the selective evaporation of alloy components in the course of multiply repeated irradiation with laser pulses is the segregation, which is manifested by the formation of separate grains of the alloy component upon cooling of the melt [14]. In the case under consideration, such grains will be independently evaporated in the course of crater heating by every arriving laser pulse.

The selective evaporation of elements from the melt can also be significantly influenced by the period of time for which the melt is maintained at a temperature T_{md} of the phase transition from the overheated liquid metal to dielectric, which is always higher than the boiling temperature T_b. This state was predicted by Landau [15] and then confirmed by Kikoin [16] in experiments on mercury. It is important to note that such a transition was also observed in laser-induced breakdown at the metal surface [1]. Moreover, it was established that the metal–dielectric transition during laser heating is accompanied, in contrast to the case of thermal heating [16], by a new phenomenon called transparency wave propagation in the melt without absorption of laser radiation. In this regime (despite the metal overheating up to T_{md}), the boiling process is not developed and a fraction of the laser pulse energy transmitted through the melt is spent for heating the underlying solid metal and for maintaining the selective evaporation until the optical breakdown onset [1]. This mechanism explains the anomalous decrease in the coefficient of reflection of the metal surface down to a certain constant level during the laser pulse, which was experimentally observed in [17, 18].

It should be noted that the absence of boiling in the crater in the presence of the Prokhorov–Bunkin transparency wave [1] is a key factor determining the selectivity of the laser-induced surface evaporation process. Selective component evaporation always takes place, in accordance with Konovalov's fourth law [19], in solutions whose compositions do not correspond to the azeotropic point. The ejection of all melt from the crater during laser ablation [20] ensures that the stoichiometry of this melt evaporated in the field of the next laser pulse will be the same as that of the solid phase. Then, the thermal balance equation [1] for a pure metal can be written as

$$V = Q[\rho c(T_m - T_0) + \lambda_m + \lambda_v]^{-1}, \quad (1)$$

where V is the evaporated volume; Q is the absorbed fraction of the laser pulse energy; ρ and c are the density and heat capacity of the material, respectively; T_m and λ_m are the melting temperature and the heat of melting of the material, respectively; λ_v is the heat of evaporation of the material; and T_0 is the initial temperature. The latter quantity gives a rather insignificant correction and, hence, can be ignored because the first term in Eq. (1) is much smaller than the last one. For example, the values of these terms for Pb when T_0 is room temperature are 444 and 9737 J/cm^3, respectively. For an alloy with the component concentrations C_i, Eq. (1) has to be only slightly modified:

$$V_i \approx C_i Q(\rho c T_m + \lambda_m + \lambda_v)_i^{-1}(T/T_{mi}). \quad (2)$$

Here, a phenomenological dimensionless factor T/T_{mi} is introduced in order to take into account the duration of the interval of active evaporation of each component, from the moment of reaching the melting temperature of this component (T_{mi}) to the moment of attaining a temperature T corresponding to termination of the selective evaporation process (e.g., the optical breakdown).

Let us ignore the saturation effect [13] and assume that the analytical line intensity I_i of the ith alloy component in the plasma is proportional to the corresponding amount of vapor or the volume V_i of the evaporated material. Then, the intensities I_i can be determined, the alloy stoichiometry reconstructed, and the initial component concentration calculated by solving the following system of equations:

$$C_i \approx \mathrm{const} I_i(\rho c T_m + \lambda_m + \lambda_v)_i T_{mi}, \quad (3)$$

$$\sum C_i = 1. \quad (4)$$

In many cases, the alloy composition contains a predominating component with a high concentration (80–90%). For example, the HPb bronze has the following nominal composition (wt %): Cu, 82.47; Sn, 5.29; Zn, 5.86; Pb, 5.55 [2]. In this case, it is convenient to use the intensity correction coefficients K_i relative to copper:

$$C_{ir} = C_{\mathrm{Cu}}(I_i/I_{\mathrm{Cu}})K_i. \quad (5)$$

Equations (3) and (5) show that the K_i value can be calculated using the tabulated values of thermal parame-

ters of the known components of the alloy:

$$K_i = [(\rho c T_m + \lambda_m + \lambda_v)T_m]_i / [(\rho c T_m + \lambda_m + \lambda_v)T_m]_{\mathrm{Cu}}. \quad (6)$$

The content of a predominating component in the given alloy must be known a priori of being evaluated in preliminarily analyses. In particular, the intensity correction coefficients K_i by formula (6) for a typical four-component bronze (Cu–Sn–Zn–Pb) gives the ratios 1 : 0.114 : 0.156 : 0.097, respectively. These ratios reflect differences in the work functions and the times of possible active evaporation of the alloy components.

The experiments were performed with a pulsed (8 ns) Nd:YAG laser operating at 1064 nm. The laser radiation was focused on the horizontal sample surface by a lens with a focal distance of $F = 155$ mm. The laser pulse energy was 200 mJ, which corresponded to a beam intensity of ~35 GW/cm^2 and an energy density of ~300 J/cm^2 at the sample surface. The laser could also operate in a double-pulse mode, whereby two pulses with the same parameters as above were generated with an interval of 45 μs. The laser flash repetition rate was 10 Hz.

The laser-induced plasma flare emission was collected by a quartz lens ($F = 85$ mm) at an angle of 90° relative to the flare axis and projected onto the entrance slit of the spectrograph with a 1 : 1 magnification. The flare axis was parallel to the spectrograph slit. The slit width (30 μm) provided for a spectral resolution of 0.5 cm^{-1} (0.014 nm) per element of a CCD matrix with a gated image intensifier.

We have analyzed five samples of copper-based alloys representing four-component (Cu–Pb–Sn–Zn) bronzes previously studied in [2]. The concentrations of minor additives (Pb, Sn, Zn) were varied within 0–11 wt %, while the major component (Cu) content continued to predominate and varied within 77–90 wt %. The samples were mounted on a rotating base at a distance of 153–154 mm from the pump focusing lens in order to reduce the influence of the sample inhomogeneity and crater depth on the emission spectra averaged over 30 laser pulses. The analyses were performed for the same analytical lines as those used in [2] (nm): Cu, 511; Zn, 472; Sn, 286; Pb, 406. The relative intensities of these lines have proved to be proportional to the relative concentrations of the corresponding elements [2]. The emission spectra were measured within a gate length of 2 μs, the beginning of which was delayed by 1.5 μs relative to the first or the second laser pulse.

Figure 1 shows a fragment of the laser plasma emission spectrum in the region of the Sn (286.33 nm) line measured upon plasma excitation on the surface of HPb bronze [2] by the (*a*) first and (*b*) second laser pulses in the double-pulse mode. The line intensity was determined as the amplitude of an approximating Gauss envelope (thin solid line in Fig. 1, curve *b*), which allowed us to eliminate the influence of background emission and to make a correction for the self-absorption [2]. It should be noted that the line intensity measured after the second laser pulse is several times that observed after the first pulse [5, 21].

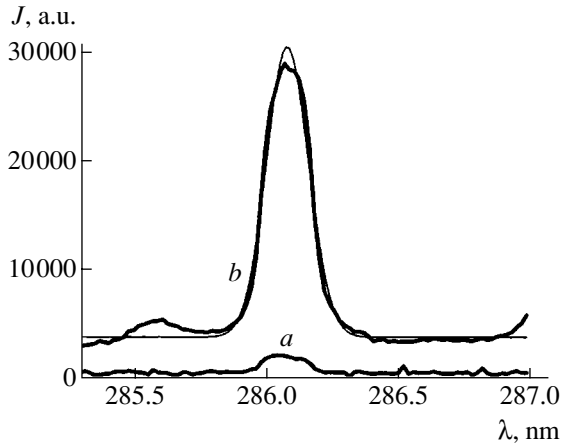

Fig. 1. The Sn (286.33 nm) line contour measured upon plasma excitation on the surface of HPb bronze [2] by the (*a*) first and (*b*) second laser pulses in the double-pulse mode. Thin solid curve is the approximating Gauss envelope used for determining the line intensity.

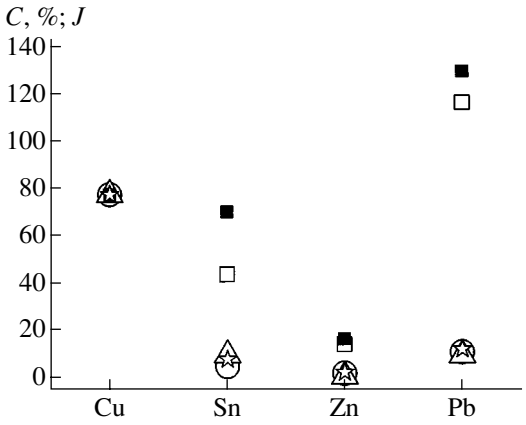

Fig. 2. A histogram of the relative intensities of plasma emission lines [(nm): Cu, 511; Zn, 472; Sn, 286; Pb, 406] normalized to the Cu (511 nm) line intensity for a sample of B30 bronze [(wt %): Cu, 77.55; Sn, 9.80; Zn, 0.99; Pb, 10] measured upon excitation by the first (open squares) and second (black squares) pulse: circles and stars show the data after correction, respectively; triangles show the concentrations of elements in the alloy.

Then, the intensities of the lines of all components measured for all samples under the same conditions of laser irradiation were normalized to the intensity of the Cu (511 nm) line. Figure 2 shows data on the relative intensities of emission lines for a sample of B30 bronze (wt %): Cu, 77.55; Sn, 9.80; Zn, 0.99; Pb, 10 [2]. The open and black squares refer to the values measured after the first and second laser pulse, respectively. As

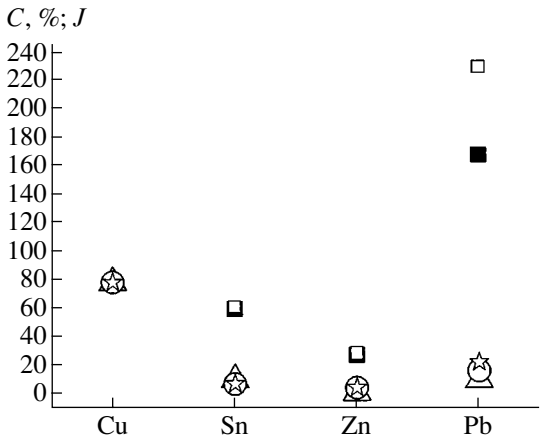

Fig. 3. A histogram of the relative intensities of plasma emission lines [(nm): Cu, 511; Zn, 472; Sn, 286; Pb, 406] normalized to the Cu (511 nm) line intensity for a sample of B30 bronze [(wt %): Cu, 77.55; Sn, 9.80; Zn, 0.99; Pb, 10] measured upon excitation by single pulses with an energy of 56 mJ (open squares) and 324 mJ (black squares): circles and stars show the data after correction, respectively; triangles show the concentrations of elements in the alloy.

can be seen, despite an almost tenfold increase in the line intensity (Fig. 1) upon the double-pulse action, the relative intensities vary to a much lower extent. Note that the normalized line intensities and their ratios [e.g., after the second pulse (%): Cu, 77.55; Sn, 70.2; Zn, 16.8; Pb, 130.4] significantly differ from those corresponding to the stoichiometry of the B30 bronze (wt %): Cu, 77.55; Sn, 9.80; Zn, 0.99; Pb, 10 (denoted by triangles in Fig. 2). The correction of the line intensities in terms of Eq. (6) (see Fig. 2, circles and stars for the first and second laser pulses, respectively) significantly improves the correspondence between the relative line intensities and the concentrations (stoichiometry) of the elements (Fig. 2, triangles).

The same procedure was used in order to correct the spectra measured using a quasi-coaxial scheme of registration and a single-pulse excitation of the plasma at a pulse energy of 56 and 324 mJ with a pump focusing lens (F = 200 mm) [2]. The results of this correction are presented in Fig. 3, where the notation is the same as in Fig. 2 (squares refer to the values before correction; and circles and stars, after correction). As can be seen, the stoichiometry of this bronze almost perfectly agrees with the relative intensities of lines after the proposed correction. The same trends were observed for the correction of all other spectra of bronze samples measured in various regimes of plasma excitation and signal detection.

Thus, we have demonstrated that deviation of the plasma composition from stoichiometry is caused by the selective evaporation of elements during the time preceding optical breakdown. We have calculated the intensity correction coefficients for the plasma emission lines with allowance for the Prokhorov–Bunkin transparency wave propagating in the melt, which make possible the direct determination of element concentrations by LIBS without using reference samples.

The proposed correction procedure significantly improves the agreement between the relative intensities of emission lines and the true stoichiometry of the sample composition. For a typical sample of B30 bronze [nominal composition (wt %): Cu, 77.55; Sn, 9.80; Zn, 0.99; Pb, 10], the correction gives the line intensity ratios 77.55 : 5 : 2.3 : 11.34 and 77.55 : 8 : 2.6 : 12.6 wt % for a single- and double-pulse plasma excitation regime, respectively. Analogous improvement was achieved upon the correction of experimental data obtained previously [2] for the same samples of bronze measured using a different signal detection configuration and a different regimes of plasma excitation (Nd:YAG laser radiation with a pulse energy of 56 and 324 mJ).

The remaining deviations of the measured concentrations of elements from the true values can also be related to the non-optimal choice of the duration and delay of the gate pulses used for the spectrum measurement and to the selection of analytical lines (for the convenience of comparison, we used the same lines as those employed in [2]). The influence of these factors and the role of spectroscopic parameters (level population, oscillator strength, emission kinetics, etc. [2, 9]) will be considered in the following publication.

It would also be of interest to use the proposed approach for the correction of the emission spectra of plasmas excited by pico- and femtosecond pulses, as well as to apply this method to the analysis of different alloys.

Acknowledgments. The authors are grateful to S. Lokshtanov and V. Spizzicchino for their help in processing laser plasma emission spectra.

This study was supported in part by the Russian Foundation for Basic Research (project no. 02-03-16046) and by the ENEA Center (Frascati, Roma, Italy).

REFERENCES

1. A. M. Prokhorov, V. A. Batanov, F. V. Bunkin, and V. B. Fedorov, IEEE J. Quantum Electron. **9**, 503 (1973).
2. L. Fornarini, F. Colao, R. Fantoni, *et al.*, Appl. Phys. A **80** (in press).
3. F. Brech and L. Cross, Appl. Spectrosc. **16**, 59 (1962).
4. L. J. Radziemski, Spectrochim. Acta B **57**, 1109 (2002).
5. G. P. Arumov, A. Yu. Bukharov, S. M. Pershin, *et al.*, Pis'ma Zh. Tekh. Fiz. **13** (7), 870 (1987) [Sov. Tech. Phys. Lett. **13**, 362 (1987)].
6. K. Takaharu, S. Hiroya, S. Koichi, and M. Katsusuke, JP Patent No. 62-85847 (1987).
7. J. Scaffidi, W. Pearman, J. C. Carter, *et al.*, Appl. Opt. **43**, 6492 (2004).

8. L. St-Onge, M. Sabsabi, and P. Cielo, J. Anal. At. Spectrom. **12**, 997 (1997).
9. M. Corsi, G. Cristoforetti, V. Palleschi, *et al.*, Eur. Phys. J. D **13**, 373 (2001).
10. V. Lazic, R. Fantoni, F. Colao, *et al.*, J. Anal. At. Spectrom. **19**, 429 (2004).
11. L. Dudragne, Ph. Adam, and J. Amouroux, Appl. Spectrosc. **52**, 1321 (1998).
12. C. Geertsen, A. Briand, F. Chartier, *et al.*, J. Anal. At. Spectrom. **9**, 17 (1994).
13. X. Xu and K. Song, Appl. Phys. A **69** (Suppl.), S869 (1999).
14. L. A. Golovan, B. A. Markov, P. K. Kashkarov, and V. Yu. Timoshenko, Solid State Commun. **108**, 707 (1998).
15. Ya. B. Zel'dovich and L. D. Landau, Zh. Éksp. Teor. Fiz. **38**, 32 (1944).
16. I. K. Kikoin and A. P. Senchenkov, Fiz. Met. Metalloved. **24**, 843 (1967).
17. A. M. Bonch-Bruevich, Y. A. Imas, G. S. Romanov, *et al.*, Sov. Phys. Tech. Phys. **13**, 640 (1968).
18. T. E. Zavecz, M. A. Saifi, and M. Noits, Appl. Phys. Lett. **26**, 165 (1975).
19. B. V. Nekrasov, *Bases of General Chemistry* (Khimiya, Moscow, 1973), Vol. 1 [in Russian].
20. J. M. Fishburn, M. J. Withford, D. W. Coutts, and J. A. Piper, Appl. Opt. **43**, 6473 (2004).
21. F. Colao, V. Lazic, R. Fantoni, and S. Pershin, Spectrochim. Acta B **57**, 1167 (2002).

Translated by P. Pozdeev

Technical Physics Letters, Vol. 31, No. 9, 2005, pp. 746–748. Translated from Pis'ma v Zhurnal Tekhnicheskoĭ Fiziki, Vol. 31, No. 17, 2005, pp. 58–62.

The Energy Levels in Quantum Wells Formed at the Contacts between Cubic and Hexagonal Polytypes of Silicon Carbide

S. Yu. Davydov* and O. V. Posrednik

Ioffe Physicotechnical Institute, Russian Academy of Sciences, St. Petersburg, 194021 Russia

** e-mail: Sergei.Davydov@mail.ioffe.ru*

Received April 20, 2005

Abstract—The energies of the ground (ε_0) and the first excited state (ε_1) in a quantum well (QW) are evaluated within the framework of the triangular QW model. It is shown that the ε_0 level in QWs at the contacts between cubic (3C) and hexagonal (*N*H, *N* = 2, 4, 6, 8) polytypes of silicon carbide (SiC) can be effectively controlled only by means of doping a wide-bandgap *n*-*N*H-SiC polytype with shallow donors. © *2005 Pleiades Publishing, Inc.*

The continuously increasing interest in the heterostructures formed using various polytypes of silicon carbide (SiC) [1] is related to the prospects for obtaining practically defectless contacts. At present, the most thorough investigations have been performed for 3C/6H [2, 3] and 3C/4H [4] heterojunctions. On the side of the narrow-bandgap component (3C-SiC) of such junctions, the contact features a two-dimensional (2D) quantum well (QW) containing at least one localized electron state. Such QWs are characterized by the energy positions of local levels (more precisely, 2D subbands) ε_0, ε_1, and so on, measured from the well bottom. As a rule, the ground state level ε_0 occurs below the Fermi level, while the first excited level ε_1 is situated above the Fermi level.

The aim of this study was to evaluate the ε_0 and ε_1 energies for the heterojunctions between cubic (3C) and hexagonal (*N*H, *N* = 2, 4, 6, 8) SiC polytypes.

Let us consider the problem of determining the ε_0 value within the framework of the approach developed in [5]. The Poisson equation for a 3C-SiC region can be written as

$$\frac{dF}{dx} = \frac{e}{\varepsilon_{st}} n(x), \tag{1}$$

where x is the coordinate in the direction (quantization axis) perpendicular to the contact plane and $\varepsilon_{st} = \varepsilon_{st}(3C)$. The electron density $n(x)$ in the QW can be expressed as

$$n(x) = n_s \delta(x), \tag{2}$$

where n_s is the 2D electron gas density in the QW, $\delta(x)$ is the Dirac delta, and $x = 0$ is the coordinate of the contact plane. Integrating Eq.(1) and taking into account formula (2), we obtain

$$F = \frac{e n_s}{\varepsilon_{st}}. \tag{3}$$

At very low temperatures, when only ε_0 occurs below the Fermi level, we have [5]

$$n_s = \bar{D}(\Delta - \varepsilon_0), \tag{4}$$

where $\bar{D} = k(m^*/\pi\hbar^2)$ is the density of states corresponding to a single quantum confinement level, k is the number of equivalent valleys, and Δ is the Fermi energy relative to the QW bottom (in the case of very low temperatures, $\Delta - \varepsilon_0 \gg k_B T$).

In an infinitely deep triangular QW, the ground state energy ε_0 is given by the formula [6, 7]

$$\varepsilon_0 \approx 1.856\left(\frac{e^2 F^2 \hbar^2}{m^*}\right)^{1/3}, \tag{5}$$

where F is the electric field strength on the 3C-SiC side of the *N*H/3C contact, m^* is the effective electron mass in 3C-SiC, e is the electron charge, and $\hbar$ is the Planck constant. Substituting relations (3) and (4) into formula (5), we eventually obtain

$$\varepsilon_0^3 = A_k(\Delta - \varepsilon_0)^2,$$
$$A_k = (1.856)^3 k^2 (e^2/\pi\varepsilon_{st})^2 (km^*/\hbar^2). \tag{6}$$

1063-7850/05/3109-0746$26.00

Introducing the dimensionless quantities $\zeta = \varepsilon_0/\Delta$ and $\alpha = A_k/\Delta$, we can rewrite Eq. (6) as

$$\zeta^3 = \alpha(1-\zeta)^2. \quad (7)$$

Note that, by definition, $0 \le \zeta < 1$, and $\zeta \longrightarrow 0$ as $\alpha \longrightarrow 0$ and $\zeta \longrightarrow 1$ as $\alpha \longrightarrow \infty$. The plots of ζ and the ratio ζ/α versus α are presented in the figure. As can be seen, ζ exhibits rapid growth only for $0 < \alpha < 2$ and varies relatively slowly for $\alpha > 2$. The plot of ζ/α versus α exhibits a hyperbolic character.

Let us estimate the coefficient A_k. For the 3C/6H-SiC heterojunction, the number of equivalent valleys is $k = 3$, while for AlGaN/GaN and AlGaAs/GaAs structures this parameter is $k = 1$ [5, 8]. For comparison, below we will consider both values of k, but the ε_{st} and m^* values will be set equal to those for C3-SiC. For $\varepsilon_{st}(3C) = 9.72$ [9], we obtain $A_k = 1.422k^2(m^*/m_0)$, where m_0 is the free electron mass. According to [10], the effective mass for the density of states in one valley is such that $m^*/m_0 = 0.35$. Then, $A_1 \approx 0.50$ eV and $A_3 \approx 4.48$ eV.

It should be noted that, in the context of the 3C/*N*H-SiC system under consideration, the A_k value is constant. Therefore, an increase in α corresponds to a decrease in Δ (whereby the Fermi level approaches the QW bottom). However, Δ must not be lower than ε_0; otherwise the ε_0 level will be unoccupied (it should be recalled that we are considering the case of very low temperatures). Therefore, $\alpha_{k\max} = A_k/\varepsilon_0$. Since $\varepsilon_0 \approx 0.06$ eV [3], we obtain $\alpha_{1\max} \approx 8.33$ and $\alpha_{3\max} \approx 74.65$. Using the definitions of ζ and α, we obtain the relation

$$\varepsilon_0 = (\zeta/\alpha_k)A_k. \quad (8)$$

For $\varepsilon_0 \approx 0.06$ eV, this formula yields $\zeta/\alpha_1 \approx 0.12$ and $\zeta/\alpha_3 \approx 0.013$. These ratios yield $\alpha_1 \approx 6$ and $\alpha_3 \approx 70$ and, accordingly, we obtain the quite reasonable estimates $\Delta_1 \approx 0.083$ eV and $\Delta_3 \approx 0.064$ eV. Note that, when α increases by more that an order of magnitude, the value of Δ only decreases by 23%.

When the Fermi level approaches the edge of the conduction band for the *N*H-SiC polytype, the Δ value grows, α drops, and the ratio $\zeta/\alpha = \varepsilon_0/A$ increases. Therefore, we may conclude that the doping of n^+-*N*H-SiC with shallow donors leads to a increase in the local ground state energy in the QW. Using the estimate of $F \approx 2 \times 10^7$ V/m [3] and a quasi-classical expression for the energy levels ε_n ($n = 1, 2, \ldots$) in a triangular quantum well [7, 11],

$$\varepsilon_n = (\hbar^2/2m^*)\left[\frac{3\pi eF}{2}\left(n+\frac{3}{4}\right)\right]^{2/3}, \quad (9)$$

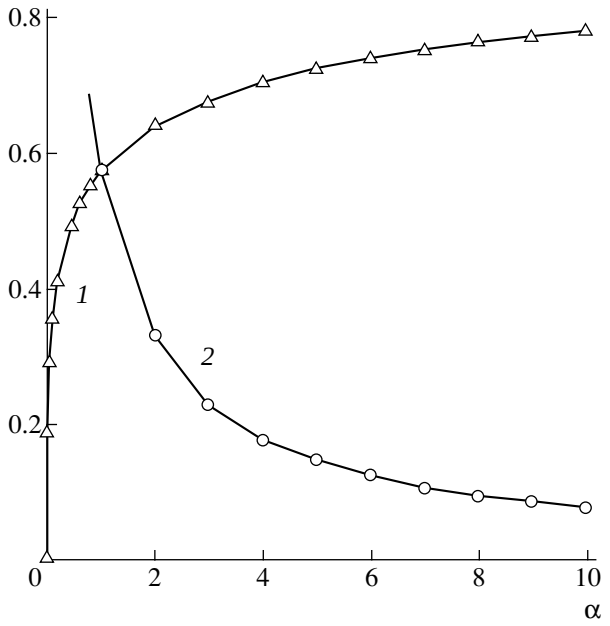

Plots of (*1*) $\zeta = \varepsilon_0/\Delta$ and (*2*) the ratio $\zeta/\alpha = \varepsilon_0/A$ versus $\alpha = A/\Delta$.

we obtain $\varepsilon_1 \approx 0.144$ eV. This level is apparently situated above the Fermi level and, in the case of extremely low temperatures, is virtually completely empty.

Applying the expressions for $n_s(T)$ [5] to the case of high temperatures ($\Delta - \varepsilon_0 \gg k_B T$ and $\varepsilon_1 - \Delta \gg k_B T$), we obtain

$$n_s = \bar{D}[(\Delta - \varepsilon_0) - (\varepsilon_1 - \Delta)], \quad (10)$$

from which it follows that the QW population decreases. However, since the field strength F decreases as well, both ε_0 and ε_1 shift down along the energy scale and the QW population increases. Thus, there is a certain temperature stabilization of the positions of ε_0 and ε_1 levels. It is also interesting to note that relation (10) is also valid at very low temperatures, when ε_1 occurs below the Fermi level [5].

Acknowledgments. This study was supported in part by the Russian Foundation for Basic Research (project no. 03-02-16054b), the INTAS Foundation (grant no. 01-0603), and the NATO Science for Peace Program (grant no. 978011).

REFERENCES

1. A. Fissel, Phys. Rep. **379**, 149 (2003).
2. A. A. Lebedev, A. M. Strel'chuk, D. V. Davydov, *et al.*, Pis'ma Zh. Tekh. Fiz. **28** (18), 89 (2002) [Tech. Phys. Lett. **28**, 792 (2002)].
3. A. A. Lebedev, A. M. Strel'chuk, N. S. Savkina, *et al.*, Pis'ma Zh. Tekh. Fiz. **28** (23), 78 (2002) [Tech. Phys. Lett. **28**, 1011 (2002)].

4. A. Fissel, U. Kaizer, B. Schröter, *et al.*, Appl. Surf. Sci. **184**, 37 (2001).
5. H. Morcoc, in *Molecular Beam Epitaxy and Heterostructures*, Ed. by L. L. Chang and K. Ploog (Martimus Nishoff, Amsterdam, 1985).
6. V. M. Galitskiĭ, B. M. Karnakov, and V. I. Kogan, *Problems in Quantum Mechanics* (Nauka, Moscow, 1992) [in Russian].
7. V. Ya. Demikhovskiĭ and G. A. Vugal'ter, *Physics of Quantum Low-Dimensional Systems* (Logos, Moscow, 2000) [in Russian].
8. V. M. Polyakov and F. Schwierz, in *Proceedings of the International Scientific Colloquy of the Technical University of Ilmenau, Germany, 2003*, p. 1.
9. V. I. Gavrilenko, A. M. Grekhov, D. V. Korbutyak, and V. G. Litovchenko, *Optical Properties of Semiconductors: A Handbook* (Naukova Dumka, Kiev, 1987) [in Russian].
10. N. T. Son, W. M. Chen, O. Kordina, *et al.*, Appl. Phys. Lett. **66**, 1074 (1995).
11. T. Ando, A. B. Fowler, and F. Stern, in *Electronic Properties of Two-Dimensional Systems* (Am. Phys. Soc., New York, 1982).

Translated by P. Pozdeev

Technical Physics Letters, Vol. 31, No. 9, 2005, pp. 749–751. Translated from Pis'ma v Zhurnal Tekhnicheskoĭ Fiziki, Vol. 31, No. 17, 2005, pp. 63–68.

Effect of Gas Adsorption on the Photoconductivity of CdSe/Dielectric Thin Film Structures

O. E. Kovalenko and V. G. Guzovskiĭ

Institute of Applied Optics, National Academy of Sciences of Belarus, Mogilev, Belarus

e-mail: iponanb@mogilev.by

Revised manuscript received April 25, 2005

Abstract—The sensitivity of CdSe/PETP thin-film structures with respect to the adsorption of ammonia, aqueous ammonia, and water vapor from the gas phase at room temperature has been studied. The photoconductivity of the best samples exhibited reversible variations within two orders of magnitude in response to the presence of ammonia vapor. The concentration of ammonia in the gas phase can be measured in the interval from 0.25 to 25 vol %. © *2005 Pleiades Publishing, Inc.*

The adsorption of various gases on the surface of thin-film semiconductor structures has received much attention because the electrical properties of such structures depend on the state of the ambient medium [1], which makes them promising sensor materials [2, 3]. Most thin-film sensors intended for the detection of gases and gas-phase admixtures employ the phenomenon whereby he electric resistance of a semiconductor changes in response to the chemical or physical adsorption of detected species on the material surface [4]. In order to provide the maximum sensitivity and selectivity of analysis, the working temperatures of such devices are usually selected in the range from 100 to 500°C, which imposes high requirements with respect to the thermal stability of the parameters of the base thin-film structure.

This letter presents the results of investigations of the adsorption of various gas-phase admixtures on the photoconductivity of thin-film structures based on CdSe and poly(ethylene terephthalate) (PETP).

The CdSe/PETP thin-film structures were prepared by alternating electron beam deposition in vacuum from two independent sources of components [5]. The sample film thickness in all cases was about 0.7 μm, while the semiconductor content was varied from 20 to 90 vol %. The semiconductor component had the form of nanograins with an average diameter of ~6 nm [5], as evaluated from the "blue" shift of the bandgap width of CdSe.

The photoconductivity spectra were measured on the automated setup based on an MDR-23 monochromator, an incandescent lamp, and a Unipan 232 lock-in amplifier. The number of incident photons was independent of the light wavelength. A system of coplanar indium electrodes separated by 1 mm was formed on the sample surface by means of vacuum deposition. The photoconductivity was also measured using light-emitting diodes operating at 530 and 630 nm. The incident light was intensity-modulated at a frequency of 20 Hz and focused in the interelectrode gap. The photomodulated transmission spectra of thin-film structures were measured at room temperature in a quasi-longitudinal geometry using a phase lock-in detection scheme [6].

The influence of gas-phase admixtures on the properties of samples was studied in chamber equipped with a gas-admission facility capable of reversibly changing the gas phase composition and pressure. In order to eliminate the influence of uncontrolled water vapor on the properties of samples, the chamber was equipped with an absorber filled with anhydrous calcium oxide. The measurements were performed after establishment of the equilibrium values. The temperature in the experimental chamber was always maintained on a constant level of 20°C.

When the properties of CdSe/TETP thin-film structures were studied in the sensor arrangement (see the inset to Fig. 1), the appearance of a gas-phase admixture in the chamber led to a change in properties of the film and in the response signal measured with the lock-in amplifier. The sensitivity of thin-film structures studied was characterized in terms of the variation of the photocurrent. We studied the properties of samples in response to the content of ammonia, aqueous ammonia, and water vapor in the gas phase. The source of NH_3 was a 10% aqueous ammonia solution. It was found that ammonia vapor not only influences the photocurrent but alters the dark current of the sample structure as well. The increase in the dark conductivity was probably related to the formation of a conducting adlayer on the sample surface. In order to eliminate the dark conductivity component, the photocurrent measurements were performed using a modulated light beam.

1063-7850/05/3109-0749$26.00 © 2005 Pleiades Publishing, Inc.

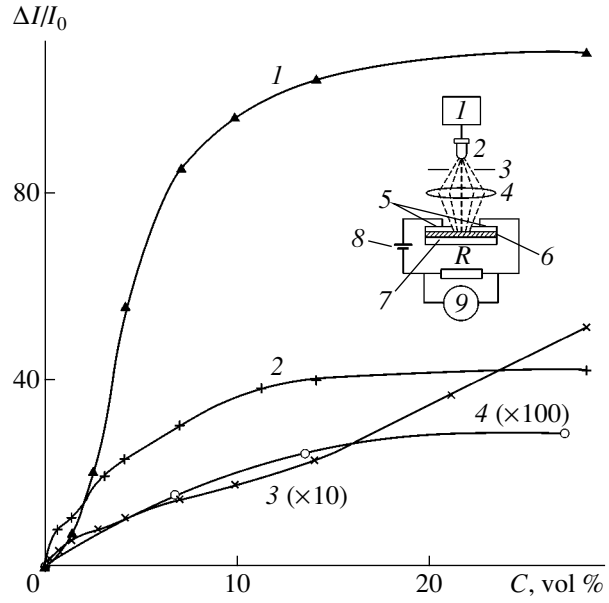

Fig. 1. Plots of the relative photocurrent change $\Delta I/I_0$ versus volume concentration C of (*1–3*) ammonia and (*4*) water vapor measured using CdSe/PETP thin-film structures with a semiconductor content of (*1*) 20, (*2*, *4*) 50, and 90 vol % (*3*). The inset shows a schematic diagram of the experimental arrangement: (*1*) ac voltage generator; (*2*) light-emitting diode; (*3*) diaphragm; (*4*) collecting lens; (*5*) indium electrodes; (*6*) sample film; (*7*) substrate; (*8*) bias source; (*9*) lock-in amplifier.

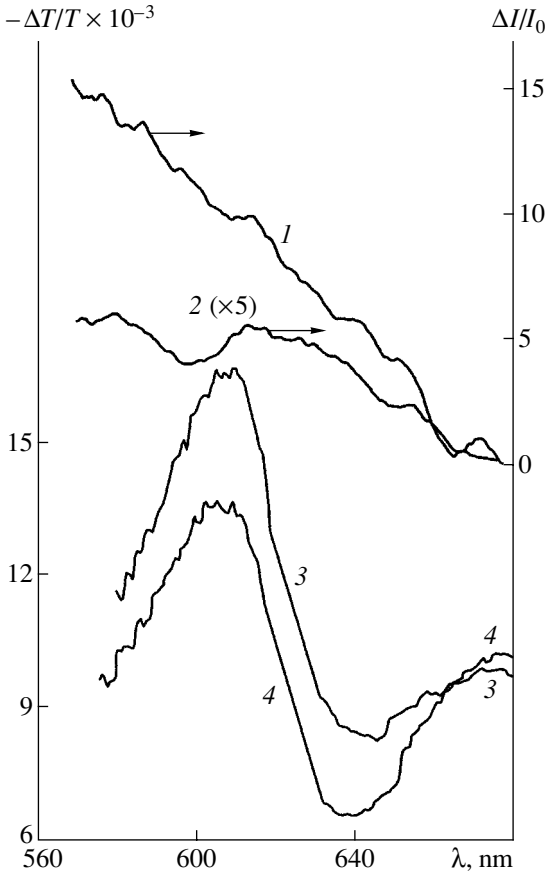

Fig. 2. Spectra of the (*1*, *2*) relative photocurrent change $\Delta I/I_0$ in ammonia and water vapor, respectively, and (*3*, *4*) photomodulated transmission $\Delta T/T$ at λ_p = 633 nm in ammonia vapor and dry air, respectively, for a CdSe/PETP thin-film structure with a semiconductor content of 90 vol %.

Figure 1 shows the results of measurements of the photocurrent of a CdSe/PETP thin-film structure as a function of the volume concentration of ammonia and water vapor. The response signal was $\Delta I/I_0$, where $\Delta I = I - I_0$, I is the modulated current amplitude measured in the presence of ammonia vapor, and I_0 is the modulated current amplitude in dry air. As can be seen from Fig. 1, the response signal exhibits considerable variations, which allows the given thin-film structure to be used as a gas sensor. The structure was most sensitive to the presence of ammonia vapor (Fig. 1, curves *1–3*). The photocurrent amplitude in the presence of ammonia vapor was one to two orders of magnitude higher than that observed in the presence of other admixtures (e.g., water, see Fig. 1, curve *4*). The concentration of ammonia vapor can be measured in the interval from 0.25 to 25 vol %.

The sensitivity of the structure studied with respect to gas-phase admixtures, as well as the range of their measurable concentrations, could be changed by varying the semiconductor/dielectric ratio in the course of synthesis of the thin-film structure. A decrease in the volume fraction of the semiconductor component led to an increase in the response signal intensity (Fig. 1, curves *1–3*), but this was accompanied by a decrease in the range of measurable concentrations. The saturation of the photocurrent for samples with lower content of the semiconductor component took place at lower volume concentrations of gas-phase admixtures.

As is known, a PETP layer as thin as 1–2 nm is virtually continuous [5] and may serve as a tunneling-transparent barrier with significantly different conductivities for electrons and holes. Such a barrier is capable of effectively separating charge carriers because the effective mass of electrons is about one order of magnitude lower than that of holes in CdSe nanograins [7]. Since the content of semiconductor nanograins in the samples was different, the thickness of dielectric spacers separating these particles also varied. The relative density of generated nonequilibrium carriers was higher in the samples with a lower content of the semiconductor component, which led to a greater relative change in the photocurrent in such samples.

The magnitude of the response signal in the structures studied was also dependent on the wavelength of the probing radiation. Figure 2 shows the spectra of the relative photocurrent $\Delta I/I_0$ (defined as in Fig. 1) of a thin-film structure exposed to ammonia (curve *1*) and

water vapor (curve *2*). It was found that anhydrous ammonia (obtained by passing vapor via the water absorber) virtually did not influence the photocurrent but changed (as well as the wet ammonium vapor did) the photoinduced absorption (measured as $\Delta T/T$, the relative change in the photomodulated optical transmission T) in the vicinity of the fundamental absorption edge (Fig. 2, curves *3* and *4*). In contrast, water vapor increased the photoconductivity (Fig. 2, curve *2*) but did not change the photomodulated transmission spectra near the fundamental absorption edge. It should be noted that the presence of water vapor in the gas phase influenced the photoinduced absorption in the region of $\lambda > 670$ nm, which could be related to the diffusion of water molecules into the nanostructure [8].

We believe that an increase in the photoinduced absorption in the region of photon energies $h\nu \le E_g$ in the presence of ammonia vapor is related to the adsorption of ammonia molecules on the surface states of CdSe nanograins, which leads to a decrease in the density of electron states responsible for the recombination of electrons. This hypothesis is confirmed by the increase in the electron lifetime (from 30 to 70 μs) under the action of ammonia vapor, whereas the hole lifetime remained unchanged (~20 μs). The molecules of water diffusing in the structure increased the probability of charge carrier transfer via the potential barriers formed by the dielectric component in the structure studied.

In conclusion, the obtained experimental results show that CdSe/PETP thin-film structures can be used in gas-phase admixture sensors capable of operating at room temperature.

Acknowledgments. This study was supported by the Basic Research Foundation of the Republic of Belarus.

REFERENCES

1. V. B. Zaĭtsev, A. V. Zoteev, *et al.*, Khim. Fiz. **18** (9), 35 (1999).
2. G. N. Gerasimov, E. I. Grigor'ev, A. E. Grigor'ev, *et al.*, Khim. Fiz. **17**, 168 (1998).
3. K. Bijan Miremadi, Konrad Colbow, and Yutaka Harima, Rev. Sci. Instrum. **68**, 3989 (1997).
4. G. Wiegleb, *Sensortechnik* (Franzis-Verlag, 1986).
5. A. S. Borbitskiĭ, A. I. Voitenkov, and V. P. Red'ko, Pis'ma Zh. Tekh. Fiz. **22** (13), 1 (1996) [Tech. Phys. Lett. **22**, 517 (1996)].
6. M. Cardona, *Modulation Spectroscopy* (Academic Press, New York, 1969; Mir, Moscow, 1972).
7. Todd D. Krauss and Louis E. Brus, Mater. Sci. Eng. B **69**–**70**, 289 (2000).
8. F. F. Vol'kenshtein, *Electronic Processes on Semiconductor Surface upon Chemisorption* (Nauka, Moscow, 1987) [in Russian].

Translated by P. Pozdeev

Technical Physics Letters, Vol. 31, No. 9, 2005, pp. 752–755. Translated from Pis'ma v Zhurnal Tekhnicheskoĭ Fiziki, Vol. 31, No. 17, 2005, pp. 69–76.

Application of the Darboux Transform to the Description of Linear Wave Propagation in Narrow Channels

A. I. Gudimenko* and K. G. Kuptsov

Pacific Institute of Oceanology, Far-Eastern Division, Russian Academy of Sciences, Vladivostok, Russia

** e-mail: algud@poi.dvo.ru*

Revised manuscript received May 3, 2005

Abstract—The standard *N*-order Darboux transformation (DT) for a one-dimensional Schrödinger operator is generalized for application to an arbitrary Sturm–Liouville operator, so that all coefficients of the later operator are subject to transformation. The generalized DT is applied to the description of linear barotropic wave propagation in narrow channels for constructing channel width and depth profiles admitting exact solutions. © *2005 Pleiades Publishing, Inc.*

In recent years, the method of Darboux transformation (DT) has received much attention as a simple and effective means of generating linear ordinary second-order differential equations admitting exact solutions in various applications [1–3]. However, it should be noted that the classical DT deals with a one-dimensional Schrödinger operator, which is only a partial case of the Sturm–Liouville operator (representing an arbitrary linear differential second-order operator). For this reason, the DT was previously applied predominantly either in quantum mechanics (for constructing potentials admitting exact solutions of the Schrödinger equation [1, 2]) or in the theory of solitons (for finding solutions of the Korteweg–de Vries equation known to be related to the Schrödinger operator [3]).

Direct applications of the DT method to fields of physics other than quantum mechanics are practically absent or—even if found as, for example, in acoustics—are again applied within the framework of the Schrödinger equation. This situation is explained, in particular, by the fact that practical problems usually encounter arbitrary Sturm–Liouville operators.

In this study, the classical DT is generalized to the case of an arbitrary Sturm–Liouville operator, which is conveniently written as

$$L := r^{-1}\frac{d}{dx}rp\frac{d}{dx} + q, \tag{1}$$

where r, p and q are functions of x. The generalization is obtained as a combination of the classical DT and the exactly solvable Kummer–Liouville transformations [4]. The generalized DT involves all coefficients of the Sturm–Liouville operator.

It should be noted that previously the classical DT was sometimes modified so as to apply to the more general Sturm–Liouville operators. However, the generalized transformations either involved only the coefficient q (see, e.g., [5]) or (even possessing a sufficiently general character) referred to rather specific cases (see, e.g., [4]) and were not suited for effective use in various physical applications.

The proposed generalization is applied to the description of linear barotropic wave propagation in narrow channels [6] for constructing channel width and depth profiles admitting exact solutions. Exact solutions of this problem are known only for a small number of channel width and depth profiles, in particular for linear and quadratic [6] and exponential profiles. However, using the DT, it is possible to generate a much wider spectrum of exactly solvable profiles, some of which may serve as good approximations to preset shapes.

Let us begin with the definition of the *N*-order DT for operator (1) with fixed r and p. Below, $L^{(N)}$ denotes the corresponding *N*-order DT of the operator L and $T^{(N)}$ denotes the operator of this transformation, that is, the operator satisfying the identity $L^{(N)}T^{(N)} = T^{(N)}L$. Then,

$$\begin{aligned} L^{(N)} &:= r^{-1}\frac{d}{dx}rp\frac{d}{dx} + q^{(N)}, \\ T^{(N)}u &= p^{1/2}\frac{\{u_{\lambda_1}, \ldots, u_{\lambda_N}, u\}}{\{u_{\lambda_1}, \ldots, u_{\lambda_N}\}}, \end{aligned} \tag{2}$$

where

$$q^{(N)} = q + 2\sqrt{p}\frac{d}{dx}\sqrt{p}\frac{d}{dx}\ln r^{N/2}p^{N^2/4}\{u_{\lambda_1}, \ldots, u_{\lambda_N}\}, \tag{3}$$

$u_{\lambda_1}, \ldots, u_{\lambda_N}$ are the eigenfunctions of L (these quantities will be referred to as the transformation functions)

corresponding to the eigenvalues $\lambda_1, \ldots, \lambda_N$, respectively, and braces denote the Wronskian of the enclosed functions.

Formulas (2) and (3) are obtained as follows. First, the Kummer–Liouville transformation [4] is used to reduce the initial operator to the Schrödinger operator. Then, the classical DT is applied to this Schrödinger operator. Finally, the result is subjected to the inverse (with respect to the initial) Kummer–Liouville transformation to yield the required operator. It should be recalled that the Kummer–Liouville transformation is a combination of the transformations of dependent and independent variables, the former being the multiplication by a function and the latter the substitution of coordinates [4]. It should also be noted that expressions (2) and (3) for $N = 1$ coincide with the relations obtained in [5].

Now let us generalize the obtained transformation by admitting variation of the coefficient r, while leaving the coefficient p fixed. To this end, we apply the Kummer–Liouville transformation T_a (T_a is the multiplication by a function a assumed to be positive) to $L^{(N)}$, which yields

$$L_1 := r_1^{-1}\frac{d}{dx}r_1 p\frac{d}{dx} + q_1. \tag{4}$$

Here, $r_1 = ra^{-2}$ (this can be readily checked) and the unknowns q_1 and a are related as

$$r^{-1}\frac{d}{dx}rp\frac{d}{dx}a^{-1} + (q^{(N)} - q_1)a^{-1} = 0. \tag{5}$$

It can be shown that Eq. (5) is exactly solvable for

$$q_1 := q^{(N)} - q^{(M)} + \lambda_0, \tag{6}$$

where M in the general case is different from N and λ_0 is a constant quantity. Indeed, Eq. (5) is an equation for eigenvalues of the M-order DT (2) of operator (1). Therefore, a^{-1} is the M-order DT of the eigenfunction u_{λ_0} of this operator, that is,

$$a^{-1} = T^{(M)}u_{\lambda_0}. \tag{7}$$

Using relation (7), the operator of the as-defined transformation is

$$T_1 := T_a T^{(N)} = T^{(N)}/T^{(M)}u_{\lambda_0}. \tag{8}$$

Finally, let us allow the coefficient p to vary as well. For this purpose, we substitute $x \longrightarrow y = \varphi^{-1}(x)$ in operator (4), where φ is defined so that

$$r = \varphi^*[r(T^{(K)}u_{\lambda_0})^2]\frac{d\varphi}{dy}, \tag{9}$$

where φ^* is the φ-induced action upon functions: $u(x) \longrightarrow \varphi^*u(y) := u(\varphi(y))$, and K is a natural number. Thus, we obtain the operator

$$L_2 := r_2^{-1}\frac{d}{dy}r_2 p_2\frac{d}{dy} + q_2, \tag{10}$$

where, according to relations (7) and (9),

$$\begin{aligned} r_2 &= r\varphi^*(T^{(M)}u_{\lambda_0}/T^{(K)}u_{\lambda_0})^2, \\ p_2 &= r^{-2}\varphi^*[r^2 p(T^{(K)}u_{\lambda_0})^4], \quad q_2 = \varphi^* q_1. \end{aligned} \tag{11}$$

The operator T_2 of this transformation is defined by formula (8). Passing to the new variable, we obtain

$$T_2 = \varphi^*(T^{(N)}/T^{(M)}u_{\lambda_0}). \tag{12}$$

Formulas (10)–(12) solve the task of generalization of the classical DT to an arbitrary Sturm–Liouville operator (for a fixed p, we put $T^{(K)}u_{\lambda_0} = 1$ and consider φ^* as the identity).

Now let us briefly address the solvability of condition (9). As can be readily seen, this condition is equivalent to the integral relation

$$\int^y r\,dy = \int^x r(T^{(K)}u_{\lambda_0})^2 dx. \tag{13}$$

Representing the transformation $T^{(K)}$ in the form of a composition of first-order transformations, calculation of the right-hand part of Eq. (13) via K-fold integration by parts can be reduced to the calculation of the integral of $ru_{\lambda_0}^2$. Each separate step in this procedure is based on the identity

$$\int_{x_0}^x r(T^{(K)}u_\lambda)^2 dx = r\sqrt{p}u_\lambda T^{(1)}u_\lambda\big|_{x_0}^x - (\lambda - \lambda_1)\int_{x_0}^x ru_\lambda^2 dx, \tag{14}$$

which can be readily verified. In many cases (including those considered below), the integrals of r and $ru_{\lambda_0}^2$ can be calculated in the analytical form.

Now let us apply the generalized DT to the description of linear barotropic wave propagation in narrow channels. The wave amplitude in the case of harmonic oscillations satisfies the equation $Lu_\lambda = \lambda u_\lambda$. Below,

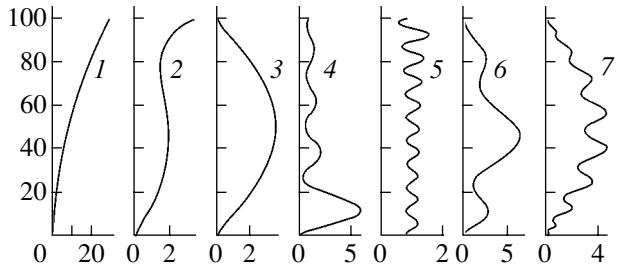

Fig. 1. Channel depth profiles constructed using *N*-order DT at a constant width for $N = 1$ (*1–3*), 2 (*4*, *5*), and 3 (*6*, *7*).

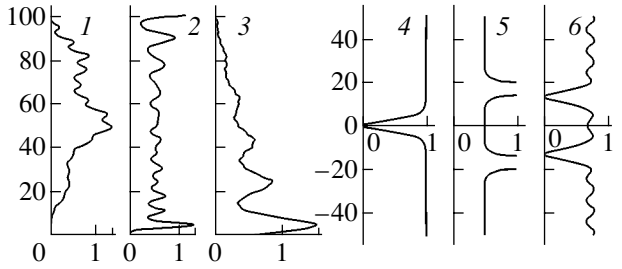

Fig. 2. Channel width profiles constructed using *N*-order DT at a constant depth for $N = 4$ (*1–3*), 1 (*4*), and 2 (*5*, *6*).

r and p will refer to the channel width and depth, respectively; $q = 0$; $\lambda = -\omega^2/g$; ω is the oscillation frequency; and g is the acceleration of gravity. The quantities entering into operator L will be considered dimensionless; this operator with $r = p = 1$will be used as initial for the DT. The new coefficients and the new transformation operator are calculated using formulas (11) and (22) with $T^{(M)} = T^{(N)}$.

Now we will demonstrate the wide possibilities of the generalized DT as a means of constructing exactly solvable channel width and depth profiles. Let us begin with the first-order DT and write explicit expressions (11) and (12) using the transformation functions of the following type: $u_{\lambda_i} = a_i\cos(k_i x + \alpha_i)$, where a_i, k_i, and α_i are constants and $i = 0, 1$. In the case when only the channel width is subjected to the transformation, we have

$$r_2 = a_0^2[-k_0\sin(k_0x + \alpha_0) + k_1\cos(k_0x + \alpha_0)\tan(k_1x + \alpha_1)]^2, \quad p_2 = 1, \tag{15}$$

$$T_2u_\lambda = \frac{du_\lambda/dx + k_1\tan(k_1x + \alpha_1)u_\lambda}{-k_0\sin(k_0x + \alpha_0) + k_1\cos(k_0x + \alpha_0)\tan(k_1x + \alpha_1)}. \tag{16}$$

In contrast, when only the channel depth is subjected to the transformation, we obtain (in terms of variable x)

$$r_2 = 1, \quad p_2 = a_0^4(-k_0\sin(k_0x + \alpha_0) + k_1\cos(k_0x + \alpha_0)\tan(k_1x + \alpha_1))^4, \tag{17}$$

and the expression for T_2 is given by (16). The relation with variable y can be found from Eqs. (13) and (14), which yields

$$y = a_0^2\left\{\cos(k_0x + \alpha_0)[-k_0\sin(k_0x + \alpha_0) + k_1\cos(k_0x + \alpha_0)\tan(k_1x + \alpha_1)] + \frac{1}{2}(k_0^2 - k_1^2)[k_0^{-1}\cos(k_0x + \alpha_0)\sin(k_0x + \alpha_0) + x]\right\} + \text{const}. \tag{18}$$

In both cases, direct substitution shows that T_2u_λ is in fact the eigenfunction of L_2 for the eigenvalue λ–λ_0.

By varying the parameters k_0, k_1, α_0, and α_1, we obtain a family of the channel width and depth profiles. Figure 1 shows three examples (curves *1–3*) of such profiles, which have shapes typical (in particular with respect to the number of extrema) of the whole family. The required interval of variation for y is determined by selecting a_0 and the integration constant in formula (18). We adopt this interval, that is, the channel length (depth) equal to 100 (as indicated in the ordinate axis in Fig. 1), and the abscissa represents the channel depth (width).

As the DT order is increased, the spectrum of channel width and depth profiles significantly expands. This is illustrated in Fig. 1 (curves *4–7*) and Fig. 2 (curves *1–3*). It should be noted that, in a broad range of variation of the DT parameters, the channel width profile obtained at a fixed depth and the corresponding channel depth profile obtained at a fixed width (we imply correspondence of the (15) ⟶ (17) type) coincide in shape. Beginning with the third-order DT, it is possible to model the "fine" structure of the channel profiles, that is, to impose high-frequency perturbations on the previously constructed profiles. The perturbation is obtained by applying an appropriate even-order DT (with the corresponding profile). For example, the profiles depicted by curves *6* and *7* in Fig. 1 are obtained by perturbing curve *3* with the profiles depicted by curves *4* and *5*, respectively. Possibilities of the fourth-order DT are illustrated in Fig. 2 (curves *1–3*). The transformation functions can be selected in the form of real exponents. This choice leads to profiles illustrated in Fig. 2 (curves *4–6*).

The limited volume of this publication does not allow us to dwell in detail on the case when both width

and depth of the channel are subjected to transformation. In this respect, we may only note that, in a broad range of variation of the transformation parameters, the channel width profiles obtained for the constructed depth profile can be varied in shape to within approximately the same limits as in the case of constant depth.

Acknowledgments. This study was supported by the Presidium of the Russian Academy of Sciences (Program no. 17).

REFERENCES

1. V. G. Bagrov and B. F. Samsonov, Teor. Mat. Fiz. **104**, 356 (1995).
2. V. G. Bagrov and B. F. Samsonov, Élem. Chast. At. Yadra **28**, 951 (1997).
3. V. B. Matveev and M. A. Salle, *Darboux Transformations and Solitons* (Springer, Berlin, 1990).
4. L. M. Berkovich, *Factorization and Transformations of Ordinary Differential Equations* ("Center for Regular and Chaotic Dynamics," Moscow, 2002) [in Russian].
5. A. A. Suzko, Int. J. Mod. Phys. A **12**, 277 (1997).
6. H. Lamb, *Hydrodynamics*, 6th ed. (Cambridge University Press, Cambridge, 1932).

Translated by P. Pozdeev

Technical Physics Letters, Vol. 31, No. 9, 2005, pp. 756–758. Translated from Pis'ma v Zhurnal Tekhnicheskoĭ Fiziki, Vol. 31, No. 17, 2005, pp. 77–82.

Polarization Aberrations of Radiation at the Lens Focus

A. L. Sokolov

Moscow Power Engineering Institute (State University), Moscow, Russia

e-mail: universe@mpei.ac.ru

Received March 15, 2005

Abstract—The polarization aberrations of radiation at the lens focus are calculated with allowance for diffraction effects. Calculations are performed using the representation of radiation as a coherent set of Hermite–Gauss modes with certain amplitudes, phases, and polarizations. An expression for the longitudinal field component at the lens focus is obtained. © *2005 Pleiades Publishing, Inc.*

Polarization aberrations are distortions in the radiation polarization structure, which detrimentally influence the parameters of optical systems (e.g., of polarization microscopes) employing short-focus lenses. The polarization aberrations of radiation are usually considered within the framework of the ray optics with neglect of the diffraction effects [1]. According to the method of polarization wave matrices [2], radiation is represented as a coherent set of Hermite–Gauss modes with certain amplitudes, phases, and polarizations. Using this representation, it is possible to calculate the polarization aberrations of laser radiation with allowance for the diffraction and, in particular, to solve the intrinsic polarization problem for optical resonators [3].

This Letter demonstrates that, using the above method, it is possible to determine the radiation intensity distribution in the focal plane of a lens. In order to simplify the calculation, let us restrict the analysis to a one-dimensional problem and consider a linearly polarized plane wave incident onto a flat-convex cylindrical lens. The optical surface curvature radius in the *XOZ* meridional plane is *R* (Fig. 1), and the plane of oscillations of the electric vector **E** in the incident wave makes an angle of 45° with the *XOZ* plane ($E_x = E_y$). Since the angle of light incidence onto the output surface of the lens varies as $\theta_i = \arcsin(x/R)$, the transmission coefficients for the orthogonal components of **E** ($T_x(x)$ for E_x and $T_y(x)$ for E_y) also depend on the coordinate *x*. Expanding E_x over the Hermite–Gauss modes and taking into account their orthogonality, we obtain the following expansion coefficients U_{mx}:

$$U_{mx} = \frac{\int_{-\infty}^{+\infty} T_x(x)\exp(-x^2/w_x^2)H_m(\sqrt{2}x/w_x)dx}{\int_{-\infty}^{+\infty} \exp(-2x^2/w_x^2)[H_m(\sqrt{2}x/w_x)]^2 dx}, \quad (1)$$

where H_m are the Hermite polynomials of the argument $\sqrt{2}x/w_x$ and w_x is the beam radius in the *XOZ* plane (determined from the condition of intensity decrease e^2 times relative to that at the beam axis). By the same token, we can write an expression for the coefficients of the expansion of the E_y component. The parameter w_x depends on the ratio D/N, where *D* is the lens diameter and *N* is the number of modes. For example, $w_x \approx D/8.8$ for $N = 10$ and $w_x \approx D/9.7$ for $N = 12$. In the case under consideration, the radiation intensity distribution behind the lens is determined by coherent superposition of only the even Hermite–Gauss modes. On the passage from the center to periphery of the lens, the E_x component increases and the E_y component decreases; at the lens edge, the field sharply drops to zero.

Let us determine the radiation intensity distribution in the focal plane of the lens for ten even modes

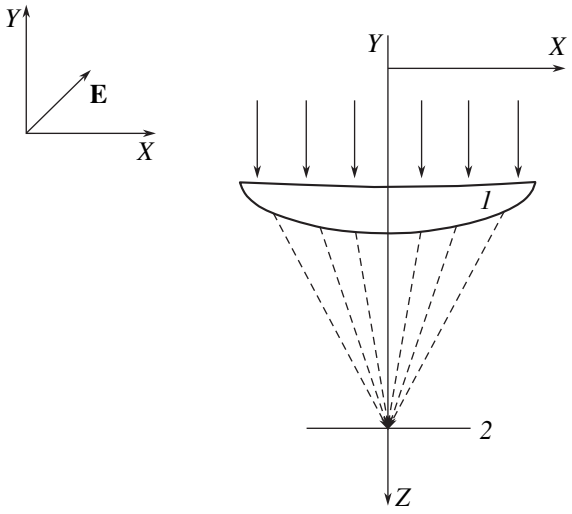

Fig. 1. Schematic diagram showing (*1*) a cylindrical flat-convex lens and (*2*) the focal plane where the diffraction pattern is observed.

1063-7850/05/3109-0756$26.00 © 2005 Pleiades Publishing, Inc.

($N = 10$). In short-focus lenses, which are of most interest for the calculation of polarization aberrations, the waist position for each mode coincides to a high precision with the rear focal plane of the lens. The phase increment for each even mode is a multiple of $\pi/2$: $\Phi_m = (m + 1)\pi/2$, so that the phase difference between adjacent even modes is π. This implies that, in the case of summing the electric field components for all modes in the focal plane, the components of adjacent modes enter the sum with opposite signs: $E'_x(f) = E'_{x0} - E'_{x2} + E'_{x4} - \ldots$. The orthogonal component is calculated in a similar manner.

With neglect of the polarization aberrations ($T_x \cong T_y$), the radiation intensity distribution $I'_0(x)/I'_0(0)$ at the lens focus coincides up to the fifth-order peaks with the theoretical dependence for the Fraunhofer diffraction on a slit. Figure 2 (curve *1*) shows such a distribution calculated for $f = 10$ mm, $D = 8.8$ mm, and $N = 10$. The distributions calculated with allowance for the polarization aberrations are shifted relative to the $I'_0(x)/I'_0(0)$ curve. The relative intensities at the maxima for $I'_x(x)/I'_0(0)$ (curve *2*) are greater than for $I'_y(x)/I'_0(0)$ (curve *3*). Thus, the size of the central maximum and its amplitude in the focal plane depend on the state of polarization of the incident radiation.

Now let us calculate the longitudinal component E_z of the **E** vector at the lens focus. This component is usually ignored because its intensity is several orders of magnitude lower than those of the transverse components. Taking into account that div**E** = 0 (or $-\partial E_z/\partial z = \partial E_x/\partial x + \partial E_y/\partial y$), we obtain the following approximate expression for the E_z component of the fundamental mode:

$$E_z \approx \frac{i}{k}\left(\frac{\partial E_x}{\partial x} + \frac{\partial E_y}{\partial y}\right) = x(\rho_x - i\omega_x)E_x + y(\rho_y - i\omega_y)E_y, \quad (2)$$

where ρ_x and ρ_y are the wave front curvatures in the *XOZ* and *YOZ* planes, respectively; λ is the wavelength; $\omega_x = 2/kw_x^2$; and $\kappa = 2\pi/\lambda$. The longitudinal component E_z of the fundamental mode at the waist on the *XOZ* plane is $E_z \approx -ix\lambda E_x/\pi w_{0x}^2$, where $E_x = E_0\exp(-x^2/w_{0x}^2)$. It should be noted that the absolute value of E_z reaches a maximum at $x = w_{0x}\sqrt{2}/2$. It was shown [4] that this method of determining E_z follows from a solution of the parabolic equation in vector form.

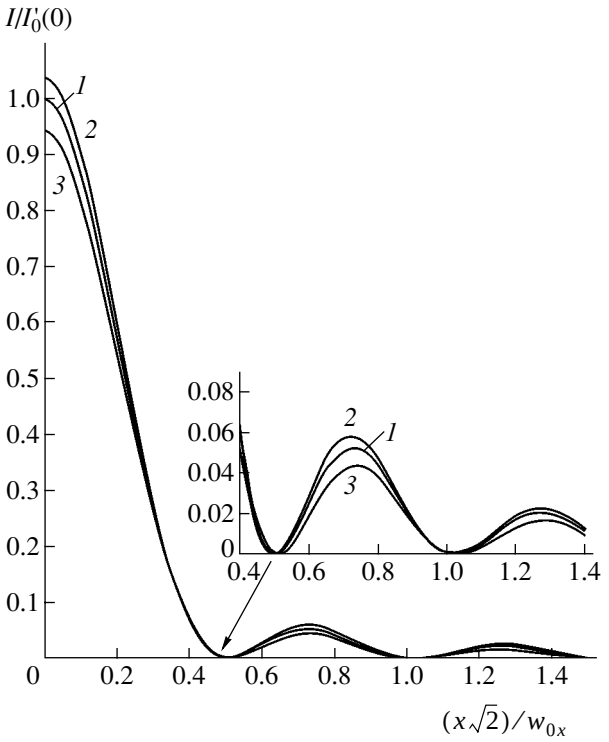

Fig. 2. Radiation intensity distributions in the focal plane of the lens calculated for $f = 10$ mm, $D = 8.8$ mm, and $N = 10$: (*1*) $I'_0(x)/I'_0(0)$; (*2*) $I'_x(x)/I'_0(0)$; (*3*) $I'_y(x)/I'_0(0)$.

The expression for the longitudinal component of the transverse mode of an arbitrary order *m* is as follows:

$$E_{zm} \approx \frac{\sqrt{2}i\lambda E_0}{\pi w_{0x}} \times \left[mH_{m-1}(\sqrt{2}x/w_{0x}) - \frac{1}{2}H_{m+1}(\sqrt{2}x/w_{0x})\right]\exp(-x^2/w_{0x}^2). \quad (3)$$

Using this expression, it is possible to calculate the intensity $I_z(x)$ of the longitudinal component in the focal plane of a cylindrical lens. Figure 3 shows this dependence calculated for ten even modes in the field representation. As can be seen from Eq. (3), the longitudinal component is nonzero at the beam axis, which was previously demonstrated for radially polarized beams [5].

Radiation transmitted through a lens with polarization aberrations becomes inhomogeneously polarized, whereby its ellipsometric parameters depend on both transverse and longitudinal coordinates. In the focal plane, the polarization azimuth varies long the *X* axis. At the optical axis, the slope of the **E** vector decreases (below 45° in the incident beam) despite the fact that the transmission coefficients for both field components at $x = 0$ coincide. This behavior is related to the fact that the lens on the whole transmits the *x* component better,

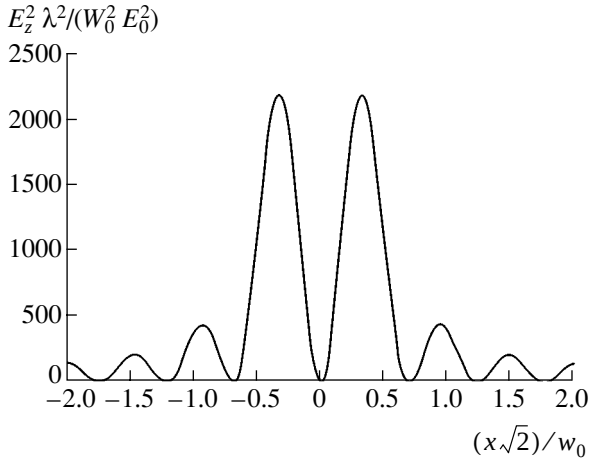

Fig. 3. A radial profile of the longitudinal field component intensity in the focal plane of a cylindrical lens.

so that the energy of a wider beam of this component is concentrated on a smaller area in the focal plane.

The above results can be generalized to the case of a spherical lens. If a linearly polarized radiation is incident on such a lens, the focal spot contracts in the direction of the **E** vector, and an orthogonal **E** component appears that is described by the TEM_{11} mode. The light with a circular polarization retains the spot shape at the lens focus. In the general case, the incident radiation acquires inhomogeneous elliptic polarization even in the absence of phase-dependent polarization devices.

By calculating the parameters of modes forming the inhomogeneously polarized radiation, it is possible to determine the polarization structure of radiation in an arbitrary optical system producing polarization aberrations.

REFERENCES

1. P. I. Lamekin and K. G. Predko, Kvantovaya Élektron. (Moscow) **9**, 2030 (1982).
2. A. L. Sokolov, Opt. Spektrosk. **83**, 1005 (1997) [Opt. Spectrosc. **83**, 930 (1997)].
3. V. N. Kuryatov and A. L. Sokolov, Kvantovaya Élektron. (Moscow) **32**, 324 (2002).
4. A. M. Bel'skii, T. M. Korneichik, and A. P. Khapalyuk, *Spatial Structure of Laser Radiation* (Belarus. State University, Minsk, 1982) [in Russian].
5. A. V. Nesterov and V. G. Niziev, J. Phys. D: Appl. Phys. **33**, 1817 (2000).

Translated by P. Pozdeev

Technical Physics Letters, Vol. 31, No. 9, 2005, pp. 759–761. Translated from Pis'ma v Zhurnal Tekhnicheskoĭ Fiziki, Vol. 31, No. 17, 2005, pp. 83–88.

Self-Organization of Nanoislands on the Surface of Silicon and Gallium Arsenide Single Crystals Stimulated by Spatially Periodic Laser Radiation Fields

Yu. K. Verevkin*, É. Ya. Daume, V. N. Petryakov, Yu. Yu. Gushchin, and S. V. Tikhov

Institute of Applied Physics, Russian Academy of Sciences, Nizhni Novgorod, Russia
Nizhni Novgorod State University, Nizhni Novgorod, Russia
** e-mail: verevkin@appl.sci-nnov.ru*

Received March 15, 2005

Abstract—Four interfering laser beams acting upon the surface of silicon and gallium arsenide single crystals stimulate the self-organization of nanoislands, which is manifested by the development of processes controlling the size of islands in a two-dimensional periodic structure formed on the sample surface. The influence of the polarization of interfering beams on the character of this self-organization has been studied. Islands with lateral dimensions from 60 to 100 nm and a height of 6–12 nm have been obtained. The lateral dimensions of nanoislands are 5–10 times smaller than the period of a standing wave of the laser radiation field, which is explained by the influence of elastic stresses developed at the crystal surface. © *2005 Pleiades Publishing, Inc.*

It is well known that the self-organization of nanostructures (SONS) is an important factor leading to a significant improvement in the characteristics of semiconductor lasers [1]. This phenomenon is also of considerable interest in many other aspects of the development of basic science and nanotechnology [2]. In recent years, extensive investigations have been devoted to finding the optimum conditions of SONS for various materials [3–6].

One promising direction of such investigations is the search for conditions providing the formation of spatially periodic arrays of nanoislands with lateral dimensions below 100 nm [7–10]. Such surface structures are usually obtained with the aid of various masks or specially pretreated substrates with a certain surface relief. Pedraza *et al.* [11] studied the self-organization of nanoislands on Si under the action of high-power UV radiation in the regime of surface wave excitation. The SONS regime was obtained upon the action of more than 200 laser pulses with an energy of about 1 J/cm^2. Patella *et al.* [12] studied the self-organization of quantum dots in the Si–Ga/Si and InAs/GaAs systems with flat and structured substrates.

This Letter presents the results of investigations aimed at establishing conditions for the formation of two-dimensional periodic structures of nanoislands on the surface of commercial (100)-oriented single crystal silicon (KEF-4 grade) and GaAs (AGChO-1 grade) after standard pretreatment.

The sample surface was exposed to four coherent beams of XeCl laser radiation. Previously, this method of action upon the surface of materials was successfully used for the local nanodimensional modification of paramagnetic films with their conversion into a ferromagnetic state [13]. The distribution of radiation in a standing wave field significantly depends on the polarization of interfering laser beams. We used two variants of beam polarization: TE–TE and TE–TM (for more detail see [14]). The results presented below were obtained using a single laser pulse with a duration of 10 ns and an intensity of 1–1.5 J/cm^2.

Figure 1 shows the typical image of a Si(100) crystal surface upon the action of four laser beams with TE–TE polarizations. The image and two surface profiles corresponding to scans in the directions indicated by solid lines *1* and *2* were obtained using an atomic force microscope (AFM). The standing wave structure in this case corresponds to a sum of two mutually perpendicular bands. In accordance with this distribution, nanoislands with a diameter of 40–60 nm (see profiles *1* and *2*) appeared at the sites of maximum radiation field intensity. The islands are separated by extended sloped regions with dimensions 30×150 nm. An interesting feature of the self-organization in this regime consists in the appearance of wells of various shapes and dimensions near the islands (hills). The wells have lateral dimensions above 30 nm and a depth of 4–6 nm. As can be seen from Fig. 1, the wells are situated on different sides of the neighboring islands. This character of modification of the crystal surface significantly differs from the results of laser action upon the surface of amorphous materials [14], where symmetric hills are formed around the wells.

1063-7850/05/3109-0759$26.00 © 2005 Pleiades Publishing, Inc.

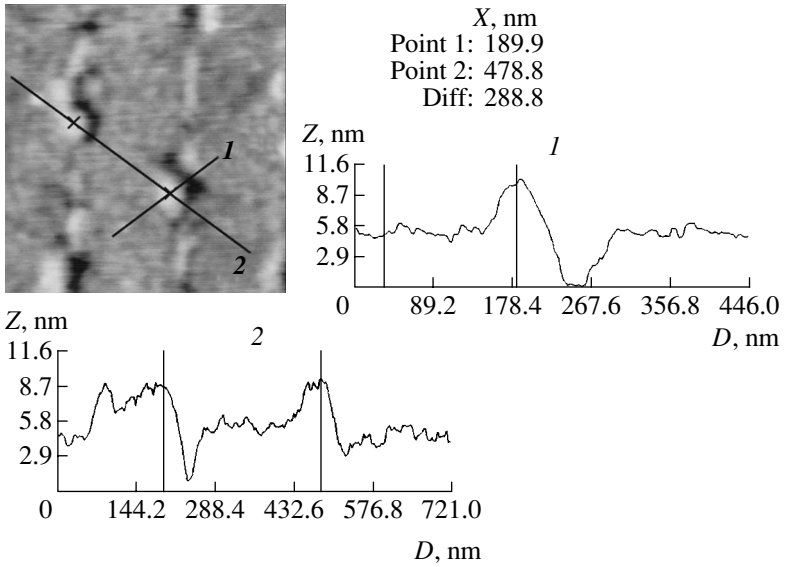

Fig. 1. An AFM image of Si(100) surface after the action of four pulsed UV laser beams (two pairs of beams in the vertical and horizontal planes) with TE–TE polarizations. The surface profiles *1* and *2* were obtained by scans in the directions indicated by the corresponding lines in the image.

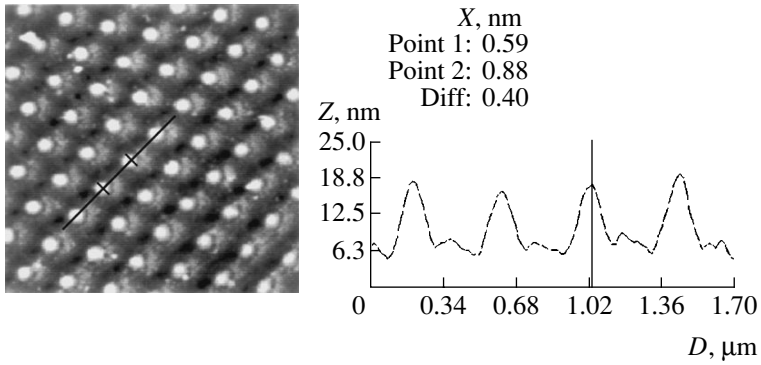

Fig. 2. An AFM image of Si(100) surface after the action of four pulsed UV laser beams (two TE-polarized beams in the horizontal plane and two TM-polarized beams in the vertical plane). The surface profile was obtained by scans in the direction indicated by the line in the image.

A substantially different character of self-organization was observed in the case of interference of the beams with TE–TM polarizations. In this case, the sites of maximum intensity are highly localized and surrounded by lines of zero intensity. This field intensity distribution leads to a clearer localization of the nanoislands. Figure 2 presents the typical AFM image of the surface of silicon treated in this regime and shows a surface profile in the direction indicated by the line. The image reveals a clear two-dimensional periodic structure of islands with diameters below 100 nm and a height of 12 nm. It should be noted that all islands in this structure are situated on the same side of the adjacent wells, which indicates that the conditions of diffusion for silicon atoms are the same on the AFM image scale.

Figure 3 presents an AFM image of a GaAs(100) single crystal surface upon the action of interfering laser beams with TE–TM polarizations and shows a surface profile in the direction indicated by the line. The islands observed on the GaAs surface have lateral dimensions about 60 nm and a height of ~7 nm. The surface profile shows that the positions of islands exhibit a spread within 30 nm.

The results presented above show that the minimum lateral size of the islands is 5–10 times smaller than the period of a standing wave of the laser radiation field. In the case of laser action upon amorphous or polycrystalline films [15, 16], the characteristic size of the region of modification usually amounts to 50% of the standing wave period. This significant difference between the results of laser action suggests that the laser modification of single crystals is significantly influenced by specific forces acting at the sample surface. We may suggest that these forces are related to the difference between the states of atoms on the surface and in the

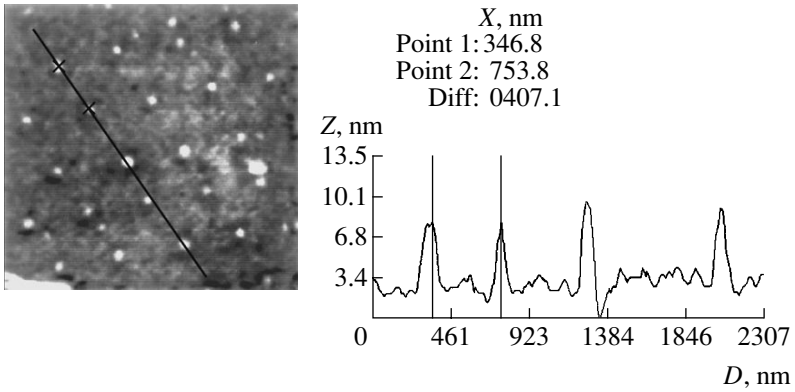

Fig. 3. An AFM image of GaAs(100) surface after the action of four pulsed UV laser beams (two TE-polarized beams in the horizontal plane and two TM-polarized beams in the vertical plane). The surface profile was obtained by scans in the direction indicated by the line in the image.

bulk of the crystal [1]. From this we infer that the formation of periodic structures described above is related to a local laser-induced heating and the stimulated diffusion of atoms in the elastic stresses developed in the surface layer of the crystal. These conditions make possible the formation of nanoislands with dimensions significantly smaller than the standing wave period.

In conclusion, the results of our experiments show the possibility of controlled self-organization of two-dimensional structures of nanoislands on the surface of Si and GaAs crystals under the action of several polarized coherent laser beams. Such structures can be used in semiconductor electronics for obtaining lasers emitting in the direction perpendicular to the cavity surface. Now we are planning to study the self-organization of nanoislands formed under optimum conditions for the surface electromagnetic wave excitation.

REFERENCES

1. N. N. Ledentsov, V. M. Ustinov, V. A. Shchukin, *et al.*, Fiz. Tekh. Poluprovodn. (St. Petersburg) **32**, 385 (1998) [Semiconductors **32**, 343 (1998)].
2. *Nanotechnology Research Directions*, Ed. by M. K. Roko, R. S. Ul'yamsa, and P. Alivisatos (Kluwer Academic, Dordrecht, 2000; Mir, Moscow, 2002).
3. V. M. Ustinov, Fiz. Tekh. Poluprovodn. (St. Petersburg) **38**, 963 (2004) [Semiconductors **38**, 923 (2004)].
4. N. V. Kryzhanovskaya, A. G. Gladyshev, S. A. Blokhin, *et al.*, Fiz. Tekh. Poluprovodn. (St. Petersburg) **38**, 867 (2004) [Semiconductors **38**, 833 (2004)].
5. B. N. Zvonkov, I. A. Karpovich, N. V. Baidus', *et al.*, Fiz. Tekh. Poluprovodn. (St. Petersburg) **35**, 92 (2001) [Semiconductors **35**, 93 (2001)].
6. A. Sgartato, P. D. Szkutnik, A. Balzarotti, *et al.*, Appl. Phys. Lett. **83**, 4002 (2004).
7. T. Kitajima, B. Lu, and S. R. Leone, Appl. Phys. Lett. **80**, 497 (2002).
8. G. Capellini, M. De Seta, C. Spinella, and F. Evangelisti, Appl. Phys. Lett. **82**, 1772 (2003).
9. Z. Zhoug, A. Halilovic, T. Fromherz, *et al.*, Appl. Phys. Lett. **82**, 4779 (2003).
10. Q. Li, S. M. Han, S. R. J. Bruek, *et al.*, Appl. Phys. Lett. **83**, 5032 (2003).
11. A. J. Pedraza, J. D. Fowlkes, and Y.-E. Guan, Appl. Phys. A **77**, 277 (2003).
12. F. Patella, A. Szkutnik, and E. Sgarlata, J. Phys.: Condens. Matter **16**, S1503 (2004).
13. A. M. Alekseev, Yu. K. Verevkin, N. V. Vostokov, *et al.*, Pis'ma Zh. Éksp. Teor. Fiz. **73**, 214 (2001) [JETP Lett. **73**, 192 (2001)].
14. V. I. Bredikhin, Yu. K. Verevkin, E. Ya. Daume, *et al.*, Kvantovaya Élektron. (Moscow) **30**, 333 (2000).
15. Yu. K. Verevkin, N. G. Bronnikov, V. V. Korolikhin, *et al.*, Zh. Tekh. Fiz. **73** (6), 99 (2003) [Tech. Phys. **48**, 757 (2003)].
16. V. I. Bredikhin, V. N. Burenina, Yu. K. Verevkin, *et al.*, Zh. Tekh. Fiz. **74** (9), 86 (2004) [Tech. Phys. **49**, 1191 (2004)].

Translated by P. Pozdeev

Technical Physics Letters, Vol. 31, No. 9, 2005, pp. 762–764. Translated from Pis'ma v Zhurnal Tekhnicheskoĭ Fiziki, Vol. 31, No. 17, 2005, pp. 89–94.

The Effect of Treatment in a Pulsed Magnetic Field on the Kinetics of Oxidation of Indium Phosphide Crystals

M. N. Levin*, G. V. Semenova, A. V. Tatarintsev, and O. N. Shumskaya

Voronezh State University, Voronezh, Russia

** e-mail: levin@phys.vsu.ru*

Received March 25, 2005

Abstract—It is demonstrated that preliminary treatment of semiconductors (for example, indium phosphide) in a pulsed magnetic field can increase the rate of surface chemical reactions (in particular, oxidation). © *2005 Pleiades Publishing, Inc.*

Previously, it was reported [1, 2] that a short-term action of pulsed magnetic fields (PMFs) induced long-term nonmonotonic variations in the structure and physical properties of semiconductor crystals. In particular, a high sensitivity to the action of magnetic fields was observed for the near-surface layers of semiconductors. Indeed, weak magnetic fields induced the outdiffusion of oxygen dissolved in the bulk of silicon crystals and the segregation of oxygen in their surface layers [3], which resulted in a significant modification of the adsorption properties of the sample surface [4, 5]. Our investigations of the crystals of Sb–As solid solutions upon a short-term PMF action revealed the subsequent long-term redistribution of components at room temperature. These events included the segregation of antimony with the formation of surface clusters, the decomposition of Sb clusters, and the gradual loss of Sb from the surface [6]. Investigations of the effect of PMFs on weakly dislocated undoped $A^{III}B^{V}$ semiconductor crystals [7] showed that the initial stage of this interaction involves the segregation of a Group III component at the crystal surface and the formation of clusters of this metal.

Evidently, a change in the phase, structure, and thermodynamic state of the surface of a semiconductor crystal under PMF action may also significantly influence the chemical activity of this surface and the kinetics of solid-phase processes involving the surface layers.

This paper presents the results of investigations of the effect of pretreatment in a pulsed magnetic field on the kinetics of low-temperature chemical oxidation of indium phosphide (InP) crystals.

Experimental. The experiments were performed with ⟨111⟩-oriented polished plates of *n*-InP with a charge carrier density of 10^{16} cm^{-3}. The plates were oxidized using the well-known method [8] of low-temperature oxidation in concentrated nitric acid in the presence of iodine, which ensured the formation of homogeneous dielectric films free of additional structural defects (typically induced by high-temperature oxidation processes). Preliminary treatment of the plates prior to oxidation included chemical polishing for 20 min with a H_2SO_2–H_2O_2–H_2O (3 : 1 : 1) etchant, washing in distilled water, treatment in a 0.1% hydrochloric acid solution, rinsing in distilled water, and final drying.

The test plates prepared as described above were subjected to the PMF action. The PMF treatment consisted in exposure to a series of 1500 unipolar symmetric triangular pulses with an amplitude of $B = 0.3$ T, a duration of $\tau = 4 \times 10^{-5}$ s, and a repetition rate of $f = 50$ Hz. The magnetic field pulses were generated by discharge of a capacitor bank through a low-inductance solenoid coil. The PMF treatment was performed in air at room temperature. Then, the test samples were stored at room temperature in an inert atmosphere, together with the control plates not treated in the PMF. The time of storage prior to oxidation was varied from 1 to 20 days.

The test and control InP plates were fixed in quartz sample holders and simultaneously oxidized in a cylindrical jar containing a fresh working solution prepared by dissolving iodine (0.02 g) in concentrated nitric acid. The oxidation was carried out in a thermostat set at 313 K for a period of time varied from 5 to 25 min. After oxidation, the test and control samples were washed with distilled water and dried. The oxide layer thickness was determined by laser ellipsometry. These measurements were performed with a LEF-3M ellipsometer (Russia). The error of determination of the angles of rotation for the polarizer, compensator, analyzer, and working arms was ±1 min or arc.

The structure of the oxide films was studied by X-ray diffraction using a DRON-3 diffractometer (Russia) using CuK_α radiation ($\alpha = 1.54178$ nm). The measurements were performed in the regime of automated angular scanning with a step of 0.1°, 3-s exposure at each point, and sample rotation in the intrinsic plane.

1063-7850/05/3109-0762$26.00 © 2005 Pleiades Publishing, Inc.

The dielectric strength of the oxide film was determined with the aid of a capacitor structure formed immediately on the sample surface without any additional thermal treatments. For this purpose, aluminum electrodes with a diameter of 0.8 mm and a thickness of ~500 nm were formed by thermal evaporation and deposition in vacuum via a molybdenum mask at a residual pressure not exceeding 10^{-3} Pa. The ohmic contact with the substrate was provided by mechanical application of an indium–gallium eutectic mixture onto the rear side of each sample.

Results. Figure 1 shows the kinetics of isothermal oxidation of InP plates stored for various periods of time between the PMF treatment and the onset of oxidation. An analysis of these curves showed that the oxidation process can be described in terms of the well-known kinetic equation [8]

$$d = (kt)^n, \quad (1)$$

where d is the oxide thickness increment [nm], t is the time of exposure in the oxidizing medium [min], k is the process rate constant [$\text{nm}^{1/n}\ \text{min}^{-1}$], and n is the exponent. The value of n in Eq. (1) was the same for both test and control samples, $n \approx 0.5$, which indicates that the PMF treatment does not influence the mechanism of oxidation.

By determining the slope of the oxide layer growth kinetics (Fig. 1) plotted in d^2 versus t coordinates, we have evaluated the rate constants of chemical reactions proceeding on the surface of test and control InP plates. For the plates upon PMF treatment, the oxidation rate constant was $978 \pm 92\ \text{nm}^{1/2}\ \text{min}^{-1}$, which was higher than the value for the control plates $780 \pm 87\ \text{nm}^{1/2}\ \text{min}^{-1}$.

Figure 2 (curve *1*) shows evidence of a nonmonotonic character of the PMF effect on the InP oxidation rate. This character is analogous to that observed previously for the PMF influence on the adsorption capacity of semiconductor crystals of some other types [5]. The PMF effect on the oxidation rate is most pronounced in samples stored for 5–6 days after the treatment. A further increase in the duration of storage led to a decrease in the PMF effect until its virtually complete vanishing after 20 days. The PMF effect of the dielectric strength of the oxide films (Fig. 2, curve *2*) also exhibited a nonmonotonic variation with the storage time, which was correlated with the behavior of the PMF-induced intensification of the oxidation process.

The results of the X-ray phase analysis showed that oxide films formed on the control and test samples are multiphase and possess virtually identical phase compositions. The main oxide phases in these films were In_2O_3 (predominantly in the hexagonal modification) and P_2O_5 (various modifications). These results lead to the conclusion that the PMF treatment of InP plates does not influence the phase composition of oxide films formed in the course of their subsequent oxidation.

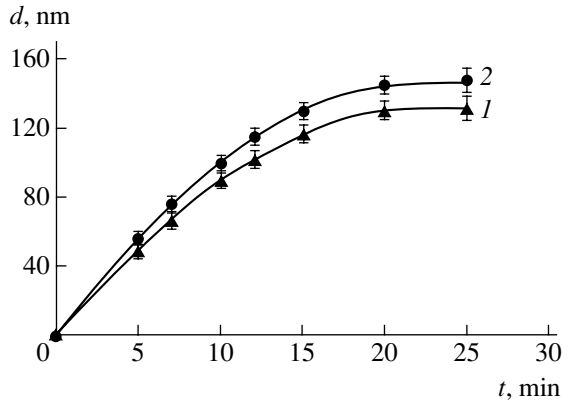

Fig. 1. Plots of the oxide film thickness versus oxidation time for InP plates (*1*) not treated in a PMF and (*2*) treated in a PMF and stored for five days prior to oxidation.

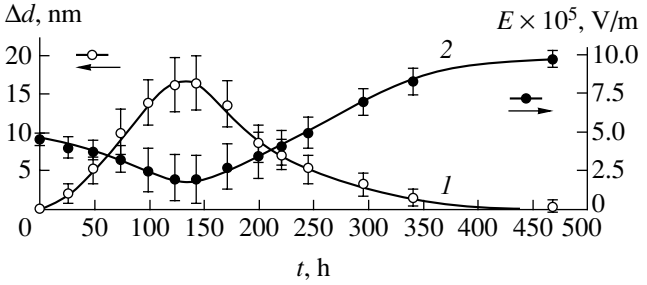

Fig. 2. Plots of the (*1*) a difference Δd of the oxide film thickness on the test (PMF-treated) and control samples and (*2*) breakdown field strength E (corresponding to a current of 10^{-6} A through the capacitor structure) versus the time of sample storage after the PMF treatment prior to the onset of oxidation (oxidation time in all cases 25 min).

Discussion. The observed increase in the rate of chemical oxidation of InP crystals as a result of their pretreatment in a PMF can be explained within the framework of a mechanism proposed previously [7], which was considered as accounting for the diffusion instability in the crystals of $A^{III}B^{V}$ semiconductor compounds.

According to this mechanism [7], the main factor responsible for the sensitivity of $A^{III}B^{V}$ semiconductor crystals with respect to the PMF is the complexes of intrinsic point defects capable of decomposing under the action of a weak magnetic field. A possible mechanism of the magnetic-field-induced decomposition of defect complexes was recently proposed in [9]. The formation of intrinsic defects in InP crystals is related primarily to the presence of an excess amount of vacancies of the volatile component (phosphorus), which are capable of forming complexes with the antistructural defects in InP. In the first stage, the PMF-induced decomposition of these defect complexes in depth of a crystal is accompanied by the appearance of mobile phosphorus vacancies diffusing from the bulk to the surface, which is the natural sink for the point defects.

The diffusion of phosphorus vacancies to the surface is equivalent to their "healing" in the bulk by atoms of phosphorus diffusing from the surface inward the crystal. The loss of phosphorus from the surface leads to the enrichment of the surface layer with the second component (indium). This segregation changes the surface topology, increases the number of structural defects in the subsurface layer, and produces activation of the surface, which results eventually in intensification of the oxidation reactions. This increase in the oxide layer growth rate is accompanied by an increase in the density of defects in the oxide film, which is manifested by a decrease in the dielectric strength of this film (Fig. 2).

The second stage features the diffusion of indium from the regions of its increased content at the surface to the bulk, which leads to the establishment of a more uniform distribution of components and to a decrease of the density of defects in the crystal. This is accompanied by a decrease in the surface activity and in the density of defects in the oxide film, which is manifested by an increase in the dielectric strength. The quality of the oxide films formed on the InP substrates pretreated in the PMF is higher than that of the control samples.

In conclusion, the results of our investigation showed that the action of a weak PMF leads to an increase in the chemical activity of the surface of semiconductors. This phenomenon can be used for the development of technologies involving the formation of high-quality films on the surface of semiconductor crystals.

REFERENCES

1. V. V. Kveder, Yu. A. Osip'yan, and A. I. Shalynin, Zh. Éksp. Teor. Fiz. **83**, 699 (1982) [Sov. Phys. JETP **56**, 389 (1982)].
2. M. N. Levin and B. A. Zon, Phys. Lett. A **260**, 386 (1999).
3. M. N. Levin and B. A. Zon, Zh. Éksp. Teor. Fiz. **111**, 1373 (1997) [JETP **84**, 760 (1997)].
4. M. N. Levin, V. N. Semenov, and A. V. Naumov, Pis'ma Zh. Tekh. Fiz. **27** (7), 35 (2001) [Tech. Phys. Lett. **27**, 279 (2001)].
5. M. N. Levin, A. V. Tatarintsev, O. A. Kostsova, and A. M. Kostsov, Zh. Tekh. Fiz. **73** (10), 85 (2003) [Tech. Phys. **48**, 1304 (2003)].
6. M. N. Levin, G. V. Semenova, T. P. Sushkova, *et al.*, Fiz. Tverd. Tela (St. Petersburg) **45**, 609 (2003) [Phys. Solid State **45**, 639 (2003)].
7. M. N. Levin, G. V. Semenova, and T. P. Sushkova, Dokl. Akad. Nauk **388**, 11 (2003) [Dokl. Phys. **48**, 62 (2003)].
8. I. M. Soshnikov and N. N. Dement'ev, Khim. Teor. Tekhnol., No. 2, 43 (1999).
9. V. I. Belyavsky and M. N. Levin, Phys. Rev. B **70**, 104101 (2004).

Translated by P. Pozdeev

Technical Physics Letters, Vol. 31, No. 9, 2005, pp. 765–766. Translated from Pis'ma v Zhurnal Tekhnicheskoĭ Fiziki, Vol. 31, No. 18, 2005, pp. 1–3.

Contact Melting of Lead-Based Solid Solutions and Metals

O. L. Enaldieva, T. A. Orkvasov, M. Kh. Ponezhev, and V. A. Sozaev*

Kabardino-Balkarian State University, Nalchik, Kabardino-Balkaria, Russia

** e-mail: sozaevv@kbsu.ru*

Received February 21, 2005

Abstract—The rates of melting of lead-based binary solid solutions A_xB_{1-x} (A = Pb; B = Bi, Sn, In, Ag, Li) in contact with metals (Sn, Bi) have been measured. A correlation between the rate of contact melting and the surface properties of solid solution components is established. © *2005 Pleiades Publishing, Inc.*

It has been reported that impurity atoms influence both the temperature and rate of contact melting, but the laws of such influence are still incompletely clear. We have attempted to establish a correlation between the rate of melting of metals in contact with lead-based binary solid solutions A_xB_{1-x}, on the one hand, and the surface properties of solid solution components, on the other hand.

In order to measure the rate of contact melting, the samples with polished edges were brought into contact in a glass tube. Then, the tube with the samples was placed in a thermostat and the contact melting was carried out in a nonstationary diffusion regime for 1 h at a temperature of 10 K above the eutectic point. Then, the samples were cooled, a longitudinal section was made, and the width Δx of the contact interlayer formed as a result of melting was measured with the aid of a microscope (MBS-10). The average rate of melting was calculated as $\langle v \rangle = \langle \Delta x \rangle / \Delta t$, where $\langle \Delta x \rangle$ is the average interlayer width and $\Delta t = 1$ h is the time of melting.

The rates of melting $\langle v \rangle$ in the contact between metals (Sn, Bi) and lead-based solid solutions (Pb–Bi, Pb–Sn, Pb–In, Pb–Ag, and Pb–Li) were compared to the surface properties of solid solution components, including the differences of their surface energies ($\Delta\sigma$), work functions ($\Delta\varphi$), and statistical generalized moments ($\Delta m^{(c)}$) according to Semenchenko [1, 2]. The plots of $\langle v \rangle$ versus these differential characteristics are presented in Figs. 1a–1c, respectively. The values of surface energies were taken from [3] and the values of work functions, from [4]. As can be seen from Fig. 1, the plots of $\langle v \rangle$ versus $\Delta\sigma$, $\Delta\varphi$, and $\Delta m^{(c)}$ are linear. This correlation indicates that the surface energy characteristics of solid solution components play an important role in the process of contact melting.

One possible reason for the observed correlation is related to the surface and grain boundary segregation of impurity atoms, which can lead to the formation of compositions similar to ternary eutectics (at the contact interface) and binary eutectics (at the grain boundaries). The degree of filling x^ω of the adsorption centers at the contact interface or at the grain boundaries by the impurity atoms can be described (for $x \ll 1$) using the Langmuir–McLean isotherm (see, e.g., [5]), Zhukhovitskiĭ isotherm [6], or Semenchenko isotherm [7]. According to this,

$$\frac{x^\omega}{1-x^\omega} \sim \exp[W/kT] \sim \exp[(\sigma_1 - \sigma_2)\omega_0/kT] \sim \exp[\gamma_\varphi(m_i - m_m)/kT], \quad (1)$$

where W is the energy (per atom) of the interaction

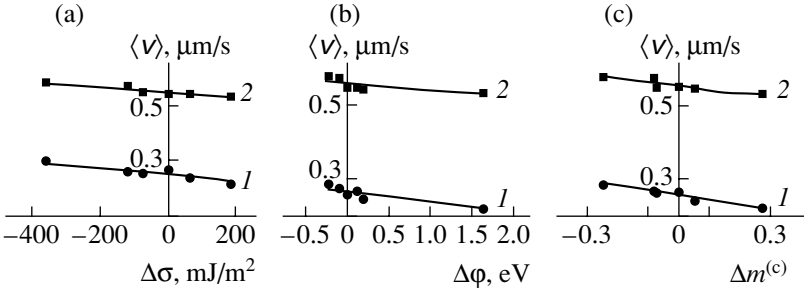

Fig. 1. Plots of the average contact melting rate $\langle v \rangle$ versus the difference of (a) surface energies $\Delta\sigma$, (b) work functions $\Delta\varphi$, and (c) statistical generalized Semenchenko moments $\Delta m^{(c)}$ of solid solution components for the contacts of Pb–0.1% Me (Me = Ag, Sn, Bi, In, Li) solid solutions with (*1*) Bi and (*2*) Sn.

1063-7850/05/3109-0765$26.00 © 2005 Pleiades Publishing, Inc.

between the impurity and the surface or grain boundary; k is the Boltzmann constant; T is the absolute temperature; σ_1 and σ_2 are the surface energies of the solid solution components; ω_0 is the contact (surface or grain boundary) area; m_i and m_m are the generalized moments (according to Semenchenko) of the impurity and matrix, respectively; and γ_φ is the difference of the molecular field strengths in the surface and bulk phases.

It should be noted that the surface energy σ of a metal system is proportional to the work function φ ($\sigma \sim \varphi$) [8] and the contact melting rate $\langle v \rangle$ is related to x^ω. Then, according to relations (1), $\langle v \rangle$ has to be proportional to W and, hence, to $\Delta\sigma$, $\Delta m^{(c)}$, and $\Delta\varphi$. This is confirmed by the data in Fig. 1.

REFERENCES

1. S. N. Zadumkin, Zh. Neorg. Khim. **5**, 1982 (1960).
2. N. L. Pokrovskiĭ, in *Thermophysical Properties of Metastable Systems* (Ural Division, Acad. Sci. USSR, Sverdlovsk, 1984), pp. 17–27 [in Russian].
3. A. B. Alchagirov, B. B. Alchagirov, T. M. Taova, and Kh. B. Khokonov, Trans. JWRI **30** (Special Issue), 287 (2001).
4. B. B. Alchagirov, Kh. Kh. Kalazhokov, and Kh. B. Khokonov, Poverkhnost, No. 7, 49 (1982).
5. B. S. Bokshteĭn and L. S. Shvindlerman, Preprint IFTT AN SSSR (Institute of Solid State Physics, Acad. Sci. USSR, Chernogolovka, 1978).
6. A. A. Zhukhovitskiĭ, Zh. Fiz. Khim. **17**, 313 (1943); **18**, 214 (1944).
7. V. K. Semenchenko, *Surface Phenomena in Metals and Alloys* (Gosizdat, Moscow, 1957; Pergamon, Oxford, 1962).
8. V. A. Sozaev and P. A. Chernyshova, Pis'ma Zh. Tekh. Fiz. **29** (2), 62 (2003) [Tech. Phys. Lett. **29**, 69 (2003)].

Translated by P. Pozdeev

Technical Physics Letters, Vol. 31, No. 9, 2005, pp. 767–769. Translated from Pis'ma v Zhurnal Tekhnicheskoĭ Fiziki, Vol. 31, No. 18, 2005, pp. 4–9.

Elastic Transverse Impact on an Orthotropic Plate

A. A. Loktev

Voronezh State University of Architecture and Civil Engineering, Voronezh, Russia

e-mail: prtlokt@yandex.ru

Received March 23, 2005

Abstract—The impact of a solid projectile via an elastic buffer on an orthotropic elastic plate possessing a cylindrical anisotropy has been numerically simulated. The dynamical behavior of the plate is described in terms of the Uflyand–Mindlin wave equations taking into account the rotary inertia and the transverse shear deformations. The wave equations are solved using the ray method and the matching of asymptotic expansions obtained for short times inside and outside the contact zone. The influence of the anisotropy of the plate material on the dynamic contact force and the plate inflection at the impact site has been studied. © *2005 Pleiades Publishing, Inc.*

The wave theory of impact used in this study is based on the Uflyand–Mindlin wave equations, which describe the dynamical behavior of a target plate with allowance for the rotary inertia of transverse sections and the transverse shear deformation [1, 2], and on the approach according to which a nonstationary transverse shear wave is generated at the moment of impact and then propagates at a finite velocity in the plate [3]. Previously, this approach was successfully used [4] in combination with the ray method to calculate the dynamics of the Uflyand–Mindlin isotropic elastic plate upon the transverse impact of a solid projectile via a nolinearly-elastic buffer. In this study, the procedure proposed in [4] has been generalized to describe the impact of a solid body on an orthotropic elastic plate via a linear elastic buffer.

Formulation of the problem and basic equations. Consider a solid projectile of mass m impinging at a velocity V_0 on the free end of a spring (buffer), the other end of which is fixed in a plate. The projectile is assumed to move along the spring axis, which is perpendicular to the plate surface (Fig. 1). It is also assumed that the spring does not lose stability in the course of deformation and obeys Hooke's law.

The dynamics of the round Uflyand–Mindlin orthotropic elastic plate possessing a cylindrical anisotropy will be described in a polar coordinate system using equations formulated in [5] and modified so as to take into account the rotary inertia of transverse sections and the transverse shear deformation. For the axisymmetric configuration, the wave characteristics are independent of the azimuthal angle φ and the basic equations can be written as

$$D_r\left(\frac{\partial^2\varphi}{\partial r^2}+\frac{1}{r}\frac{\partial\partial\varphi}{\partial r}\right)-D_\theta\frac{\varphi}{r^2}+hKG_{rz}\left(\frac{\partial w}{\partial r}-\varphi\right)=-\rho\frac{h^3}{12}\frac{\partial^2\varphi}{\partial t^2}, \quad (1)$$

$$KG_{rz}\left(\frac{\partial^2 w}{\partial r^2}-\frac{\partial\varphi}{\partial r}\right)+KG_{rz}\frac{1}{r}\left(\frac{\partial w}{\partial r}-\varphi\right)=\rho\frac{\partial^2 w}{\partial t^2}, \quad (2)$$

where $D_r = B_r h^3/12$, $D_\theta = B_\theta h^3/12$, $B_r = E_r/(1-\sigma_r\sigma_\theta)$, $B_\theta = E_\theta/(1-\sigma_r\sigma_\theta)$, $E_r\sigma_r = E_\theta\sigma_\theta$ (D_r and D_θ are the bending stiffnesses in the radial and polar directions, respectively; E_r, E_θ and σ_r, σ_θ are the elastic moduli and Poisson ratios, respectively, in the r and θ directions); $K = 5/6$; G_{rz} is the shear modulus in the rz plane; $w(r, \theta)$ is the normal displacement of the median plane; $\varphi(r, \theta)$ is an arbitrary (unknown) function of coordinates r and θ; ρ is the density; h is the plate thickness; and t is the time.

Method of solution. We assume that transverse impact gives rise to the longitudinal and transverse shear waves (Fig. 1), whose fronts are the surfaces of strong discontinuity propagating at the normal velocities $G^{(\alpha)}$ ($\alpha = 1, 2$ is the wave number). Let $Z(z_\alpha, t)$ be an arbitrary function to be determined. Behind the wave front Σ, this function can be presented in the form of a ray series:

$$Z(r,t)=\sum_{k=0}^{\infty}\frac{1}{k!}[Z,_{(k)}]_{t=r/G}\left(t-\frac{r-r_0}{G}\right)^k H\left(t-\frac{r-r_0}{G}\right), \quad (3)$$

1063-7850/05/3109-0767$26.00

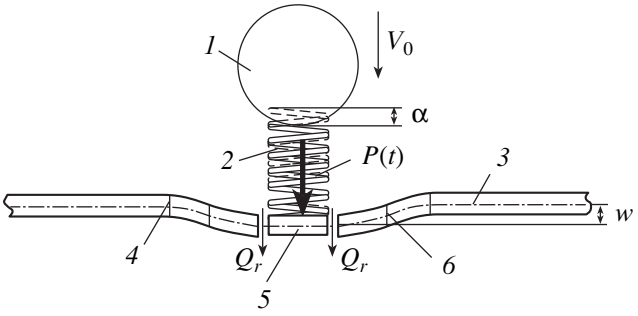

Fig. 1. Schematic diagram of the impact of a solid projectile via an elastic buffer on a plate: (*1*) projectile; (*2*) buffer; (*3*) plate; (*4*) quasi-longitudinal wave surface; (*5*) contact region; (*6*) quasi-transverse wave front.

where $[Z, {}_{(k)}] = Z^+, {}_{(k)} - Z^-, {}_{(k)} = [\partial^k Z/\partial t^k]$; $Z, {}_{(k)}$ is the jump of the kth order derivative of Z with respect to time t on the wave front Σ (i.e., at $t = (r - r_0)/G^{(\alpha)}$, r_0 being the initial radius); superscripts (+) and (–) refer to the values calculated in front of and behind the wave surface Σ, respectively; $H(t)$ is the Heaviside unit step function; and r is the arc length measured along the ray.

In order to determine the coefficients of series (3), it is necessary to differentiate the basic equations (1) and (2) k times with respect to time, calculate the differences of these derivatives on the opposite sides of the wave surface Σ, and use the conditions of matching for the $(k + 1)$-order jumps of the function Z with respect to time [3]:

$$G\left[\frac{\partial Z, {}_{(k)}}{\partial r}\right] = -[Z, {}_{(k+1)}] + \frac{\delta[Z, {}_{(k)}]}{\delta t}, \tag{4}$$

where $\delta/\delta t$ is the delta-derivative with respect to time. Applying this procedure to the equations of motion (1) and (2), we obtain a system of recurrent differential equations for the jumps to be determined (to within arbitrary constants):

$$\left(1 - \frac{\rho G^2}{B_r}\right)\omega_{\varphi(k+1)} = 2\frac{\delta\omega_{\varphi(k)}}{\delta t} + Gr^{-1}\omega_{\varphi(k)} + b_r G X_{w(k)} + F_{\varphi(k-1)}, \tag{5}$$

$$\left(1 - \frac{\rho G^2}{KG_{rz}}\right)X_{w(k+1)} = 2\frac{\delta X_{w(k)}}{\delta t} + Gr^{-1}X_{w(k)} - G\omega_{\varphi(k)} + F_{w(k-1)}, \tag{6}$$

where

$$X_{w(k)} = [w, {}_{(k+1)}],\ w_{\varphi(k)} = [\varphi, {}_{(k+1)}],$$

$$b_r = hKG_{rz}D_r^{-1},\ r = r_0 + Gt,$$

$$F_{\varphi(k-1)} = -\frac{\delta^2\omega_{\varphi(k-1)}}{\delta t^2} - Gr^{-1}\frac{\delta\omega_{\varphi(k-1)}}{\delta t} + G^2r^{-2}\frac{E_\theta}{E_r}\omega_{\varphi(k-1)} - b_r G\frac{\delta X_{w(k-1)}}{\delta t} + b_r G^2\omega_{\varphi(k-1)},$$

$$F_{w(k-1)} = -\frac{\delta^2 X_{w(k-1)}}{\delta t^2} - Gr^{-1}\frac{\delta X_{w(k-1)}}{\delta t} + G\frac{\delta\omega_{\varphi(k-1)}}{\delta t} + G^2r^{-1}\omega_{\varphi(k-1)}.$$

Putting $k = -1, 0, 1, 2$, and 3 in Eqs. (5) and (6), we obtain the jumps of the corresponding orders for the first and second waves. Using these quantities, the functions W and Q_r can be determined as segments of ray series (to within integration constants):

$$W \cong \sum_{\alpha=1}^{2}\sum_{k=0}^{4}\frac{1}{k!}X_{w(k)}^{(\alpha)}(y_\alpha)^k H(y_\alpha), \tag{7}$$

$$Q_r \cong KG_{rz}h\sum_{\alpha=1}^{2}\sum_{k=0}^{4}\frac{1}{k!}\left(-X_{(k)}^{(\alpha)}G^{(\alpha)-1} + \frac{\delta X_{(k-1)}^{(\alpha)}}{\delta t}G^{(\alpha)-1} - \omega_{(k-1)}^{(\alpha)}\right)(y_\alpha)^k H(y_\alpha), \tag{8}$$

where $y_\alpha = t - (r - r_0)G^{(\alpha)-1}$; the values of $X_{w(k)}^{(\alpha)}$, $\omega_{\varphi(k)}^{(\alpha)}$, and their delta-derivatives with respect to time are calculated for $y_\alpha = 0$.

Equations describing the impact. The interaction of a solid projectile with the buffer and plate is described by the following equations:

$$m\ddot{y} = -P(t), \quad \rho h\pi r_0^2\ddot{w} = 2\pi r_0 Q_r + P(t), \tag{9}$$

where $y = \alpha + w$ is the total displacement of the projectile (Fig. 1), $P(t) = E_1(\alpha - w)$ is the contact force, and E_1 is the spring stiffness. Substituting the expressions for y and $P(t)$ into Eqs. (9) and taking into account that the plane tangent to the median surface at the boundary points of the contact zone is horizontal [3, 4], we obtain a system of equations describing interactions between the projectile, the buffer, and the plate. In order to solve this system, the functions entering into the equations can be presented in the form of power series with respect to time t. Substituting expressions (7) and (8), written for the boundaries of the contact region (i.e., at $r = r_0$), and the power series in time t for α into system (9) and equating coefficients, we obtain a system of equations for determining three constants ($j = 0, 1, 2$)

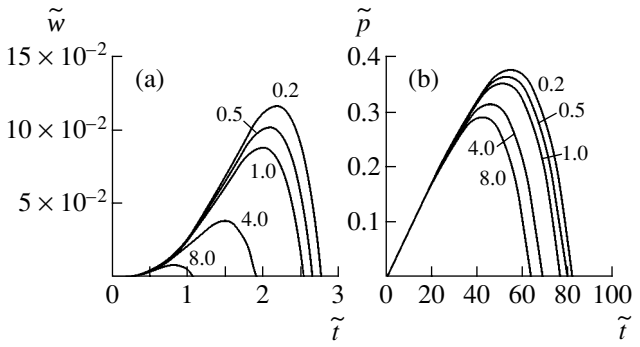

Fig. 2. Time variation of (a) the dynamic inflection w and (b) the contact force p calculated for various values of the E_θ/E_r ratio (indicated at the curves).

and α_i (i = 0, 1, 2, 3, 4). Once the integration constants are determined, it is possible to calculate the dynamic inflection and the contact force at any time t as the segments of power series with known coefficients.

In order to illustrate the results, we have studied a particular case and determined the dependence of the dynamic inflection w and the contact force p on the orthotropic properties of the plate. Figure 2 shows the time variation of w and p calculated for various values of the E_θ/E_r ratio (indicated at the curves). As can be seen from these data, a decrease in the E_θ/E_r ratio leads to an increase in the dynamic inflection and the contact force to certain values (for $E_\theta/E_r \ll 1$), while an increase in this ratio leads to a decrease in both dynamic inflection and the contact force. Thus, the lateral anisotropy of the plate significantly influences the dynamic characteristics of the impact in the system studied.

REFERENCES

1. Ya. S. Uflyand, Prikl. Mekh. **12**, 287 (1948).
2. R. D. Mindlin, Quarterly Appl. Math. **19**, 51 (1961).
3. Yu. A. Rossikhin and M. V. Shitikova, Acta Mech. **102**, 103 (1994).
4. Yu. A. Rossikhin, M. V. Shitikova, and A. A. Loktev, Izv. Vyssh. Uchebn. Zaved., Stroit., No. 11, 16 (2004).
5. S. A. Ambartsumyan, *Theory of Anisotropic Plates: Strength, Stability and Vibrations* (Nauka, Moscow, 1987; Hemisphere, New York, 1991).

Translated by P. Pozdeev

Technical Physics Letters, Vol. 31, No. 9, 2005, pp. 770–771. Translated from Pis'ma v Zhurnal Tekhnicheskoĭ Fiziki, Vol. 31, No. 18, 2005, pp. 10–14.

Grain-Boundary Internal Friction in Alloys with Dispersed Inclusions

V. G. Kul'kov

Moscow Power Engineering University (Volzhskiĭ Branch), Volzhskiĭ, Volgograd oblast, Russia

e-mail: kulkov@vlz.ru

Received April 20, 2005

Abstract—The role of dispersed particles in the grain-boundary slip in alloys with such second phase inclusions is considered. An equation for the grain-boundary slip velocity, formulated with allowance for an external variable load and the internal reverse stress produced by the dispersed particles, is solved and the contribution of the latter factor to the internal friction is determined. The frequency spectrum of internal friction in this system has the shape of a broad peak. © *2005 Pleiades Publishing, Inc.*

Dispersed solid particles of a second phase occurring at the grain boundaries of a two-phase alloy act as effective stoppers for the grain-boundary slip. The relative local shift of grains has an inhomogeneous distribution and reaches a maximum in the regions of grain boundaries most distant from the second phase inclusions. Below we will analyze the dissipation of energy in the course of slip at the incommensurate grain boundaries containing hard inclusions. In contrast to the case of special boundaries, where the principal mechanism of such deformation is the motion of grain-boundary dislocations, the velocity of slip at the boundaries under consideration is controlled by the rearrangement of local atomic configurations [1].

Let us consider spherical particles of radius R_0 uniformly distributed over the grain boundary, which intersects with the spheres along their equators. We assume that the mutual displacement of grains inside the inclusions is absent. A constant shear stress σ applied to the boundary results in a macroscopic mutual shift u of the grains along the boundary. The balance of forces yields an effective stress at the spheres (acting as stoppers): $\sigma_c = \sigma(\pi N R_0^2)^{-1}$, where N is the number of inclusions per unit area of the grain boundary. For this mode of loading, the inclusions arranged symmetrically with respect to the grains and stresses remain at rest in the laboratory frame, whereas the grains are displaced by $u/2$ in the opposite directions.

In order to determine the magnitude of the mutual shift, let us first solve an auxiliary problem. Considering the grain as a half-space bounded by the boundary plane and passing to the system of coordinates fixed on this grain, let us determine the displacements of points inside the circular section under the action of a force $\pi R_0^2 \sigma_c$ uniformly distributed over the section area. Placing the origin of coordinates at the center of the undisplaced circle and orienting the coordinate axes in the xy boundary plane so that the force will be directed along the x axis, we reduce the problem to the description of the equilibrium of an elastic medium bounded by a plane [2] under the action of a surface force.

If the radius of inclusions is small compared to the distance between them, $R_0^2 \ll N^{-1}$, the displacements of various points in the circles can be assumed to be the same and to be equal to the displacement of the center. Using an expression for the G_{11} component of Green's tensor [2], we obtain

$$\frac{u}{2} = \int_{S_0} G_{11}(x, y)\sigma_c dS, \tag{1}$$

where

$$G_{11}(x, y) = \frac{1+\nu}{\pi E}\left(\frac{(1-\nu)}{r} + \frac{\nu x^2}{r^3}\right),$$

E is Young's modulus, ν is the Poisson ratio, $r^2 = x^2 + y^2$, and the integration is performed over the circle area. Taking the integral in (1), we obtain an expression

$$\sigma = \frac{\pi N E R_0}{2(1+\nu)(2-\nu)}u, \tag{2}$$

which relates the shear stress to the mutual shift of grains in the initial (laboratory) frame.

The velocity of the grain-boundary slip strongly depends on the structure of this boundary and is determined by the diffusion mobility of vacancies at the boundary [3] or by the mobility of atoms of the dissolved (dispersed) component. In the latter case, the impurity atoms occurring at the boundary sequentially act as stoppers in the course of slip. As a result, the energy of such atoms increases and the further local

1063-7850/05/3109-0770$26.00

shift is possible only upon disappearance of the stoppers as a result of their diffusion along the boundary to the new energetically favorable positions. The slip is controlled by the rates of appearance and disappearance of stoppers.

Under these conditions, the velocity of slip at an incommensurate boundary under the action of the shear stress σ_t is given by the expression [4]

$$v = \frac{2\pi DkT}{\lambda^2 S_1^2 n}\sigma_t, \quad (3)$$

where D is the grain-boundary diffusion coefficient for the impurity, S_1 is the average area of a cell in the potential relief of the grain boundary, λ is the force constant describing the interaction of atoms on both sides of the boundary, and n is the number density of atoms at the boundary. The coefficient at σ_t has a meaning of the system mobility in the grain-boundary slip. An analogous relation is valid for the slip velocity and stress averaged over the grain boundary with inclusions. Defining v as du/dt and considering σ_t as a superposition of the external variable stress $\sigma(t) = \sigma_0\exp(i\omega t)$ and the reverse stress (2) produced by the inclusion, we can write expression (3) as

$$\frac{du}{dt} = \frac{2\pi DkT}{\lambda^2 S_1^2 n}\left(\sigma_0\exp(i\omega t) - \frac{\pi NER_0}{2(1+\nu)(2-\nu)}u\right). \quad (4)$$

The solution of this equation for a stationary regime of oscillations is as follows:

$$u = \frac{2(1+\nu)(3-2\nu)\sigma_0}{\pi NER_0(1+\omega^2\tau^2)^{1/2}}\exp(i(\omega t-\varphi)),$$
$$\tau = \frac{\lambda^2 S_1^2 n(1+\nu)(2-\nu)}{\pi^2 DkTER_0 N}, \quad \tan\varphi = \omega\tau. \quad (5)$$

The internal friction related to the inhomogeneous slip is defined as [5]

$$Q^{-1} = \frac{\Delta W}{2\pi W}, \quad (6)$$

where $\Delta W = S\int_0^{2\pi/\omega}\mathrm{Re}\,(\sigma(t))\mathrm{Re}(du/dt)dt$ is the energy loss per cycle over a grain boundary area S, $W = \sigma_0^2 V/2E$ is the maximum elastic energy of oscillations, and V is the grain volume. Substituting these expressions into formula (6), taking into account Eqs. (5), and using the relation $S/V = \gamma/d$ (where d is the grain size and γ is a geometric factor reflecting the grain shape, the fraction of grain boundary belonging to one grain, and the orientation of grains relative to the external stress direction), we eventually obtain

$$Q^{-1} = \frac{2(1+\nu)(2-\nu)\gamma}{\pi NR_0 d}\frac{\omega\tau}{1+\omega^2\tau^2}. \quad (7)$$

According to Eq. (7), the frequency dependence of the internal friction has the form of a Debye peak with an effective relaxation time $\tau = \tau_0\exp(-Q/kT)$ and the grain-boundary diffusion activation energy Q. The value of the pre-exponential factor can be evaluated using the following relations: $\lambda \sim Ea$; $Ea^3/kT_m \sim 50$ [6], $n/N \sim 10^2$; $a/R_0 \sim 10^3$, and $S_1 \sim a^2$, where a is the crystal lattice period. The characteristic temperature in the experiments with grain-boundary internal friction amounts to approximately half of the melting temperature T_m, which yields an estimate of $\tau_0 \sim 10^{-12}$ s. This value is characteristic of the grain-boundary slip on incommensurate boundaries, where the elementary slip events are local rearrangements of two-well atomic energy configurations at the boundary [1, 7]. In a real system, the peak width is greater than the Debye value as a result of the unavoidable spread of the size of inclusions and their inhomogeneous distribution over the grain boundary. As can be seen from relations (5) and (7), an increase in the concentration N of inclusions at the boundary leads to a decrease in the peak height. This is evidence that such inclusions play the role of stoppers in the grain-boundary slip [8, 9]. In addition, an increase in N is accompanied by a decrease in the relaxation time τ, which is also in agreement with experiment [10].

REFERENCES

1. B. M. Darinskiĭ and V. G. Kul'kov, Poverkhnost, No. 5, 153 (1993).
2. L. D. Landau and E. M. Lifshitz, *Course of Theoretical Physics*, Vol. 7: *Theory of Elasticity* (Nauka, Moscow, 1965; Pergamon, New York, 1986).
3. V. G. Kul'kov, Kondens. Sredy Mezhfaz. Gran. **3** (4), 373 (2001).
4. B. M. Darinskiĭ and V. G. Kul'kov, Pis'ma Zh. Tekh. Fiz. **18** (2), 65 (1992) [Sov. Tech. Phys. Lett. **18**, 50 (1992)].
5. A. S. Nowick and B. S. Berry, *Anelastic Relaxation in Crystalline Solids* (Academic, New York, 1972).
6. V. N. Chuvil'deev, *Nonequilibrium Grain Boundaries in Metals: Theory and Applications* (Fizmatlit, Moscow, 2004) [in Russian].
7. V. V. Gorbunov, B. M. Darinskiĭ, S. V. Mushtenko, *et al.*, Izv. Ross. Akad. Nauk, Ser. Fiz. **60** (9), 137 (1996).
8. M. S. Blanter, I. S. Golovin, S. A. Golovin, A. A. Il'in, and V. I. Sarrak, *Mechanical Spectroscopy of Metallic Materials* (MIA, Moscow, 1994) [in Russian].
9. B. H. Luo, Z. H. Bai, and Y. Q. Hie, Mater. Sci. Eng. A **370**, 172 (2004).
10. N. Shigenaka, R. Monzen, and T. Mori, Acta Metall. **31**, 2087 (1983).

Translated by P. Pozdeev

Technical Physics Letters, Vol. 31, No. 9, 2005, pp. 772–774. Translated from Pis'ma v Zhurnal Tekhnicheskoĭ Fiziki, Vol. 31, No. 18, 2005, pp. 15–21.

A Heterocontact in the Semiconductor–Mumie System

S. I. Drapak[a,*], V. V. Netyaga[a], Yu. I. Prilutskiĭ[b], M. O. Vorobets[b], and Z. D. Kovalyuk[a]

[a] *Frantsevich Institute for Problems of Materials Science (Chernivtsy Department), National Academy of Sciences of Ukraine, Chernivtsy, Ukraine*

[b] *Kiev National University, Kiev, Ukraine*

** e-mail: chimsp@unicom.cv.ua*

Received April 29, 2005

Abstract—The list of materials that can be used in photosensitive structures has been expanded to include mumie—an organic compound of a biological nature. The current–voltage, capacitance–voltage, and photoelectrical characteristics of *n*-InSe–mumie heterostructures have been studied. The spectrum of the relative quantum efficiency of these heterostructures exhibits a correlation with the optical absorption spectrum of mumie films deposited from ethanol solutions. *© 2005 Pleiades Publishing, Inc.*

The development of new types of heterojunctions between inorganic semiconductors and other substances of various origins is among the promising directions in modern optoelectronics [1]. Recently, it was demonstrated that photosensitive hybrid structures can be created using direct contacts between traditional inorganic semiconductors and some substances of biological nature [2–5]. This Letter presents the results of the first observation of a photovoltaic effect in the contact of a semiconductor (InSe) with the natural biologically active substance of mumie.

Mumie, which has been known from ancient times for its curative properties [6], is a complex chemical compound found in the form of films, crusts, and outgrowths of a resinous mass with sand and rubble inclusions in the cracks of rocks and in various voids and cavities. Being purified and extracted, mumie appears as a homogeneous elastic mass containing both organic and inorganic components, including about 30 trace elements, 10 metal oxides, and a complex of organic and mineral compounds.

We have studied the electrical and photoelectrical properties of heterostructures prepared by depositing mumie films from ethanol solutions onto the surface of substrates—cleaved single crystal plates of the layered semiconductor InSe—using a method described previously [7]. The initial material was a purified mumie (Technical Specification TU-9358-003-22588590-2001) produced by Biovit Company (Bishkek, Kyrgyzstan) in the form of a food additive. The samples were prepared using *n*-InSe substrates with a charge carrier density of $n = 2 \times 10^{15}$ cm^{-3} and a major carrier mobility of $\mu_\perp \approx 700$–800 cm^2/(V s) in the direction perpendicular to the symmetry axis (both parameters determined at $T = 300$ K). The thicknesses of mumie films (with a density of about 80 mg/cm^3) on the semiconductor surface varied from 15 to 30 μm, and their specific conductivities were on the order of 10^{-7}–10^{-8} Ω^{-1} cm^{-1}. The electric contacts on the semiconductor and mumie surfaces were formed by depositing indium and silver films, respectively.

Measurements of the stationary current–voltage (*I*–*V*) characteristics of the samples prepared as described above showed that the *n*-InSe–mumie heterojunctions exhibit a clearly pronounced rectification effect: at a bias voltage of $|V| = 2.5$–3 V, the forward current exceeded the reverse current by a factor of not less than 10^2. The forward direction always corresponded to the bias voltage applied with minus on *n*-InSe.

Figure 1a (curves *1* and *2*) shows the typical *I*–*V* characteristic of the *n*-InSe–mumie heterostructure. The initial portions of forward branches of these *I*–*V* characteristics at $V \le 2.2$–2.5 V (Fig. 1, curve *1*) with allowance for a serial differential resistance at $T = 287$ K can be subdivided into three regions. In the region of small bias voltages ($V \le 0.2$ V), the forward current varies as $I = I_{01}\exp(eV/nkT)$ with a diode coefficient of $n = 2$. For $0.2\ \text{V} \le V \le 1.2$–$1.4$ V, the current obeys the law $I = I_{02}\exp(\alpha V + \beta T)$, where the coefficients α and β are independent of the voltage and temperature. In the interval 1.2–$1.4\ \text{V} \le V \le 2.2$–$2.5$ V, the current varies as $I = I_{03}\exp(eV/nkT)$ with $n \cong 1$. Such a behavior of the current as a function of the forward bias voltage is characteristic of the heterojunctions based on inorganic semiconductors, which correspond to the Anderson model. In the general case, the forward current in such structures is a sum of the recombination current (I_{gr}) in the space charge region, the tunneling current (I_t), and the over-barrier current (I_d) [8]. However, in our experiments, a change of the temperature in the interval $T = 220$–303 K was accompanied by a parallel shift of the $I = f(V)$ curve, whereby I_0 in all three

regions for the forward bias voltages up to $V \approx 2.2–2.5$ V varied according to the law $I_0 \sim \exp(E_a/kT)$ and the activation energy varied in various samples within $E_a = 0.32–0.34$ eV.

On the other hand, the initial regions of the forward *I–V* curves of the *n*-InSe–mumie structures studied are similar to the $I = f(E)$ curves (where E is the electric field strength) for gases [9]. According to [10], organic substances possessing semiconductor properties resemble molecular gases rather than solids. This circumstance suggests that the initial regions of the forward *I–V* curves in our case reflect the current transfer via the space charge region displaced completely into the organic layer.

In the range of forward bias voltages $V > 4$ V (Fig. 1, curve *3*), the current in *n*-InSe–mumie structures is described by a linear function of the voltage:

$$I = (V - V_0)/R_0, \quad (1)$$

where the cutoff voltage is $V_0 \cong 2.5$ V and the residual resistance at $T = 287$ K is $R_0 \sim 10^4\ \Omega$.

At small reverse bias voltages ($|V| < 0.3–0.5$ V), the behavior of *I–V* curves of the structures studied significantly varied from one sample to another, which suggests that a dominating role in this region is played by leakage currents. In the region of higher values of the reverse bias voltage, the *I–V* curves can be described by the relation

$$I \sim (\varphi_0 - eV)^{1/2}, \quad (2)$$

which is characteristic of the generation–recombination processes in the space charge region [8]. An increase in the temperature led to expansion of the range of voltages in which relation (2) was obeyed. For example, at $T = 243$ K, the *I–V* curves of the *n*-InSe–mumie structures studied were satisfactorily described by Eq. (2) in the interval of reverse bias voltages $|V| \approx 0.5–3$ V, while at $T = 303$ K this interval extended from 0.5 to 12 V. At large reverse bias voltages, the current obeyed a power law ($I \sim V^2$), which is characteristic of both a tunneling regime and the regime of current limited by the space charge [11].

The capacitance–voltage (*C–V*) characteristics of the *n*-InSe–mumie system were measured in a frequency range of $f = 10–30$ kHz and were found to vary with the frequency. This is characteristic of the structures based on inorganic semiconductors with large residual resistances [12]. In the interval of reverse bias voltages from 0 to 3 V, the capacitance–voltage curves were close to linear when plotted in the C^{-2} versus V coordinates. However, the values of the barrier potential determined according to [12] by measuring the cutoff voltages V_b at various frequencies, plotting $V_b(\omega)$ versus ω^2, and extrapolating this plot to $\omega = 0$ gave a rather ambiguous pattern. At the same time, the cutoff

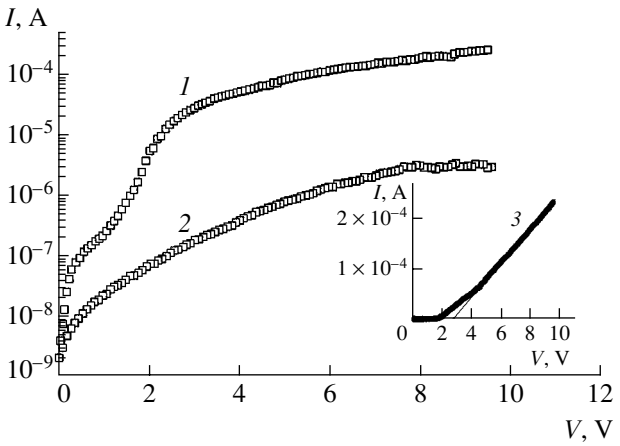

Fig. 1. The typical stationary current–voltage characteristic of *n*-InSe–mumie heterostructures ($T = 287$ K): (*1*, *3*) forward branch; (*2*) reverse branch. The area of the mumie film of the semiconductor substrate was $S_M = 0.45$ cm^2; the area of a silver contact on the organic film was $S_{Ag} = 0.08$ cm^2.

voltages determined from *C–V* curves measured at $\omega = 10–30$ kHz and reconstructed as C^{-3} versus V were always equal to the same value, $V_b = 2.63$ V, which was in good agreement with the V_0 value determined from the *I–V* curves. Since the mumie solutions can rather be considered as suspensions or emulsions [13], it is quite probable that the linear behavior of $C^{-3} = f(V)$, which is typical of smooth *p–n* junctions, reflects a specific organization taking place in organic films on the semiconductor surface in the course of solvent evaporation. An increase in the probing signal frequency up to $\omega = 0.5–1$ MHz led to an increase in the capacitance of the *n*-InSe–mumie structure rather than to a decrease (observed when the frequency was varied in the 10–30 kHz interval). This behavior is indicative of a dispersion of the dielectric properties of mumie films in this frequency range.

Under illumination with natural light, the *n*-InSe–mumie structures studied exhibited a photovoltaic effect, whereby the semiconductor substrate acquired a negative charge, in agreement with the forward current direction according to the *I–V* characteristics. The photo emf direction depended neither on the wavelength nor on the position of the probing light spot on the sample surface. The magnitude of the photoresponse was greater when the heterostructures were illuminated from the side of the mumie film.

Figure 2 (curve *1*) shows the typical spectrum of the relative quantum efficiency $\eta(h\nu)$ of photoconversion, which was determined as the ratio of the photocurrent to the number of photons incident onto a *n*-InSe–mumie structure. The shape of this curve is typical of semiconductor-based heterojunctions. The slope of the long-wavelength exponential photosensitivity edge, $s = \delta(\ln\eta)/\delta(h\nu) \approx 80$ eV^{-1}, corresponds to the direct optical transitions in the semiconductor, while the energy

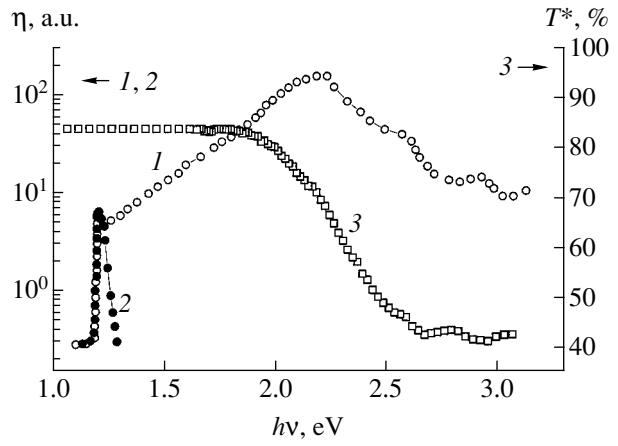

Fig. 2. The spectra of the relative quantum efficiency η(*h*ν) of photoconversion in the *n*-InSe–mumie heterostructure illuminated from the side of (*1*) organic layer and (*2*) semiconductor. Curve *3* is the spectrum of the optical transmission *T** of a mumie film with a thickness of $d = 70$ μm. $T = 287$ K.

position of the bending point ($h\nu = 1.2$ eV) agrees with the bandgap width in InSe. In the region of the fundamental absorption edge, the η spectrum exhibits a narrow peak, which is typical of the photoconductivity in layered $A^{III}B^{VI}$ semiconductor compounds and is usually attributed to excitonic effects. The growth of the photosensitivity observed on increasing the photon energy up to $h\nu \approx 2.3$ eV is related to an increase in the optical absorption coefficient of InSe in this spectral interval, which improves the collection and separation of photogenerated charge carriers at the heterocontact.

The decrease in the photosensitivity observed at $h\nu > 2.3$ eV and small local peaks at $h\nu \approx 2.6$, 2.9, and 3.2 eV qualitatively agree with the spectrum of the optical absorption coefficient of the organic compound (Fig. 2, curve *3*). For this reason, the short-wavelength decrease in η(*h*ν) can be related to the optical absorption in the broad-bandgap component through which the radiation is transmitted to the active region of the heterostructure. When the structure was illuminated from the side of the semiconductor substrate, the efficiency of photoconversion was significantly decreased and the photoresponse exhibited a high selectivity with a peak near the bandgap width (~1.2 eV) of InSe (Fig. 2, curve *2*). This behavior is explained (i) by the sharp growth of the optical absorption in the semiconductor plate upon the onset of direct interband transitions and (ii) by the fact that the distance from the layer of effective carrier generation to the active region exceeds the diffusion length of photoholes in InSe.

Thus, the contact of a semiconductor with mumie, as well as with some other substances of a biological nature [2–5], exhibits a photovoltaic effect, which can be used in the development of photosensors operating in a broad spectral range.

REFERENCES

1. Zh. I. Alferov, Fiz. Tekh. Poluprovodn. (St. Petersburg) **32**, 3 (1998) [Semiconductors **32**, 1 (1998)].
2. V. Yu. Rud', Yu. V. Rud', and V. Kh. Shpunt, Fiz. Tekh. Poluprovodn. (St. Petersburg) **31**, 129 (1997) [Semiconductors **31**, 97 (1997)].
3. V. Yu. Rud', Yu. V. Rud', and V. Kh. Shpunt, Zh. Tekh. Fiz. **70** (2), 114 (2000) [Tech. Phys. **45**, 255 (2000)].
4. S. I. Drapak and Z. D. Kovalyuk, Pis'ma Zh. Tekh. Fiz. **30** (6), 73 (2004) [Tech. Phys. Lett. **30**, 250 (2004)].
5. S. I. Drapak, V. B. Orletskiĭ, V. D. Fotii, and Z. D. Kovalyuk, Prikl. Fiz. **11** (2), 73 (2004).
6. Abu Ali ibn Sina (Avicenna), *Canons of Medical Science* (Fan, Tashkent, 1982), Vol. 2 [in Russian].
7. S. I. Drapak, V. B. Orletskiĭ, Z. D. Kovalyuk, and V. V. Netyaga, Pis'ma Zh. Tekh. Fiz. **29** (20), 69 (2003) [Tech. Phys. Lett. **29**, 867 (2003)].
8. B. L. Sharma and R. K. Purohit, *Semiconductor Heterojunctions* (Pergamon, Oxford, 1974).
9. N. P. Bogoroditskiĭ, Yu. M. Volokobinskiĭ, A. A. Vorob'ev, and B. M. Tareev, *Theory of Insulators* (Énergiya, Moscow, 1965) [in Russian].
10. E. A. Silinsh and L. F. Taure, *Organic Semiconductors* (Znanie, Moscow, 1980) [in Russian].
11. S. Sze, *Physics of Semiconductor Devices* (Wiley, New York, 1981).
12. T. V. Blank, Yu. A. Gol'dberg, E. V. Kalinina, *et al.*, Fiz. Tekh. Poluprovodn. (St. Petersburg) **35**, 550 (2001) [Semiconductors **35**, 529 (2001)].
13. T. L. Kiseleva, L. N. Frolova, L. A. Baratova, and S. I. Galina, Med.-Farm. Vestnik, No. 6, 38 (1996).

Translated by P. Pozdeev

Technical Physics Letters, Vol. 31, No. 9, 2005, pp. 775–778. Translated from Pis'ma v Zhurnal Tekhnicheskoĭ Fiziki, Vol. 31, No. 18, 2005, pp. 22–29.

High-Power Microwave Pulses Generated by a Resonance Relativistic Backward Wave Oscillator with a Power Supply System Based on Explosive Magnetocumulative Generators

K. V. Gorbachev, S. D. Korovin, G. A. Mesyats, E. V. Nesterov, S. D. Polevin*, V. A. Stroganov, M. Yu. Sukhov, E. V. Chernykh, and V. E. Fortov

Institute of High-Current Electronics, Siberian Division, Russian Academy of Sciences, Tomsk, 634055 Russia

Institute for High Energy Densities, Associated Institute for High Temperatures, Russian Academy of Sciences, Moscow, Russia

Lebedev Institute of Physics, Russian Academy of Sciences, Moscow, 117924 Russia

** e-mail: polevin@hcei.tsc.ru*

Received April 27, 2005

Abstract—High-power microwave radiation has been generated using a relativistic backward wave oscillator (BWO) powered by a high voltage source comprising an inductive energy storage and an electric-explosion current switch. The high voltage source and the BWO magnetic system are energy pumped by explosive magnetocumulative generators. In experiments, the proposed setup generated 30-ns single-mode radiation pulses with a carrier frequency of 3.6 GHz at an output power of 0.75 GW. *© 2005 Pleiades Publishing, Inc.*

In recent years, considerable progress has been achieved in the high-current electronics of high-power radiation sources. In particular, pulsed electromagnetic radiation has been generated at the gigawatt power level in the centimeter wavelength range [1] for a broad spectrum of applications, including ultra-long-range radar systems, plasma physics and technology, and action upon various natural and technical objects. Such high-power microwave generators are based on high-current direct drive electron accelerators, which are capable of forming intense electron beams with a current density of 10^3–10^6 A/cm^2 and a power of 10^8–10^{13} W in the explosive emission regime. The accelerators and the magnetic systems of electron beam transport are traditionally powered by high-voltage capacitive energy storages, in which the energy density does not exceed 10^{-1} J/cm^3. Such power supply systems are sophisticated, cumbersome, and expensive.

Among accessible pulsed energy sources, a record high specific energy density (~10^4 J/cm^3) is provided by condensed explosives. The ultimate potential in the production of current pulses and magnetic energy pulses is offered by the existing explosive magnetocumulative generators (EMGs), which employ the fast compression of magnetic flux by a conducting shell accelerated by the products of explosion [3]. The generation of current pulses in EMGs is based on the direct conversion of chemical energy into the magnetic field energy. However, the use of such pulses is complicated by stringent requirements to the matching of characteristics of EMGs and microwave generators. Indeed, the characteristic time of current pulse formation in EMGs, while being much greater than the characteristic time of processes in high-current accelerators, is still insufficient for obtaining quasi-stationary magnetic fields transporting the beam in the slow-wave structures (SWS) used in most microwave generators. However, previous investigations in which vircators (relativistic generators with virtual cathodes) [4] and Cherenkov generators [5] were powered by EMGs showed the technical possibility of and good prospects for using such energy sources.

This paper presents the results of experiments aimed at further expanding the power scale of microwave generators using EMGs as primary energy sources.

Resonance relativistic backward wave oscillator (BWO). In this study, high-power microwave pulses were obtained using a resonance relativistic BWO with a high generation efficiency achieved through the optimization of the longitudinal distribution of a high-frequency field (improved due to reflection of the working TM_{01} mode from the ends of an electrodynamic system) and the interaction of electron beam with both for-

1063-7850/05/3109-0775$26.00

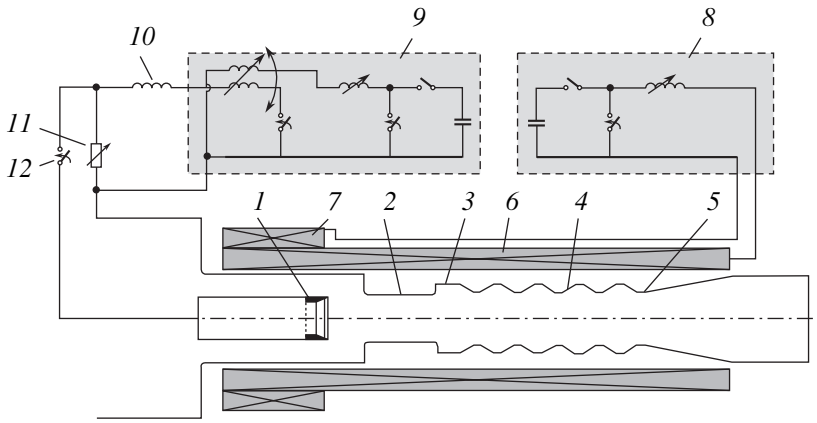

Fig. 1. Schematic diagram of a relativistic BWO and the experimental setup: (*1*) explosive-emission cathode; (*2*) below-cutoff narrowing; (*3*) adjustment insert; (*4*) corrugated SWS; (*5*) resonance output reflector; (*6*) main solenoid; (*7*) correcting coil; (*8*) EMG feeding solenoid with a system of the initial magnetic flux formation; (*9*) two-stage EMG with a system of the initial magnetic flux formation; (*10*) inductive energy storage; (*11*) electric-explosion current switch; (*12*) discharger.

ward and backward waves [6]. An important advantage of the proposed resonance system over the usual relativistic BWO is the shorter length of the interaction space (about three wavelengths), which provided for a decrease in the energy required for the creation of a magnetic field.

Figure 1 shows a schematic diagram of the BWO studied. In this configuration, an electron beam is formed in a coaxial vacuum diode with a cylindrical exposive-emission graphite cathode *1* (with a diameter of 50 mm) and injected into the electrodynamic system via a below-cutoff narrowing *2* (ensuring the reflection of a backward electromagnetic wave). The longitudinal distribution of a high-frequency field is improved and the optimum interaction of the electron beam with the (–1)st spatial harmonic of the backward wave and the fundamental harmonic of the forward wave is provided by the partial reflection of the working TM_{01} mode from the collector end *5* of the electrodynamic system. Using this reflection, it is possible to control the quality of the electrodynamic system. A smooth cylindrical waveguide section *3* situated between the below-cutoff narrowing *2* and the SWS *4* was used for the adjustment of the optimum phase shift between the fundamental harmonic of the forward electromagnetic wave and the (–1)st harmonic of the backward wave. The ratio of the amplitudes of these harmonics was determined by the corrugation height in the SWS.

The BWO geometry was optimized using the numerical PIC-code KARAT [7]. The optimum geometry corresponded to the following parameters: SWS corrugation period, 0.55λ; SWS corrugation height, 0.12λ; SWS median radius, 0.42λ; SWS length, 2.5λ; electrodynamic system quality, 100; electron beam radius, 0.3λ (where λ is the radiation wavelength). The magnetic transport was provided at an induction of 1.5 T. The results of numerical simulations showed that the generation power efficiency (calculated as a ratio of the output radiation peak power to the maximum power of a beam injected into the electrodynamic system) of the BWO with the optimum geometry was about 30% and exhibited insignificant variations in a broad range of the electron beam power. The optimum impedance of the vacuum diode is about 100 Ω.

High-voltage pulse generation system. In our experiments (see the scheme in Fig. 1), the EMG current pulse was sharpened using an inductive energy storage *10* and electric-explosion current switch *11*. In order to ensure the effective operation of such a switch, it is necessary that the inductive energy storage would be energy pumped within a sufficiently short time. This was achieved by pumping the inductive energy storage from a two-stage spiral EMG operating on the principle of magnetic flux trapping [8]. The first stage provided for the main energy gain, and the second stage formed a current pulse with a short rise time in the inductive energy storage. The EMG had working spirals with a diameter of 80 mm, a liner with a diameter of 40 mm and a length of 400 mm, and an explosive charge of about 400 g. The effective operation time of the second stage (with respect to the integral current action) was 3.4 μs. The inductive energy storage was made of a coaxial cable with a length of 16 m and an inductance of about 4 μH. The electric-explosion current switch comprised several copper wires with a diameter of 0.1 mm and a length of 700 mm. The high voltage pulse was transmitted to the vacuum diode via a gas discharger tuned to operate at 300–400 kV. The main rules of selecting the optimum parameters for such systems of high voltage pulse generation are considered in [9].

Magnetic system of BWO. The main difficulty encountered in the formation of a homogeneous mag-

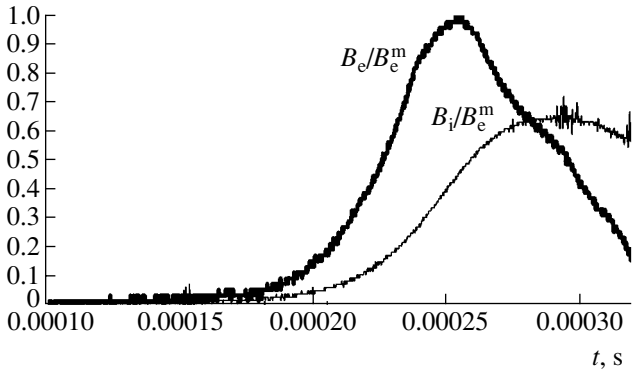

Fig. 2. Time variation of the magnetic induction measured at the SWS axis (B_i) and outside the SWS (B_e), normalized to the maximum value of magnetic induction at the external boundary of the SWS.

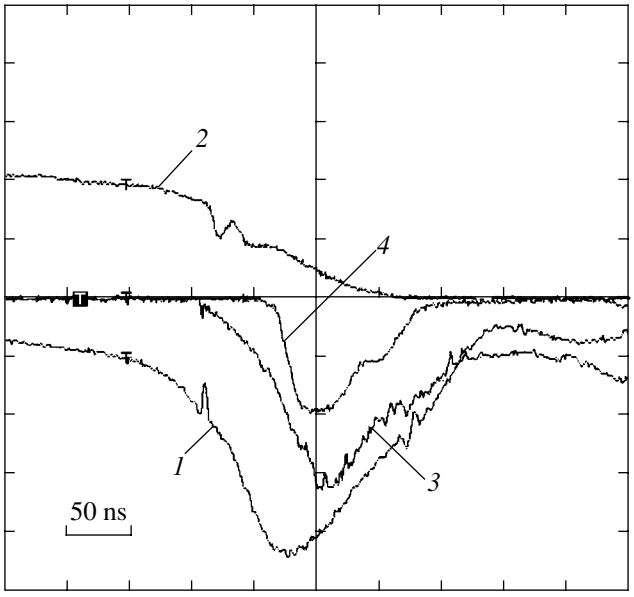

Fig. 3. Typical experimental oscillograms of the (*1*) voltage and (*2*) current in the switch, (*3*) electron beam current, and (*4*) microwave detector signal.

netic field inside the SWS is to ensure that the time of magnetic field penetration will be comparable with the characteristic time of EMG operation. In order to solve this self-consistent problem, we have performed the numerical simulation (using the results obtained previously [9]) and physical modeling of the system. Using the results of modeling, we determined the optimum parameters of the special EMG and solenoid for the system studied. By measuring the spatial distribution and temporal variation of the magnetic induction in the SWS, we have selected the optimum moment for the electron beam injection, which provided for the most homogeneous magnetic field in the SWS.

The source of current for the main solenoid and the correcting coil (with a total inductance of about 4 μH) was a specially developed high-inductance sectioned spiral EMG. The EMG comprised a spiral with a diameter of 90 mm (consisting of five sections with a total length of 400 mm), a liner with a diameter of 40 mm, and an explosive charge of 250 g. In order to increase the field penetration time, the detonation rate was reduced to 3.8 mm/μs. The EMG total operation time was 136 μs at a maximum current above 100 kA.

Figure 2 shows the oscillograms of the magnetic induction pulse measured at the SWS axis (B_i) and in the gap between SWS and solenoid (B_e). The magnetic field amplitude inside the SWS was $B_i^m \approx 1.5$ T. In order to improve the magnetic isolation of the electron beam in the magnetic system, it was possible to adjust the field using a single-turn correcting coil *7* (Fig. 1) connected in series with the main solenoid.

Experimental results. The resonance BWO was preliminarily adjusted for the optimum generation regime (by varying the impedance of the vacuum diode and the electron beam position on the collector) using capacitive energy storages. Then, the experiments were performed with the energy supply from EMGs. The operation of both EMGs was synchronized using an explosive delay line so that the electron beam would propagate in the most homogeneous magnetic field.

The microwave radiation parameters were measured either in the output tract, using a directional coupler and a calibrated detector, or at the BWO output using a wide-aperture calorimeter [10].

In the optimum operation regime, characterized by an inductive energy storage current of 35 kA (at the moment of current switching to the load), a cathode voltage of 750 kV, and a tubular electron beam current of 9 kA, the peak microwave power was 0.75 GW at a pulse width at half maximum (FWHM) of about 30 ns. Figure 3 shows the typical oscillograms of the voltage and current in the switch, the electron beam current, and the microwave detector signal. The generation frequency (3.6 GHz) and the directivity pattern corresponded to the TM_{01} mode of a round waveguide. In these experiments, the electron leakage current to anode was about 2 kA, and the power efficiency was about 14%.

REFERENCES

1. S. D. Korovin, V. V. Rostov, S. D. Polevin, *et al.*, IEEE Proc. (Special Issue on Pulsed Power: Technology and Applications) **92**, 1082 (2004).
2. G. A. Mesyats, *Generation of High-Power Nanosecond Pulses* (Sov. Radio, Moscow, 1974) [in Russian].
3. A. I. Pavlovskiĭ and R. Z. Lyudaev, in *Problems of Modern Experimental and Theoretical Physics*, Ed. by

A. P. Aleksandrov (Nauka, Leningrad, 1984), pp. 206–217 [in Russian].

4. E. I. Azarkevich, A. N. Didenko, *et al.*, Dokl. Akad. Nauk SSSR **319**, 353 (1991) [Sov. Phys. Dokl. **36**, 539 (1991)].
5. A. Ya. Brodskiĭ, V. A. Vdovin, A. S. Kravchenko, *et al.*, Dokl. Akad. Nauk SSSR **314**, 846 (1990) [Sov. Phys. Dokl. **35**, 876 (1990)].
6. S. A. Kitsanov *et al.*, in *Proceedings of the 14th International Conference on High Power Particle Beams, Albuquerque, 2002*, pp. 255–258.
7. V. P. Tarakanov, *User's Manual for Code KARAT* (Berkley, Springfield, 1992).
8. V. A. Davydov and V. K. Chernyshov, Zh. Prikl. Mekh. Tekh. Fiz., No. 6, 112 (1981).
9. *Explosive High-Power Current Pulse Generators*, Ed. by V. E. Fortov (Nauka, Moscow, 2002) [in Russian].
10. A. L. Lisichkin, E. V. Nesterov, and V. A. Stroganov, Prib. Tekh. Éksp., No. 1, 82 (1996).

Translated by P. Pozdeev

Technical Physics Letters, Vol. 31, No. 9, 2005, pp. 779–781. Translated from Pis'ma v Zhurnal Tekhnicheskoĭ Fiziki, Vol. 31, No. 18, 2005, pp. 30–36.

Structure and Magnetic Properties of Iron Based Nanoparticles with Oxide Shells

O. V. Tolochko[a,*], D. W. Lee[b], C. J. Choi[b], D. Kim[b], and M. Arif[a]

[a] *St. Petersburg State Polytechnical University, St. Petersburg, 195251 Russia*

[b] *Korea Institute of Machinery and Materials 66, Sangnam-Dong, Changwon, Kyungnam 641-010, South Korea*

** e-mail: oleg@ftim.spbstu.ru*

Received May 17, 2005

Abstract—Oxide-coated iron nanoparticles with average dimensions from 6 to 75 nm have been synthesized by chemical vapor condensation. The structure of particles and their size distribution have been determined. These data are used to interpret the results of measurements of the magnetic hysteresis characteristics. © *2005 Pleiades Publishing, Inc.*

In recent years, much attention has been devoted to the synthesis of ferromagnetic nanomaterials and to the investigation of their structure and properties. At present, the ferromagnetic particles most widely used in electronics and medicine are obtained using iron oxides representing magnetite (Fe_2O_4) and maghemite (γ-Fe_2O_3). However, metallic iron nanoparticles are obviously more promising as a base for magnetic recording media, magnetic fluids, magnetic-field-driven drug delivery systems, etc. [1–3].

Materials and experimental methods. Iron nanoparticles have been synthesized by the conventional method of chemical vapor condensation described in detail elsewhere [4]. An inert gas (Ar, He) was purged at a controlled rate through a thermostat containing liquid iron pentacarbonyl $Fe(CO)_5$ heated to the evaporation temperature. $Fe(CO)_5$ vapor was entrained by the gas flow and transferred to a reactor chamber, which was heated to a still higher temperature, making possible the pyrolysis of carbonyl with the formation of supersaturated iron vapor and carbon monoxide (CO). The condensation of iron vapor led to the growth of metal nanoparticles. The reactor temperature was controlled within 400–1100°C. Since the freshly synthesized iron particles are pyrophoric, the metal surface is subject to passivation (slow oxidation) even in an inert gas atmosphere containing about 10^{-4} vol % O_2, with the formation of an oxide shell.

The structure and phase composition of the synthesized particles were studied by X-ray diffraction (XRD), transmission electron microscopy (TEM), and Mössbauer spectroscopy. The XRD measurements were performed on a DRON 2.0 diffractometer using monochromatized Fe$K\alpha$ radiation. The TEM measurements were carried out on a JEOL JEM-2000FXII instrument operating at an accelerating voltage of 200 kV. The magnetic properties were studied in a field of up to 10 kOe using a vibrating-sample magnetometer.

The particle dimensions and their distribution were studied using the TEM data. First, the maximum average diameters were determined using TEM micrographs for not less than 200 particles and a histogram of their linear dimensions was constructed. Then, the mass corresponding to each particle size was calculated. The average particle size was determined upon description of the mass distribution in terms of the normal (Gaussian) or log-normal function.

Results and discussion. According to the TEM data (Fig. 1), the synthesized nanoparticles had a spherical shape and comprised a metal core and an oxide shell. The shell was formed as a result of the controlled oxidation (passivation) and consisted of magnetite (Fe_3O_4) epitaxially related to the crystal structure of the core [4]. The oxide shell thickness usually did not exceed 2–3 nm. The average particle size varied from 6 to 75 nm, depending on the process parameters. The particle size distribution obeyed the normal (usually, for particles smaller than 15 nm) or log-normal law, depending on the growth mechanism. The normal distribution corresponded to the growth via sequential attachment of iron atoms adsorbed from the vapor phase, whereas the log-normal distribution reflected the growth by coagulation of the previously formed particles [5].

Figure 1 also presents the electron microdiffraction patterns, which show that the phase composition of particles with various average dimensions is virtually the same. Indeed, in both cases, the diffraction patterns consist of smeared ring reflections due to the metal core and oxide shell, although the pattern for smaller particles (12 nm) exhibits more pronounced smearing and the pattern for greater particles (19 nm) shows evidence of the point reflections due to a bcc iron phase. The X-ray diffraction patterns of relatively large particles

1063-7850/05/3109-0779$26.00 © 2005 Pleiades Publishing, Inc.

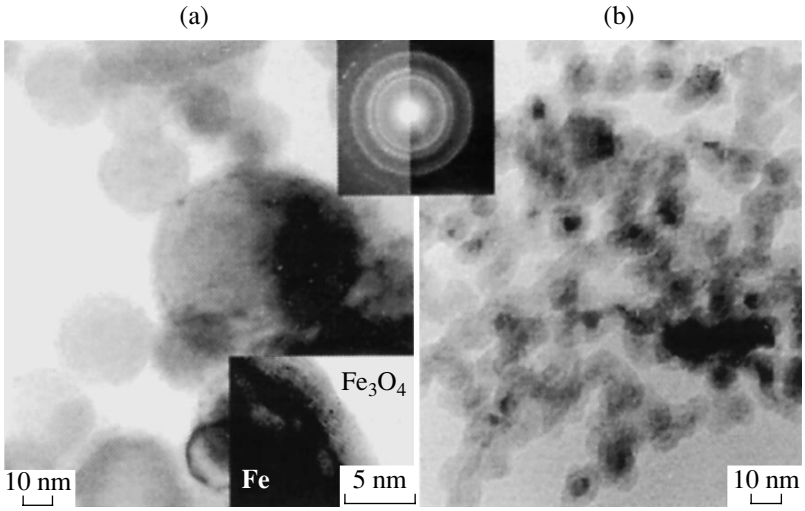

Fig. 1. TEM micrographs of iron based nanoparticles with an average size of (a) 19 and (b) 12 nm. The insets show the electron microdiffraction patterns (top) and the interphase boundary between the metal core and oxide shell (bottom).

revealed the presence of only the crystalline bcc iron phase. The diffractograms of particles smaller than 15 nm showed traces of an oxide phase, while the particles with linear dimensions below 8 nm appeared as X-ray-amorphous.

Figures 2 and 3 show the characteristic magnetic hysteresis loops and the curves of saturation magnetization M_s and coercive force H_c as functions of the average particle size. In Fig. 3, the particle size (abscissa axis) corresponds to the maximum of distribution with respect to the mass. For small particles, the positions of maxima in the mass and size distribution practically coincide. As the average particle size grows, the distribution becomes log-normal and the maximum shifts toward greater dimensions.

The maximum magnetization (up to 215 emu/g) was observed for the particles with an average size of 75 nm. This value is close to the theoretical magnetization of a compact pure bcc iron (~225 emu/g). As the average particle size decreases, the saturation induction also exhibits a decrease. However, this decrease well agrees with the values of induction calculated assuming that the specific saturation magnetization is a sum of the corresponding values for the metal core and the magnetite shell (~90 emu/g). In Fig. 3, the calculated values of magnetization fall within a cross-hatched region, reflecting uncertainty in determining the oxide shell thickness, which can vary within 2–3 nm.

Significant differences between the calculated and measured values are observed for nanoparticles with an average size (distribution maximum) of about 10–12 nm and below. In this region, an increasing contribution to the total magnetization is due to the growing fraction of superparamagnetic particles with dimensions below 6–7 nm (for which the measured magnetization does not exceed 10 emu/g). However, it should be noted that, in the range of probing magnetic fields employed, the saturation magnetization for superparamagnetic particles is not reached (Fig. 2a).

The observed dependence of the coercive force H_c on the particle size (Fig. 3) confirms the theoretical predictions: as the particle size decreases, the magnetization grows, exhibits a maximum, and then drops to zero [6]. It is commonly accepted that the maximum of the coercive force corresponds to the maximum proportion of monodomain particles. The experimentally determined maximum value of the coercive force (up to 1000 Oe) is observed for the particles with an average size of 20–25 nm (in which the metal core diameter is not less than 14–19 nm).

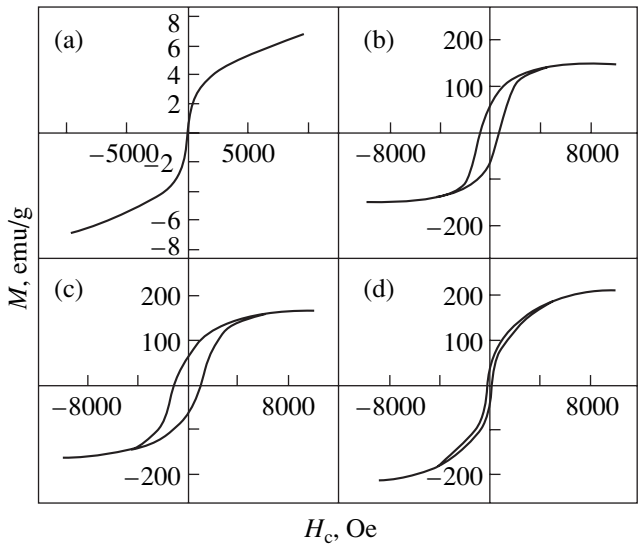

Fig. 2. The characteristic magnetic hysteresis loops of iron based nanoparticles with an average size of (a) 7, (b) 13, (c) 24, and (d) 75 nm.

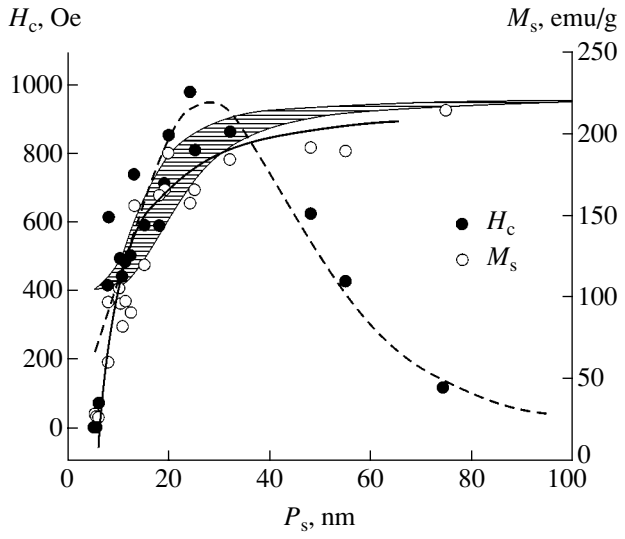

Fig. 3. Plots of the coercive force H_c and saturation magnetization versus average particle size. Cross-hatched region corresponds to the M_s values calculated for iron based particles comprising a metal core and 2- to 3-nm-thick magnetite shells assuming the additivity of their magnetic properties.

The domain size in magnetic materials is proportional to $A^{1/2}/M_s$, where A is the exchange energy parameter and M_s is the theoretical saturation magnetization [1]. In contrast to the case of ferrites and rare earth oxides, the exchange energy of metallic iron is small and the domain size does not exceed 10 nm [7]. However, the maximum value of the coercive force obtained in our experiments corresponds to a particle size significantly greater than 10 nm. Apparently, the maximum coercive force in this case is determined by interactions between the metal core and oxide shell or between the particles. It should also be noted that the coercive force reported for monodomain spherical magnetite particles is significantly (3–4 times) lower [6]. Further decrease in the average particle size is accompanied by a rapid drop of the coercive force practically to zero because of an increase in the proportion of superparamagnetic parcels. At an average particle size below 7 nm, the powder is completely superparamagnetic, which is confirmed by the data of Mössbauer spectroscopy. These particles contain more than 85% of nonmetallic phases (magnetite and β-FeOOH).

Conclusions. The results of our investigation of the magnetic hysteresis of iron based nanoparticles with the average size varying from 5 to 75 nm and with 2 to 3-nm-thick magnetite shells showed that the saturation magnetization monotonically increases with the particle size and virtually attains the level of the maximum (theoretical) magnetization for pure iron in the compact state. The coercive force exhibits a maximum of about 1000 Oe at an average particle size of 20–25 nm, which is significantly greater than the size of monodomain iron particles. This result probably indicates that the high-coercivity state is determined by the interaction between the metal core and the oxide shell. The particles with average dimensions below 7 nm are completely paramagnetic. The maximum size of particles according to the mass distribution in this case does not exceed 10 nm, so that the iron core size in such superparamagnetic particles is below 6 nm. The obtained nanoparticles can be used for the creation of permanent magnets, magnetic fluids, and magnetic media for data recording.

REFERENCES

1. R. H. Kodama, J. Magn. Magn. Mater. **200**, 359 (1999).
2. L. Hu and M. Chen, Mater. Chem. Phys. **43**, 212 (1996).
3. *Ultra-Fine Particles: Exploratory, Science and Technology*, Ed. by C. Hayashi, R. Ueda, and A. Tasaki (Noyes, Westwood, 1997).
4. C. J. Choi, O. Tolochko, and B. K. Kim, Mater. Lett. **56**, 289 (2002).
5. *Fine Particles: Synthesis, Characterization, and Mechanisms of Growth*, Ed. by T. Sugimoto (Marcel Dekker, New York, 1996).
6. G. F. Goya, T. S. Berquó, F. C. Fonseca, and M. P. Morales, J. Appl. Phys. **94**, 3520 (2003).
7. W. Gong, H. Zhao, Z. Li, and J. Chen, J. Appl. Phys. **69**, 5119 (1991).

Translated by P. Pozdeev

Technical Physics Letters, Vol. 31, No. 9, 2005, pp. 782–784. Translated from Pis'ma v Zhurnal Tekhnicheskoĭ Fiziki, Vol. 31, No. 18, 2005, pp. 37–43.

The Influence of Molecular Structure Modification on the Photoluminescence and Optical Absorption of Thin Copper Phthalocyanine Films in the Near-IR Range

A. G. Kazanskiĭ, E. I. Terukov*, A. V. Ziminov, O. B. Gusev, A. V. Fenukhin, A. G. Kolosko, I. N. Trapeznikova, Yu. A. Nikolaev, and Bey Modu

Moscow State University, Moscow, 119899 Russia

Ioffe Physicotechnical Institute, Russian Academy of Sciences, St. Petersburg, 194021 Russia

** e-mail: eug.terukov@mail.ioffe.ru*

Received April 20, 2005

Abstract—We have studied the luminescence and optical absorption of thin films of copper phthalocyanine (CuPc) with a modified molecular structure of the peripheral fragments. The coefficient of absorption in the near-IR and visible range (absorption by defects) and the photoluminescence spectra exhibit correlated changes depending on the modification of the CuPc structure. © *2005 Pleiades Publishing, Inc.*

In the past decade, the growing attention in the field of materials for electronics and optoelectronics has been devoted to organic semiconductors, in particular, conjugated polymers. This interest is related to the high technological capacity of these materials and their good prospects for use in the technology of thin-film solar cells and various data storage and display devices. Despite the successful application of thin-film organic semiconductors in optoelectronic devices whose operation is based on the interaction of such materials with radiation, the mechanisms of charge carrier generation, transport, and recombination in organic semiconductors are still incompletely clear. Information about the energy states of molecular semiconductors determining these processes can be obtained using optical methods, in particular, measurements of luminescence and absorption properties.

The properties of organic semiconductors–in particular, metal phthalocyanines–must strongly depend on the structure of their molecules. As is known, a change in the molecular structure as a result of the chemical modification of a peripheral part of the molecule leads to significant changes in the physicochemical properties of compounds. A discotic mesophase of copper phthalocyanine (CuPc) features strong intermolecular interactions and is capable of self-organization into columnar molecular ensembles. The data of X-ray diffraction show that substituted CuPc (in particular, with peripheral substituents possessing side chains) form a characteristic discotic mesophase with uniformly distributed alkyl chains situated between the molecular ensembles. A typical example is offered by the thermotropic mesomorphism of octa-alkoxy-substituted CuPc, in which the substituents are situated around the macrocyclic nucleus. The ester groups contribute to the microsegregation of molecular fragments in the columnar aggregates and to the stabilization of mesomorphous behavior of the discotic mesogenic phases. In this context, it is of interest to study correlated variations of the optical emission and absorption properties of CuPc in response to the modification of the molecular structure.

This paper presents the results of a comparative investigation of the photoluminescence spectra and the optical absorption in the near-IR and visible range for thin films of CuPc with various molecular structures.

CuPc films were grown by thermal deposition in vacuum with the aid of a Knudsen cell. The samples were prepared using the initial purified CuPc (sample 1), modified CuPc with a peripheral methylenephthalimide group (sample 2), and oxidized μ-peroxo-CuPc dimer (sample 3). The films were deposited onto Sitall (glass ceramic composite) or quartz glass substrates and had a thickness of $d \approx 65$ μm.

The photoluminescence (PL) spectra were measured using the excitation with an argon laser operating at 514.5 nm. The emission was analyzed by a grating monochromator and detected by a cooled germanium detector. All the PL measurements were performed at room temperature.

The spectral dependences of the optical absorption coefficients α of organic semiconductors are usually determined by measuring their transmission spectra [1]. However, this method cannot be used in the case of thin films with small α such that $\alpha d < 1$ (d is the film thickness). However, the significant photoconductivity of metal phthalocyanines allows the spectrum of α to be determined using photoelectric techniques, in particular, the constant photocurrent method [2], which has been successfully applied in the investigation of amor-

1063-7850/05/3109-0782$26.00

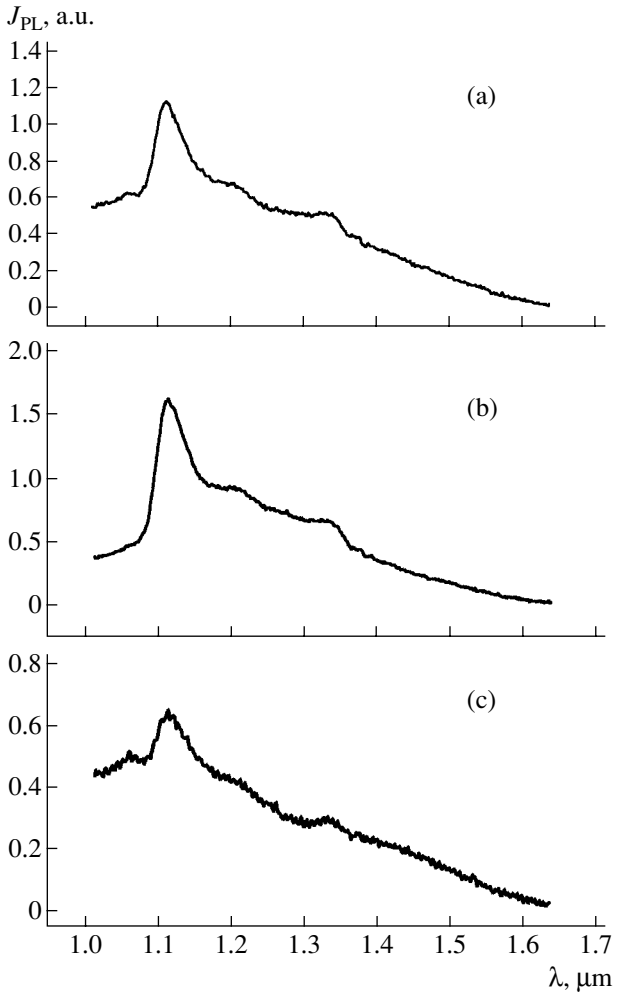

Fig. 1. The PL spectra of thin films of (a) purified CuPc (sample 1), (b) modified CuPc with a peripheral methylenephthalimide group (sample 2), and (c) oxidized μ-peroxo-CuPc dimer (sample 3).

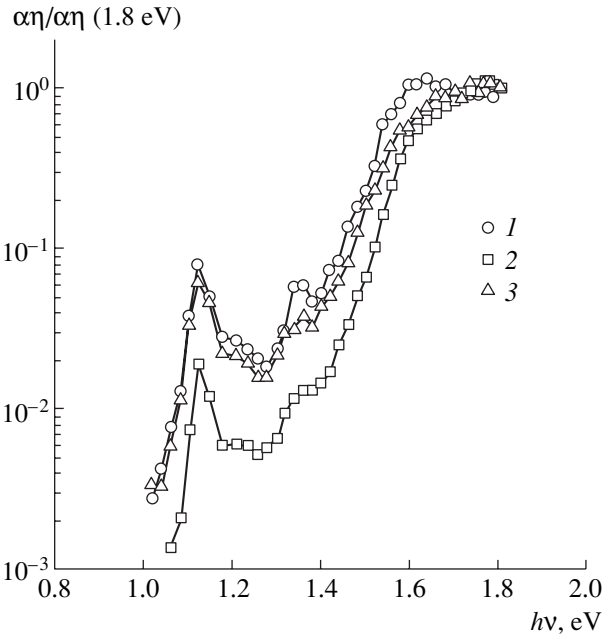

Fig. 2. The spectra of the αη product (normalized to maximum) obtained by the constant photocurrent method for thin films of (*1*) purified CuPc (sample 1), (*2*) modified CuPc with a peripheral methylenephthalimide group (sample 2), and (*3*) oxidized μ-peroxo-CuPc dimer (sample 3).

phous semiconductors. The photoconductivity measurements were performed using samples with 4-mm-long aluminum contacts deposited onto the CuPc film surface. The distance between the contacts was 0.5 mm. The photoconductivity was measured at room temperature and at an applied electric field of 200 V/cm. In order to eliminate the influence of atmosphere, the measurements were performed in vacuum, at a residual gas pressure of 10^{-3} Pa.

Figure 1 shows the typical spectra of PL in the near-IR spectral range. As can be seen, the emission intensity exhibits certain variations and shows a pronounced peak at a wavelength of $\lambda \approx 1.11$ μm (1.12 eV). The position of this peak is close to that of the phosphorescence maximum ($\lambda \approx 1.075$ μm) observed for a CuPc solution in 1-chloronaphthalene [3] and assigned to the transition from an excited triplet state (T_1) to the ground state (S_0). As can be seen from Fig. 1, the intensity of emission (in particular, of the main PL peak at 1.11 μm) depends on the molecular structure of the film: the maximum PL intensity was observed for sample 2.

The optical transmission spectrum of CuPc is characterized by an intense absorption at $h\nu = 1.77$ eV, which is related to the transition from the ground state (S_0) to an excited singlet state (S_1) [4]. Figure 2 shows the spectrum of the absorption coefficient measured using the constant photocurrent method. In organic semiconductors, the quantum efficiency η determining the probability of charge carrier generation upon the absorption of a photon depends on the quantum energy $h\nu$. Therefore, the photoelectric measurements in the constant photocurrent regime give the spectrum of the αη product [2]. Using the spectra presented in Fig. 2 in relative units, it is possible to compare the optical absorption of samples in the region of the absorption edge (at 1.5–1.5 eV). As can be seen, the curves of αη versus $h\nu$ in this region have an exponential shape. The energy characterizing the slope of the αη curve is ~53 meV for sample 2 and 65–68 meV for samples 1 and 3. The behavior observed in the region of 1.4–1.5 eV can be related to the exponential energy distribution of localized states in metal phthalocyanines (MPc) reported in [5], where these states were attributed to the fluctuations of the electrostatic potential appearing due to the presence of charged ions (e.g., MPc^+ and O_2^-).

In the region of $h\nu < 1.4$ eV, the spectra of αη exhibit three local maxima corresponding to the quantum energies 1.12, 1.21, and 1.36 eV. The positions of

these maxima are close to the positions of absorption peaks in the transmission spectra of thick (10–30 μm) single crystal flakes of CuPc [6] and in the photoconductivity spectra of CuPc in the near-IR range [7, 8]. The intense absorption at 1.12–1.14 eV is assigned to the transition from the ground state (S_0) to the excited triplet state (T_1), which probably becomes allowed due to the spin–orbit interaction caused by the heavy metal atom. The assignment of the peak at $h\nu = 1.12$ eV in the $\alpha\eta$ spectra to the $S_0 \longrightarrow T_1$ transition is confirmed by the coincidence of this value with the position of the intense peak in the PL spectra of the samples studied.

A comparison of the PL spectra (Fig. 1) and the $\alpha\eta$ curves (Fig. 2) reveals certain correlations. The maximum PL intensity among the CuPc films studied is observed for sample 2, which exhibits the minimum absorption in the region of energies below the bandgap of CuPc. The intense PL in this sample is probably indicative of a lower concentration of the centers of nonradiative recombination as compared to that in the two other samples. This assumption is confirmed by the results of photoconductivity measurements for the films irradiated by light with a quantum energy of 1.95 eV. The room-temperature photoconductivity of sample 2 was about ten times greater as compared to the values for samples 1 and 3. A decrease in the concentration of the centers of nonradiative recombination may also account for the decrease in the relative intensity of absorption at $h\nu = 1.12$ eV observed in the $\alpha\eta$ spectrum. Since this spectrum is provided by the photoconductivity measurements, a decrease in the concentration of these centers may lead to a lower rate of autoionization of the Frenkel excitons appearing upon the excitation of molecules from the ground to the triplet state. Accordingly, the relative photoconductivity corresponding to the $S_0 \longrightarrow T_1$ transitions must decrease as well.

Thus, we have established a correlation between the absorption by defects with energy states in the forbidden band of CuPc and the $S_0 \longrightarrow T_1$ transitions responsible for the PL in this compound. We believe that, using a combination of the constant photocurrent method and PL measurements, it is possible to optimize the technology of CuPc (including their chemical modification) for various applications in optoelectronics.

REFERENCES

1. Z. G. Ji, K. W. Wong, P. K. Tse, *et al.*, Thin Solid Films **402**, 79 (2002).
2. L. Goris, K. Heinen, M. Nesladek, *et al.*, Proc. SPIE **5464**, 372 (2004).
3. P. S. Vincett, E. M. Voigt, and K. E. Rieckhoff, J. Chem. Phys. **55**, 4131 (1971).
4. J. Simon and J. J. Andre, *Molecular Semiconductors: Photoelectrical Properties and Solar Cells* (Springer-Verlag, Berlin, 1985).
5. H. Naito, K.-H. Kishimoto, and T. Nagase, Thin Solid Films **331**, 82 (1998).
6. M. Schott, J. Chem. Phys. **44**, 429 (1966).
7. P. Day and R. J. P. Williams, J. Chem. Phys. **42**, 4049 (1965).
8. S. E. Harrison, J. Chem. Phys. **50**, 4739 (1969).

Translated by P. Pozdeev

Technical Physics Letters, Vol. 31, No. 9, 2005, pp. 785–787. Translated from Pis'ma v Zhurnal Tekhnicheskoĭ Fiziki, Vol. 31, No. 18, 2005, pp. 44–49.

Threshold Electron Impact Ionization of SF_6 Molecule

A. N. Zavilopulo*, O. B. Shpenik, A. V. Snegursky, F. F. Chipev, and V. S. Vukstich

Institute of Electron Physics, National Academy of Sciences of Ukraine, Uzhgorod, Ukraine

** e-mail: an@zvl.iep.uzhgorod.ua*

Received April 4, 2005

Abstract—The relative cross sections of a dissociative ionization of SF_6 molecules by electron impact in the near-threshold energy region have been determined. The experiments were performed on a setup providing for ion mass separation and detection using a monopole mass spectrometer. The energy dependences of the cross sections of fragment ion formation have been measured and the corresponding appearance thresholds are determined. © *2005 Pleiades Publishing, Inc.*

Experimental investigations of the products of the dissociative ionization of SF_6 molecules upon single electron impact in the region of threshold energies are of considerable importance for applications, since sulfur hexafluoride is among the most widely occurring technogeneous gases. Being artificially created, SF_6 molecules possess a number of unique physicochemical properties. This compound is widely used in various modern technologies, for example, in plasma etching of semiconductors and in devices for the transmission and distribution of high voltages. SF_6 plays an important role in the creation of active media for excimer lasers. Sulfur hexafluoride provides a solution for many technical problems involving the need for effective sound absorption and thermal insulation. In recent years, additional attention to sulfur hexafluoride was attracted in the context of environmental problems related to the increasing greenhouse effect in the Earth's atmosphere, where the potential contribution of SF_6 can be four orders of magnitude greater than that of carbon dioxide [1].

The interaction of SF_6 with low-energy electrons has been extensively studied (see, e.g., review [1]). However, most of the available papers do not pay much attention to the laws governing the thresholds of the elementary processes that accompany the interactions of electrons with SF_6 molecules. Moreover, the published results are rather contradictory.

We have studied the energy dependences of the cross sections for the formation of fragment ions (S^+, F^+, F_2^+, SF^+, SF_2^+, SF_3^+, SF_4^+, and SF_5^+) upon the electron impact ionization of sulfur hexafluoride. The main attention was devoted to the measurement of the appearance potentials (E_{ap}) of the above fragment ions. This investigation was inspired by the fact that the well-known NIST database of the atomic and molecular constants [2] gives, for example, ten different values of the appearance potential for SF_2^+, with the differences amounting to 2–5 eV.

The experiments were performed in a vacuum setup with an oilless pumping stage. The setup was equipped with an MX-7304A monopole mass spectrometer. Ions separated by the analyzer were detected by a system capable of operating in the regimes of the manual, cyclic, and programmed sweep of the ion mass range and the electron energy range, with a digital indication of the ion mass and intensity. The experimental procedure is described in detail elsewhere [3], and here we will only briefly mention the main methodological aspects of this study.

The beam of SF_6 molecules was generated by a multichannel source of the effusion type, which allowed the concentration of molecules in the region of interaction with the electron beam to be maintained at a level of 10^{10}–10^{11} cm^{-3}. The ion source with electron impact ionization was operating in the regime of stabilized electron current. In this regime, the electron gun produced a beam with controlled energy, a beam current of 0.5–1.5 mA, and an electron energy spread not exceeding ΔE = 500 meV (full width at half maximum of the electron energy distribution). Ions extracted from the region of interaction of the electron and molecular beams were transported via the ion optics system of the analyzer, separated with respect to masses, and detected by a detector capable of operating in both the analog and count regimes of the ion current measurement. The ion mass and electron energy scales were calibrated using Ar and Xe ion beams.

In the first stage of the experiment, the electron energy was set at E = 70 eV and a control mass spectrum was obtained, with the automatic subtraction of the signal of a residual gas background from the signal due to SF_6 ions. Using this spectrum, it was possible to judge the relative yield of fragment ions, as well as the purity of the substance studied. In our experiments, the

1063-7850/05/3109-0785$26.00 © 2005 Pleiades Publishing, Inc.

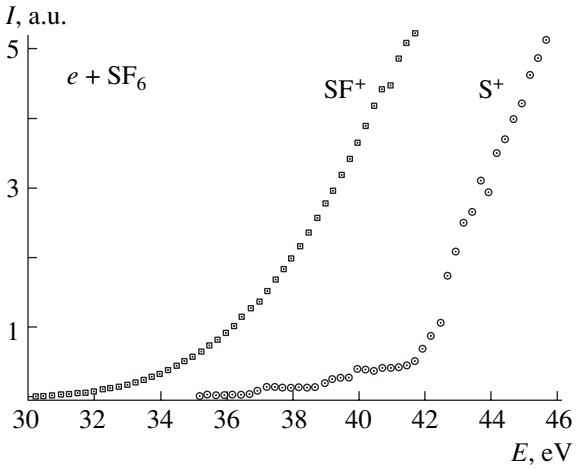

Fig. 1. Near-threshold region of the energy dependence of the cross section for the yield of SF^+ and S^+ ions in the course of the dissociative electron impact ionization of SF_6.

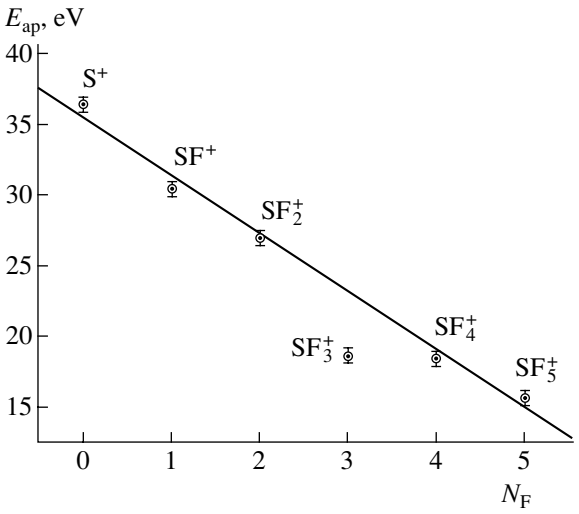

Fig. 2. A plot of the appearance potential E_{ap} for various fragment ions of SF_6 versus the number of fluorine atoms in the fragment.

intensities of the peaks of background ions (not entering into the composition of sulfur hexafluoride) did not exceed 2% of the most intense peak due to the SF_5^+ ion.

The SF_6 molecule has a radial-symmetric structure, with the central atom of sulfur bound to six fluorine atoms. This molecular structure accounts for the presence of the peaks of fragments with different numbers of fluorine atoms in the ion mass spectrum, the intensities of which reflect the effective cross section of the sequential dissociative ionization of SF_6 molecule by electron impact. It should be noted that the obtained spectrum did not contain a peak corresponding to SF_6 molecules. This is probably related to the fact that the SF_6^+ ion (ionization threshold, E_i = 15.32 eV [2]) is unstable both in the ground state and in the excited states. This ion rapidly (within picoseconds) dissociates with the formation of fragment ions and neutrals [4].

In the next stage, the mass spectrometer was tuned to transmit ions with a selected mass, and the dependence of the amount of such ions on the electron beam energy was measured in the automated regime. This dependence was used to determine the appearance potential of the given fragment ion using a special procedure developed for the processing of data on the threshold cross section (see, e.g., [3]). It should be noted that the accuracy of determination of the appearance potential of a fragment ion depends on the accuracy of determination of the primary electron energy. As was mentioned above, the system calibration was performed using Ar and Xe atoms, for which the initial regions of the electron impact ionization function were measured. The correctness and reliability of this approach could be judged by the results of a control experiment, in which the initial regions of the electron-impact ionization cross section for Kr was measured using a procedure analogous to that described in [5]. In this way, the electron energy scale was established with an error not exceeding ±0.5 eV, which is comparable with the electron energy spread in the primary beam.

Figure 1 shows the near-threshold regions of the energy dependence of the cross sections for the formation of SF^+ and S^+ ions. These curves were obtained by the cyclic scanning of a selected energy interval at a 0.25-eV step. The data for these fragment ions are of special interest because they possess the maximum appearance potentials E_{ap} (compared to those of the other fragments) and, hence, can provide information about the contributions to the electron impact dissociation of SF_6 related to the other fragments. Indeed, a characteristic feature of the curves in Fig. 1 is a strong "delay" in the initial regions, with several deviations from smooth monotonic growth in the curve for the S^+ fragment. This behavior is probably explained by the sequential switching of various mechanisms of the S^+ ion formation depending on the energy of ionizing electrons. The rate of the cross section growth for sulfur ions gradually increases with the electron energy and the curve exhibits a more extended delayed portion of the near-threshold energy dependence.

Using the initial regions of the energy dependences of the cross sections for the yield of fragment ions formed as a result of the dissociative ionization of SF_6 molecules by electron impact, we determined the corresponding appearance potentials. Figure 2 shows a plot of the absolute values of the appearance potential E_{ap} for the fragment ions studied (except for F^+ and F_2^+, which have a different nature of formation) versus the number of fluorine atoms in the fragment (i.e., versus the mass of the fragment). Note that the plot is virtually linear. This behavior generally confirms the notion of the sequential detachment of fluorine atoms from the initial SF_6 molecule upon the electron impact with

increasing energy. The only fragment violating the linear dependence (Fig. 2) is SF_3^+. This deviation is probably related to the presence of competitive channels for the fragmentation of the initial molecule, which reduce the appearance potential for this ion as compared to the E_{ap} values for the other reaction products. Certain peculiarities of the formation of this ion were previously reported, for example, in [6], although the mechanism considered in that case could be operative in the region of higher energies (above 40 eV).

In conclusion, we have used a combination of the crossed beam technique and mass spectrometry and measured for the first time the initial regions of the energy dependences of cross sections for the yield of fragment ions of SF_6 in the course of the dissociative electron impact ionization. In some cases, the cross sections deviate from monotonic variation. We have also established for the first time a linear variation of the absolute values of the appearance potentials for S^+, SF^+, SF_2^+, SF_3^+, SF_4^+, and SF_5^+ ions depending on the ion mass.

REFERENCES

1. L. G. Christophorou and J. K. Olthoff, J. Phys. Chem. Ref. Data **29**, 267 (2000).
2. *NIST Standard Reference Database*, http.www.webbook.nist.gov.
3. A. N. Zavilopulo, F. F. Chipev, and O. B. Shpenik, Zh. Tekh. Fiz. **75** (4), 19 (2005) [Tech. Phys. **50**, 402 (2005)].
4. R. K. Singh, R. Hippler, and R. Shanker, Phys. Rev. A **67**, 022704 (2003).
5. A. N. Zavilopulo and A. V. Snegursky, Pis'ma Zh. Tekh. Fiz. **28** (11), 68 (2002) [Tech. Phys. Lett. **28**, 913 (2002)].
6. S. Feil, K. Gluch, P. Scheier, *et al.*, J. Chem. Phys. **120**, 11465 (2004).

Translated by P. Pozdeev

Technical Physics Letters, Vol. 31, No. 9, 2005, pp. 788–792. Translated from Pis'ma v Zhurnal Tekhnicheskoĭ Fiziki, Vol. 31, No. 18, 2005, pp. 50–60.

A Model of Mechanical Polishing in the Presence of a Lubricant

V. L. Popov[a,b] and A. É. Filippov[b]

[a] *Berlin Technical University, Berlin, Germany*

[b] *Donetsk Physicotechnical Institute, Donetsk, Ukraine*

Received April 28, 2005

Abstract—Modeling of the friction and wear at the contact of rough surfaces in the presence of a lubricant is important for the development of modern technologies. This is a complex problem involving a consistent description of the elastic straining of contacting bodies and of the flow of viscous liquid between them. It is demonstrated that this problem can be significantly simplified in the most interesting case, in which the lubricant thickness is very small and the decisive contribution to both the contact interaction and the friction force is due to the interactions between a finite number of inhomogeneities approaching one another to a certain distance, this distance being much smaller than the average distance between the two bodies. The lubricant dynamics can be modeled in terms of the nonconservative interactions between the particles, which depend on the distance and relative velocity. The proposed approach is used to describe the process of mechanical polishing in the presence of abrasive particles suspended in the lubricant layer. This hydrodynamic polishing process results in the formation of a surface relief with a statistically equilibrium roughness that exhibits a fractal character.

In recent years, the task of obtaining high-quality surfaces with the desired parameters of both a macroscopic inhomogeneity and a microscopic roughness has become very important. The problem of creating such surfaces is encountered, for example, in the production of magnetic disks and integrated chips. The solid surfaces are frequently processed using the method of chemical-mechanical polishing [1], according to which the disk of a polished material (e.g., silicon wafer) is brought into contact with a rotating substrate via a lubricant layer. The lubricant layer may contain suspended abrasive particles. In the typical regime, the abrasive particles do not have direct contacts with the surface of a processed material. Irreversible changes in the surface topography are caused by fluctuations of the pressure developed in a thin lubricant layer separating the abrasive particles and the processed surface. The laws of such a "hydrodynamic polishing" process have not been theoretically studied until now.

This Letter describes a model of the process of surface topography variation as a result of the interaction with abrasive particles suspended in the lubricant layer. In order to increase the efficiency of the numerical model, we have developed a new approach to the description of the hydrodynamic interaction. According to this, the interaction mediated by a liquid layer can be modeled without solving the corresponding hydrodynamic problem. The proposed approach is used to model the process of friction at the contact of two rough surfaces in the presence of a lubricant layer.

Hydrodynamic forces at a single contact. In the aforementioned problem of hydrodynamic polishing, we deal with a system in which the average distance between the two surfaces is much greater than the minimum distance to which the abrasive particles approach the processed surface at a "contact" site. As will be shown below, the main contribution to the interaction force in this case is related to the small vicinity of the point of maximum approach. Taking this into account, we can reduce the description of the interaction between two surfaces to the description of forces arising in pairs of such microcontacts in the presence of a liquid. A single microcontact will be modeled using a hard spherical surface of radius R, which approaches a plane. Since the main contribution to the force is related to the small vicinity of the point of maximum approach, the hydrodynamics in the liquid layer can be considered using the Reynolds approximation [2].

The idea of the proposed approach can be illustrated using the following example. Consider a hard sphere of radius R approaching at a small velocity a solid plane in a liquid medium (Fig. 1). The distribution of pressure in the liquid medium in the Reynolds approximation is described by the equation

$$\frac{dp}{dr} = -\frac{6\eta r\dot{h}}{h(r)^3}, \tag{1}$$

where η is the dynamic viscosity of the liquid, r is the polar radius measured from the point of maximum approach, and $h(r) = h_0 + r^2/2R$ is the distance from a point on the spherical surface to the plane. Integrating

1063-7850/05/3109-0788$26.00 © 2005 Pleiades Publishing, Inc.

Eq. (1), we obtain an expression describing the pressure distribution in the liquid:

$$p = -\int \frac{6\eta r\dot{h}}{h(r)^3}dr = -\int \frac{6\eta r\dot{h}}{(h_0 + r^2/2R)^3}dr = \frac{3\eta\dot{h}R}{(h_0 + r^2/2R)^2} + p_\infty. \quad (2)$$

The total force with which the liquid acts upon the sphere is

$$F = \int (p(r) - p_\infty)dr = \int_0^{\sim R} \frac{4\eta\dot{h}R}{(h_0 + r^2/2R)^2}2\pi r dr.$$

Since the integral in (2) converges at the upper limit, this limit can be replaced by the infinity:

$$F \approx \int_0^\infty \frac{3\eta\dot{h}}{(h_0 + r^2/2R)^2}2\pi r dr = \frac{6\pi\eta\dot{h}R^2}{h_0}. \quad (3)$$

The convergence of this integral implies that regions occurring sufficiently far from the contact (at distances much greater than $r \approx \sqrt{2Rh_0}$) practically do not contribute to the interaction between the two surfaces. Therefore, it is necessary to determine only the character of flow in the immediate vicinity of the point of maximum approach.

Using Eq. (3), we can determine the force of interaction between two rough surfaces via the liquid layer without solving hydrodynamic equations—merely by determining the statistics of the heights and curvature radii of the microscopic roughnesses and summing the forces given by formula (3) over all the pairs of closely spaced roughnesses (or roughnesses and suspended abrasive particles).

The proposed approach can be further developed in application to the case where the interacting particles can be characterized by a certain radius of curvature. Equation (3) shows that the force of interaction between a sphere and a solid plane is proportional to the relative velocity and inversely proportional to the distance between the two surfaces. It can be readily shown that the same relation is observed in the case of a central interaction between elements of the spherical surface and elements of the plane according to the law

$$dF = \frac{6\eta R}{\pi}\frac{v}{r^4}dAdA', \quad (4)$$

where dA and dA' are the surface elements of the sphere and the plane, respectively; r is the distance between these elements; and v is the velocity of their mutual approach. The integration of force (4) over all the elements of the sphere and the plane under the condition $h \ll R$ leads to relation (3). The nonlocal character of the interaction of solids via the liquid layer is manifested by the explicit dependence of the interaction force on the radius R.

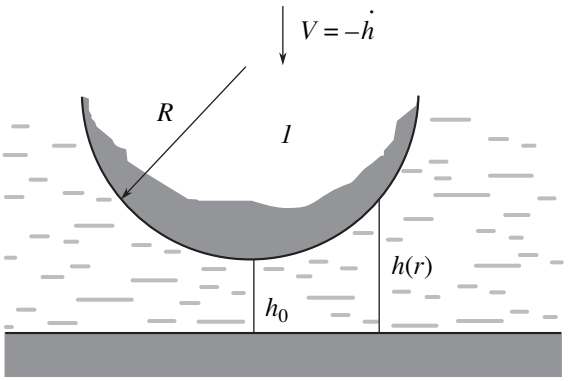

Fig. 1. A model of the microscopic contact between a hard spherical particle (*1*) and a solid surface.

The main advantage of passing from the exact interaction via liquid to the central interactions (4) consists in the possibility of modeling friction between randomly rough surfaces without solving the hydrodynamic equations.

Description of model. Below we consider the simplified discrete model of elastic bodies schematically depicted in Fig. 2. The model represents a series of equidistant material points elastically bound to a hard surface possessing a preset profile. It will be assumed that the surfaces interact only via particles suspended in the lubricant layer. As was demonstrated above, this interaction can be described using forces of the type given by formula (4), which depend on the distances between particles and on their relative velocities. Inelastic interactions between the particles and surfaces will be described as follows: if the force acting upon a particle on the surface exceeds a preset yield point, the "seeding" profile exhibits a depression or protrusion, depending on the sign of this pressure.

A system of dynamic equations for the model described above can be written as follows:

$$\partial v_{z1,2}/\partial t = K_z(w_{1,2}(x) - z_{1,2}(x)) + K_z(z_{1,2}(x + dx) + z_{1,2}(x - dx) - 2z_{1,2}(x)) - F^{(1,2)}_{z\,\text{liquid}} - F^{(1,2)}_{z\,\text{repuls}}. \quad (5)$$

$$\partial V_{x,z}/\partial t = \sum_{(1,2)} [F^{(1,2)}_{x,z\,\text{liquid}} + F^{(1,2)}_{x,z\,\text{repuls}}] - F_{x,z\,\text{diss}} + D\zeta(X, Z),$$

where $\partial X/\partial t = V_x$; $\partial Z/\partial t = V_z$; $\partial x_{1,2}/\partial t = v_{x1,2}$; $\partial z_{1,2}/\partial t = v_{z1,2}$; K_z is the elastic constant of bonds between

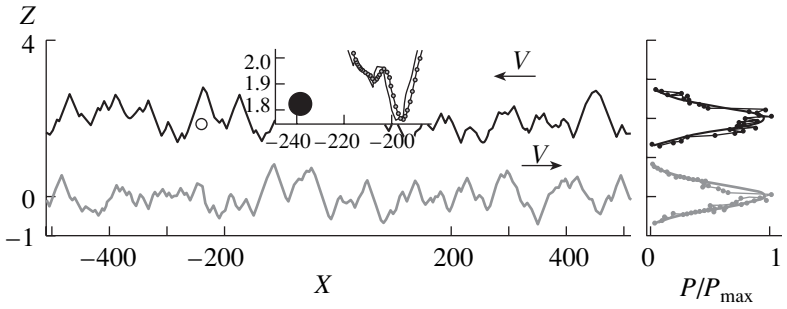

Fig. 2. A discrete model of the contact between two elastic rough surfaces. The diagram shows a fragment of the two-dimensional (x, z) section with the hard "seeding" profiles of the upper (black curve) and lower (gray curve) surfaces. Arrows indicate the directions of motion. The central inset shows deviations of the material points (small black circles) from the seeding profiles. The big black circle shows an abrasive particle suspended in the lubricant layer, which produced these deviations. The right-hand inset shows the instantaneous (points) and time-averaged (solid curves) distributions of the heights of both surfaces obtained as a result of polishing.

mobile elements (material points) of the upper and lower surfaces in positions with the coordinates $z_{2,1}(x)$, respectively, and the quasi-static "seeding" profiles $w_{2,1}(x)$ of the same surfaces; and the sum $\Sigma_{(2,1)}$ is taken over all elements of both surfaces. In addition, we take into account the intrinsic elasticity of these surfaces, which will be roughly approximated by the elastic bonds $K_z(z_{1,2}(x + dx) - z_{1,2}(x))$ (with the same elastic constant K_z as above) in the sequence of surface elements spaced by dx on each surface.

If the absolute value of the difference $|w_{1,2}(x) - z_{1,2}(x)|$ exceeds the yield point W, the surfaces $w_{2,1}(x)$ exhibit a relatively small plastic deformation. According to the proposed model, this deformation is described using the relations

$$w_{2,1}(x) = w_{2,1}(x) \quad \text{for} \quad |w_{2,1}(x) - z_{2,1}(x)| < W;$$
$$w_{2,1}(x) = \mu w_{2,1}(x) + \nu z_{2,1}(x) \quad \text{for } |w_{2,1}(x) - z_{2,1}(x)| > W, \qquad (6)$$

where $\mu + \nu = 1$ and $\mu/\nu \gg 1$. These relations should be considered jointly with Eqs. (5).

With neglect of the interactions between particles occurring between the surfaces, we may consider the result of the joint action of particles upon these surfaces as produced by a single particle in a certain statistical realization of the process (with averaging over a long time of the numerical experiment or over multiply repeated realizations). The coordinates of this particle will be denoted (X, Y).

The interaction of a particle with elements of the surface is a sum of the aforementioned liquid friction $F^{(1,2)}_{x,z\,\text{liquid}}$ and the repulsion between this point and the surface elements. For simplicity, the repulsion potential can be set as a Gaussian function of the distance, $U_{1,2} = Cc\exp\{-[(X - x_{1,2})^2 + (Z - z_{1,2})_2]/c\}/2$, such that $F^{(1,2)}_{x\,\text{repuls}} = -\partial U_{1,2}/\partial x$ and $F^{(1,2)}_{z\,\text{repuls}} = -\partial U_{1,2}/\partial z$.

The temperature fluctuations must also be taken into account (as usual, within the framework of the Langevin equation) by introducing a δ-correlated random force $D = 2k_BT\eta$ ($\langle\zeta(X, Z; t)\zeta(X', Z'; t)\rangle = D\delta(X' - X')\delta(Z' - Z')\delta(t' - t')$) and a dissipation with the intensity proportional to the difference between velocities of the particle and each surface $F_{z\,\text{diss}} = \eta V_z$; $F^{(1,2)}_{z\,\text{diss}} = \eta(V_x \pm V)$.

For the symmetry (which increases the accuracy of numerical experiments in the case under consideration), we assume that the upper and lower surfaces move with equal velocities V in the opposite directions as shown in Fig. 2. In this case, the lateral dissipative force is $F_{x\,\text{diss}} = \eta(V_x + V) + (V_x - V) = 2\eta(V_x)$.

We will use the mirror boundary condition for the particle in the Z direction. According to this condition, the particle going outside the interval between $\langle w_2(x)\rangle$ and $\langle w_1(x)\rangle$ is returned back with the same value and opposite direction of the velocity V_z. The boundary conditions in the X direction are periodic.

The formation of equilibrium friction surface. The results of numerical experiments using the model described above showed that the local collisions of abrasive particles with the surface inhomogeneities lead to a continuous change in the surface topography with the formation of a certain equilibrium roughness. If a numerical experiment starts with smooth surfaces, they eventually become rough. Figure 3 shows the typical example of a quasi-random walk of an abrasive particle suspended in a lubricant layer (occurring at the origin at $t = 0$). This motion resembles at first glance the usual diffusion, but a more thorough analysis shows that the diffusion should be considered as anomalous. The main sign of the anomalous diffusion is the presence of long jumps (ballistic flights) [3–5].

In the case under consideration, these ballistic flights have both a simple meaning and large practical significance. Indeed, statistical analysis shows that the flights are related to periods in which the particle approaches significantly closer to the upper or lower

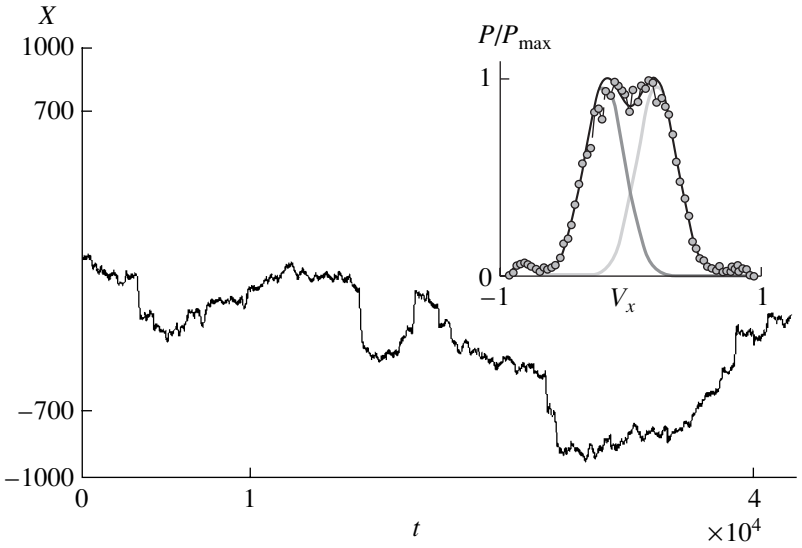

Fig. 3. The typical scenario (time series) of a quasi-random walk of an abrasive particle suspended in a lubricant layer (occurring at the origin at $t = 0$). The inset shows the distribution of the instantaneous particle velocities $P(V_x)$ (open circles) accumulated for the given time series, the distribution averaged over the ensemble (thick solid curve), and the distributions corresponding to the periods of motion when the particle moves predominantly together with the upper (thin solid curve) or lower (gray curve) surface.

surface and, accordingly, more intensively interacts with the surface. In these states, the particle moves together with the corresponding surface and may stray a rather large distance from the initial position. This circumstance is substantially related to the liquid friction in the system with lubricant, which significantly increases the intensity of liquid stirring and, hence, the efficiency of the polishing process.

These considerations are illustrated in the inset to Fig. 3, which shows the distribution of the instantaneous particle velocities $P(V_x)$ (open circles) accumulated for the particular time series of diffusion presented in Fig. 3. For the comparison, we also present the distribution $P(V_x)$ averaged over the ensemble (thick solid curve) and the distributions corresponding to the periods of motion when the particle moves predominantly together with the upper (thin solid curve) or lower (gray curve) surface.

The irreversible changes of surface topography described by relations (6) lead to a constant shift of the surfaces in the opposite directions along the Z axis, which reflects the wear that has occurred as a result of polishing (or a total shift $dZ < 0$ necessary to maintain the constant spacing between the surfaces). Accumulating the shift, we obtain the dependence $dZ(t)$ reflecting the wear that has occurred at a practically constant rate in the course of polishing (Fig. 4). The inset to Fig. 4 shows the distribution of the probability of finding the particle at a point with the coordinate Z between the plates (the data were accumulated for the same particular scenario as that used to determine the $dZ(t)$ dependence). As can be seen, the particle occurs predominantly in the immediate vicinity of each surface and rather frequently enters the regions where it is on the average close to one or another surface. This behavior increases the intensity of polishing and is consistent with the aforementioned mechanism of anomalous diffusion.

One of the most important characteristics of the process under consideration is the spectral structure $C(q)$ of the quasi-equilibrium surfaces formed as a result of polishing. The results of multiply repeated numerical experiments performed in a broad range of the parame-

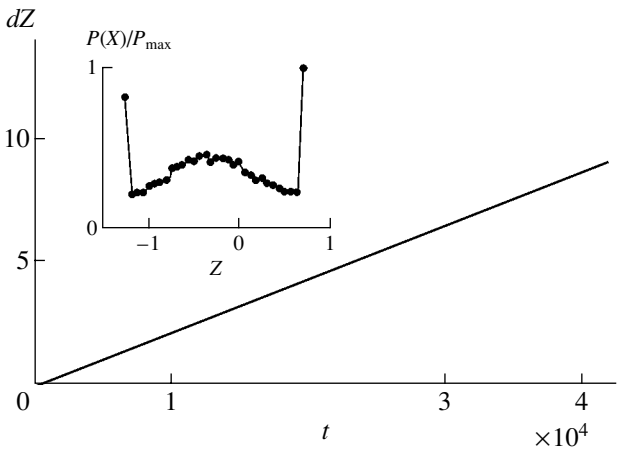

Fig. 4. The wear of surfaces caused by their interaction with an abrasive particle suspended in the lubricant layer (for the time series presented in Fig. 3). The function $dZ(t)$ reflects the total accumulated shift of the average positions $z_{1,2}$ over the time t, which is necessary to maintain a constant average spacing between the polished surfaces. The inset shows the distribution of the probability of finding the particle at a point with the coordinate Z between the plates for the same time series.

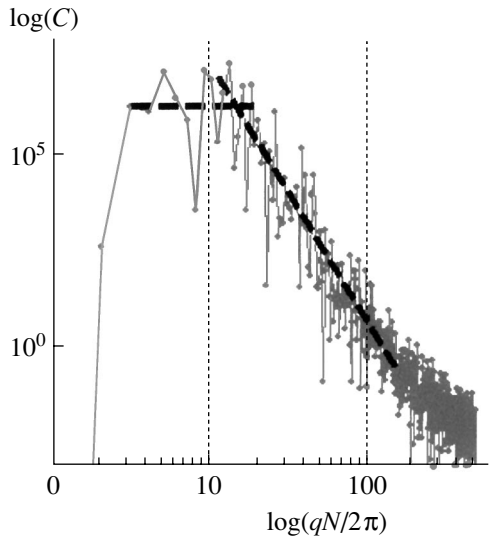

Fig. 5. The typical spectral density curve $C(q)$ for quasi-equilibrium surfaces obtained as a result of polishing. Such a density spectrum is typical of a broad class of real surfaces [6]. In the region of the variable q between the vertical dashed lines, the $C(q)$ function exhibits a scaling behavior, with the range of scales from 10 to 100 units of length dx in the real space.

ters of Eqs. (5)–(6) showed that such surfaces are stably formed within the framework of this model under rather arbitrary initial conditions (flat plates, surfaces generated by random throwing, or surfaces determined by certain spectral structures).

Figure 5 shows the typical spectral density curve $C(q)$ for quasi-equilibrium surfaces $z_{1,2}$ obtained as a result of polishing. Such a density spectrum is typical of a broad class of real surfaces [6]. In particular, the given profile contains a well-pronounced region of the variable q where the $C(q)$ function exhibits a scaling behavior. This region (indicated by vertical dashed lines in Fig. 5) corresponds to the scales from 10 to 100 units of length dx in the real space.

Conclusion. We have developed a new effective approach to the modeling of the elastic-hydrodynamic contacts between rough solid surfaces and of the process of surface topography variation during friction. It was demonstrated that the relative motion of two bodies separated by a lubricant layer containing suspended abrasive particles leads to the formation of statistically equilibrium surfaces with a characteristic fractal topography. The proposed method of modeling can be used for the optimization of parameters of the polishing process used in hard memory disk technology.

Acknowledgments. The authors are grateful to Deutsche Forschungsgemeinschaft for financial support of this work.

REFERENCES

1. G. Nanz and L. E. Camilletti, IEEE Trans. Semicond. Manuf. **8**, 382 (1995).
2. L. D. Landau and E. M. Lifshitz, *Course of Theoretical Physics*, Vol. 6: *Fluid Mechanics* (Nauka, Moscow, 1986; Pergamon, New York, 1987).
3. M. F. Shlesinger, G. M. Zaslavsky, and J. Klafter, Nature (London) **363**, 31 (1993).
4. J. Klafter, M. F. Shlesinger, and G. Zumofen, Phys. Today **49**, 33 (1996).
5. G. Zumofen and O. Klafter, Phys. Rev. E **51**, 1818 (1995).
6. B. N. J. Persson, O. Albohr, U. Tartaglino, *et al.*, J. Phys.: Condens. Matter **17**, R1 (2005).

Translated by P. Pozdeev

Technical Physics Letters, Vol. 31, No. 9, 2005, pp. 793–795. Translated from Pis'ma v Zhurnal Tekhnicheskoĭ Fiziki, Vol. 31, No. 18, 2005, pp. 61–65.

Additivity of the Crystal Structure and Properties of Solid Solutions of Rare Earth Metal Hexaborides

V. N. Gurin*, L. I. Derkachenko, and M. M. Korsukova

Ioffe Physicotechnical Institute, Russian Academy of Sciences, St. Petersburg, 194021 Russia

** e-mail: vladimir.gurin@mail.ioffe.ru*

Received May 19, 2005

Abstract—Single crystals of solid solutions of the rare earth metal (REM) hexaborides LaB_6–CeB_6 and EuB_6–SrB_6 have been grown from solutions in aluminum melt. The chemical compositions of the samples were determined by energy-dispersive X-ray spectroscopy; the crystal lattice periods were determined by X-ray diffraction; and the microhardness on a {001} cubic face in the 0° (90°) azimuthal direction was measured using the Knoop indenter. The properties of the mixed solid solutions of REM hexaborides are described using the concept of additivity, whereby the lattice period and the microhardness are determined as linear functions of the concentrations (atomic fractions) of both metals. It is established that both characteristics obey the corresponding linear relationships and vary between the values for the initial pure hexaborides. The accuracy of the calculated additive characteristics depends on the precision of determination of the chemical composition of samples. The accuracy of experimental data is determined by the precision of particular techniques, the structural perfection of single crystals, and (for microhardness) the state of the sample surface. © *2005 Pleiades Publishing, Inc.*

The additive characteristics of a complex system are determined as sums over the system components or as linear functions of the concentrations of these components [1]. Such additivity is an important and interesting phenomenon encountered, for example, in the study of mixed solid solutions of various compounds. In particular, it can be of large practical significance in the synthesis and characterization of solid solutions of rare earth metal (REM) hexaborides such as LaB_6–CeB_6 [2]. Unfortunately, the absence of systematic published data on the phase diagrams of quasibinary solid solutions of the REM^1B_6–REM^2B_6 systems hinders the description of such phase diagrams (see figure) with a reasonable precision. Using the fragmentary data available in the literature and the results of our own investigations, we may only ascertain the unlimited mutual solubility of REM hexaborides. This is a quite reasonable conclusion in view of the proximity of the atomic and ion radii of the rare earth elements.

In this paper, we present the results of a comparative analysis of the calculated and experimental data on the crystal lattice periods and Knoop microhardnesses for solid solutions of the two mixed REM hexaboride systems, LaB_6–CeB_6 and EuB_6–SrB_6, and show the additivity of these characteristics for the compounds studied. Of course, we are speaking of real behavior (rather than of the ideal, mathematically exact additivity) within the limits of precision of the particular experimental methods used for the investigation of single crystal solid solutions of REM hexaborides.

The single crystals of La, Ce, Eu, and Sr hexaborides were grown from solutions in aluminum melt [3], which were prepared using initial components with a purity of not less than 99.7–99.9 mass %; the excess Al was dissolved in hydrochloric acid (HCl) of the reagent grade. The synthesis was performed in a furnace of the Lynn type under a flow of argon (>99.99 mass % Ar). The mixture was slowly (within 4–6 h) heated to 1250–1350°C, kept at a constant temperature for 4 h, and then cooled with the furnace to room temperature over 20–24 h. After the dissolution of

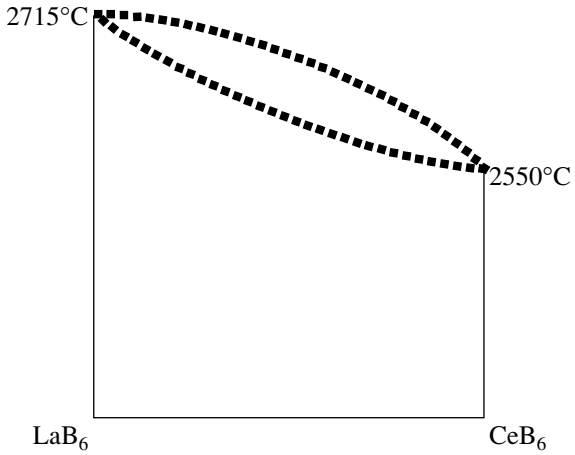

A quasibinary phase diagram of the LaB_6–CeB_6 hexaboride system (the liquidus and solidus lines are depicted by dashed curves because of the lack of experimental data).

1063-7850/05/3109-0793$26.00 © 2005 Pleiades Publishing, Inc.

Table 1. Comparison of the measured and calculated values of the lattice periods of solid solutions of REM hexaborides

Sample composition*	Atomic fractions and lattice periods of components, Å		Lattice period of mixed REM hexaboride, Å	
	REM^1B_6	REM^2B_6 (REM^3B_6)	calculation	experiment
$La_{0.28}Ce_{0.72}B_{5.55}$	Ce: 0.72 × 4.1396	La: 0.28 × 4.1563	4.1443	4.1443(3)
$La_{0.40}Ce_{0.60}B_6$	Ce: 0.6 × 4.1396	La: 0.4 × 4.1563	*4.1463*	4.1470(3)
$La_{0.68}Ce_{0.32}B_{5.65}$	La: 0.68 × 4.1563	Ce: 0.32 × 4.1396	*4.1510*	4.1520(4)
$La_{0.70}Sr_{0.30}B_6$	La: 0.7 × 4.1563	Sr: 0.3 × 4.197	*4.1685*	4.1620(4)
$Eu_{0.86}Sr_{0.14}B_6$	Eu: 0.86 × 4.1844	Sr: 0.14 × 4.197	*4.1862*	4.1870(1)
$Eu_{0.38}Sr_{0.62}B_6$	Sr: 0.62 × 4.197	Eu: 0.38 × 4.1844	*4.1922*	4.1910(1)
$Eu_{0.05}Sr_{0.95}B_6$	Sr: 0.95 × 4.197	Eu: 0.05 × 4.1844	*4.1964*	4.1970(1)
$La_{0.7}Ce_{0.15}Pr_{0.15}B_6$	La: 0.7 × 4.1563	Ce: 0.15 × 4.1396 Pr: 0.15 × 4.1327	*4.1502*	4.1530(2)

* Experimental data (error, ±0.01–0.02 at. fraction).

the excess aluminum in diluted (1 : 4) aqueous HCl, the samples in the form of whiskers (3–7 mm long), thin plates (up to 3 × 5 mm), or isometric crystals (up to 2 × 2 × 3 mm) were selected under microscope (MBS-9) and studied. The chemical compositions of the samples were determined by energy-dispersive X-ray spectroscopy. The crystal lattice periods were determined by X-ray diffraction using the Guinier–Hagg technique. The microhardness was measured using the Knoop indenter (PMT-3) at a load of 490 mN. In order to eliminate uncertainties in the microhardness, the measurements were performed after the removal of the surface oxide film by etching for 5 min in a diluted (1 : 4) aqueous nitric acid HNO_3.

The accuracy of calculations of an additive characteristic y (e.g., the crystal lattice period a or the Knoop microhardness H_K) of a two-component solid solution depends on two main factors. The first is the accuracy of determination of the chemical composition, that is, of the exact atomic fractions of components (X and $1 - X$) forming the solution. The second is the degree of perfection of the crystal structure of solid solutions and their components (elements or compounds). In order to provide for the correct comparison, it is necessary that this degree (e.g., the defectness of sublattices) in solid solutions be the same as that in pure hexaborides.

We have experimentally determined the precise values of the lattice period for single crystals in both systems of solid solutions (LaB_6–CeB_6 and EuB_6–SrB_6). Using the results of chemical analyses, these values were also calculated as $y = y_{LaB_6}X + y_{CeB_6}(1 - X)$, assuming their additivity in the mixed solid solutions. The results of measurements and calculations are presented in Table 1. As can be seen from these data, the measured and calculated values show a quite good agreement (in view of the high precision of analyses and measurements). Indeed, the maximum difference (for $La_{0.70}Sr_{0.30}B_6$) is 0.0065 Å (the values for which the difference falls outside the limits of experimental accuracy are given in italics), while the two values for $La_{0.28}Ce_{0.72}B_{5.55}$ exactly coincide. Note that large differences are observed for solid solutions of the LaB_6–SrB_6 and EuB_6–SrB_6 systems in which one of the components is not a REM hexaboride (SrB_6). Apparently, the intervals of the existence of solid solutions in such systems may have some specific features. Unfortunately, the lack of published data does not allow us to judge on this possibility. It is also interesting to note the good agreement (a difference of 0.0028 Å at an 0.0002 error: 0.008 or 0.0030 Å) between the calculated and experimental data for a ternary solid solution ($La_{0.7}Ce_{0.15}Pr_{0.15}B_6$). Thus, the additivity of the crystal lattice period in solid solutions of mixed REM hexaborides is satisfactorily confirmed by the experimental results.

Table 2 presents data on the microhardness measured using the Knoop indenter for the same solid solutions of mixed REM hexaborides in which the lattice period was shown to be additive. As can be seen from these data, the difference between the measured values and those calculated for the LaB_6–CeB_6 system using the additive scheme also falls within the experimental error limits. The same is valid for the EuB_6–SrB_6 system with a relatively small content of Sr. A significant difference between experiment and calculation is observed only when the atomic fraction of Sr exceeds 0.5 (these values are given in italics). It should be noted that the microhardness, being a mechanical property characterizing the surface of a sample, strongly depends on the state of this surface (the presence of an oxide film, fine inclusions, and surface relief with nonparallel faces of various heights, various degrees of etching for different metals, etc.). This implies that a correct comparison can be made only for

Table 2. Comparison of the measured and calculated values of the Knoop microhardness H_K of single crystal solid solutions of REM hexaborides measured on a {001} cubic face in the 0° (90°) azimuthal direction at an indenter load of P = 490 mN

Sample composition*	Atomic fractions and H_K values of components, MPa		H_K of mixed REM hexaboride, MPa	
	REM^1B_6	REM^2B_6	calculation	experiment
$La_{0.28}Ce_{0.72}B_{5.55}$	Ce: 0.72 × 24108	La: 0.28 × 23030	23814	22834(1960)
$La_{0.40}Ce_{0.60}B_6$	Ce: 0.60 × 24108	La: 0.40 × 23030	23716	23128(1960)
$La_{0.68}Ce_{0.32}B_{5.65}$	La: 0.68 × 23030	Ce: 0.32 × 24108	23422	23912(1960)
$La_{0.70}Sr_{0.30}B_6$	La: 0.70 × 23030	Sr: 0.30 × 29498	24990	26264(1470)
$Eu_{0.86}Sr_{0.14}B_6$	Eu: 0.86 × 22834	Sr: 0.14 × 29498	23814	24304(1176)
$Eu_{0.38}Sr_{0.62}B_6$	Sr: 0.62 × 29498	Eu: 0.38 × 22834	*26950*	24696(1470)
$Eu_{0.05}Sr_{0.95}B_6$	Sr: 0.95 × 29498	Eu: 0.05 × 22834	*29204*	29460(1470)

* Experimental data (error, ±0.01–0.02 at. fraction).

single crystals whose surfaces occur in similar states. We may ascertain that the additivity of the crystal structure of solid solutions of mixed REM hexaborides must be accompanied by the additivity of those properties that depend on the perfection and type of the crystal lattice.

In conclusion, the measured crystal lattice periods and Knoop microhardnesses in a series of solid solutions of REM hexaborides are additive and can be calculated using the linear rule of mixing.

REFERENCES

1. V. Ya. Anosov, M. I. Ozerova, and Yu. Ya. Fialkov, *Fundamentals of Physicochemical Analysis* (Nauka, Moscow, 1976), pp. 50–55, 58 [in Russian].
2. A. Gulian, K. Wood, D. Van Vechten, *et al.*, Nucl. Instrum. Methods Phys. Res. A **520**, 36 (2004).
3. V. N. Gurin, L. I. Derkachenko, M. M. Korsukova, *et al.*, Fiz. Tverd. Tela (St. Petersburg) **38**, 2750 (1996) [Phys. Solid State **38**, 1508 (1996)].

Translated by P. Pozdeev

Technical Physics Letters, Vol. 31, No. 9, 2005, pp. 796–798. Translated from Pis'ma v Zhurnal Tekhnicheskoĭ Fiziki, Vol. 31, No. 18, 2005, pp. 66–71.

Estimation of the Computation Capacity of Classical Computers

Yu. N. Zaiko

Volga Region Academy of State Service, Saratov, Russia

e-mail: zyrnick@lycos.com

Received March 1, 2005

Abstract—Calculations performed by a classical (irreversible) computer are described in terms of the Landauer model representing an ensemble of particles in a potential well with two minima separated by a barrier. Evaluation of the computation capacity of a classical computer under the assumption that the switching rate of such devices is exponentially dependent on the dissipated energy leads to a conclusion that contradicts the real situation. In order to eliminate the discrepancy, the system of equations for the populations of the wells is supplemented by an equation for the entropy. Solving this system of equations leads to a power dependence of the switching rate on the dissipated energy, which is confirmed in practice. © *2005 Pleiades Publishing, Inc.*

Classical computers are devices that operate according to the laws of classical physics. Their main feature is the irreversible character of calculations, whereby the input data cannot be reconstructed from the results of calculations. For this reason, the behavior of a classical computer (as well as of any other macroscopic physical system) obeys the second law of thermodynamics according to which the entropy of a closed system in all processes does not decrease with time. Physically, this is related to the dissipation of energy in the course of calculations. Von Neumann [1] suggested that the minimum amount of energy dissipated per computation step is $kT\ln 2$, where k is the Boltzmann constant and T is the absolute temperature of the computational medium. This assumption relates the thermodynamical and logical irreversibility.

Landauer [2] thoroughly considered various models, which represented computational cells as bistable switching devices, and obtained expressions for the switching time that can be naturally considered as a time of the elementary computation step (the processor cycle). One of the most completely analyzed models is a bistable (double) potential well with two minima along one of the coordinates (information degree of freedom). The behavior of an ensemble of particles in such a system is described by the following equation [2]:

$$\frac{dn_A}{dt} = -\nu n_A \exp\left(-\frac{U-U_A}{kT}\right) + \nu n_B \exp\left(-\frac{U-U_B}{kT}\right), \quad (1)$$

where n_A and $n_B = N - n_A$ are the numbers of particles in the potential minima A and B, respectively; N is the total (conserved) number of particles in the cell; ν is the frequency of transitions between the minima; and U, U_A, and U_B are the energies at the maximum (barrier) between the minima and at the potential minima A and B, respectively. The difference $\Delta = (U_A - U_B)/2$ is a half of the energy dissipated in the course of switching, which is supplied by an external force controlling the switching.

Upon switching, the system goes out of the equilibrium characterized by the values $n_A = n_B$ (for $U_A = U_B$) and exhibits relaxation to a new equilibrium distribution:

$$n_A = n_B \exp\left(\frac{U_B - U_A}{kT}\right). \quad (2)$$

This relaxation proceeds according to the exponential law $\sim\exp(-\lambda t)$ with a characteristic time τ, where $\tau^{-1} = |\lambda|$, and λ is the characteristic value of Eq. (1):

$$\lambda = -\nu \exp\left(-\frac{U-U_A}{kT}\right) - \nu \exp\left(-\frac{U-U_B}{kT}\right). \quad (3)$$

Using simple transformations, one can readily show that [2]

$$\frac{1}{\tau} = \frac{1}{\tau_0}\cosh\left(\frac{\Delta}{kT}\right);$$
$$\frac{1}{\tau_0} = 2\nu \exp\left(-\frac{U-U_0}{kT}\right); \quad U_0 = \frac{1}{2}(U_A + U_B), \quad (4)$$

where τ_0 has a meaning of the information lifetime, τ is the switching time defined above, and $\cosh(\Delta/kT)$ is the number of switching events (processor cycles), that is, the program length expressed in processor cycles. Under the condition (usually assumed) that $\Delta \gg kT$, the number of cycles is large, and this fact shows the usefulness of computing devices of this type.

1063-7850/05/3109-0796$26.00 © 2005 Pleiades Publishing, Inc.

The above results are valid under certain conditions, some of which were mentioned above and others were considered by Landauer [2]. One of these assumptions is that the quantities entering into Eqs. (4) can be varied within certain limits, otherwise this relationship would not be so valuable. For example, the value of Δ can change at least severalfold. However, taking this circumstance into account, we come to a contradiction with the commonly accepted point of view that classical computers have insufficient capacity to solve the so-called nonpolynomial problems—the problems whose complexity (measured in terms of the time required for a given program to find a solution) cannot be expressed by any polynomial of the dimensionality of the input data. Examples of such problems are offered by the well-known traveling salesman (shortest route) problem and the problem of long password guessing by the brute force method [3]. The complexity of such problems is evaluated, as a rule, by an exponential function of the input dimensionality—the number of cities to be visited by the salesman or the password length. According to relation (4), the exponential growth of complexity of the problem can be compensated by a similar exponential decrease in the processor cycle time; then, despite exponentially increasing number of instructions (commands), the total time of their execution will remain unchanged.

This circumstance is probably related to the fact that Eq. (1) according to Landauer [2] is solved assuming that the temperature T is constant, whereas the aforementioned energy dissipation must lead to an increase in the temperature in view of the finite heat capacity c of the switching cell. In order to take this fact into account, Eq. (1) should be supplemented with an equation for the entropy S, and the new system of equations should then jointly be solved, which is essentially in the spirit of the Landauer approach. The supplementary equation is as follows:

$$\frac{dS}{dt} = \frac{2\Delta}{T\tau(T)}, \tag{5}$$

where $\tau(T)$ is the temperature-dependent switching time and $2\Delta/T$ is the entropy production per cycle.

The difficulty of the problem under consideration consists in that the exact form of the function $\tau(T)$ at arbitrary temperatures is unknown. For this reason, the consideration will be restricted to the case of small times t, when formula (4) can still be used for $\tau(T)$. Substituting this expression into Eq. (5), taking the integral, and using the formula $dS/dt = (c/T)(dT/dt)$, we obtain a relation for $T(t)$:

$$\exp\left(\frac{E}{kT}\right) = \exp\left(\frac{E}{kT_0}\right) - \alpha t,$$
$$E = U - U_A, \quad \alpha = \frac{2\nu E\Delta}{ckT_0^2}, \quad T_0 = T(0). \tag{6}$$

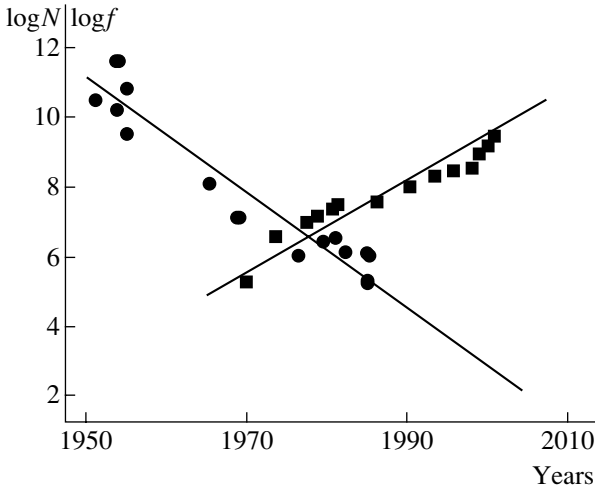

Plots of the number of impurities N in the base of a bipolar transistor (circles, data from [5]) and the CISC processor clock rate f [Hz] (squares, data from [4]) versus year (in cases when several f values were reported [4], $\log f$ was averaged). Straight lines have been drawn to show the trends.

Substituting relation (6) into Eq. (1), we can express $n_A(t)$ as

$$n_A \sim \left|\frac{t'}{\delta_0}\right|^{\frac{\nu}{\alpha}} \exp\left[-\frac{\sigma}{(t')^{\frac{2\Delta}{E}}}\right] + \ldots; \quad t' = t - \frac{1}{\alpha}\exp\left(\frac{E}{kT}\right),$$
$$\delta_0 = \frac{1}{\alpha}, \quad \sigma = \frac{\nu E}{2\Delta\alpha^{1+\frac{2\Delta}{E}}}. \tag{7}$$

Note that expressions (7) describe only the relaxation part of $n_A(t)$.

It turns out that the relaxation of the particle distribution in the potential well to the equilibrium state in the interval of times $t \geq 0$ is described by a power function (rather than by an exponent) and the characteristic time scale $\delta_0 = \delta(T_0) = ckT_0^2/(2\nu E\Delta)$ (which can naturally be considered as the switching time) is also a power function of the dissipated energy 2Δ. This function correctly describes the behavior whereby δ decreases with increasing Δ.

The time scale τ characterizing variation of the power function is determined by its argument and can be evaluated using the derivative $|n_A'| \sim n_A/\tau$. Then, $\tau \approx (\alpha/\nu)|t'|$ and (in the interval of small t under consideration, where $t' \sim -1/\alpha\exp(E/kT)$ we obtain the same formula $\tau = (1/\nu)\exp(E/kT)$ as that used to derive expression (7). However, for other times t, τ will be different, and the use of $\tau(t)$ as a time scale for the relaxation in cases of nonexponential processes such as that described by expression (7) encounters certain prob-

lems. An analysis of these problems, as well as of various $\tau(T)$ dependences, is of independent interest and goes beyond the framework of this study.

The use of δ_0 as a measure of the switching time can be justified using the following considerations. The frequency of switching $f = \alpha$ (processor clock rate) can be evaluated as

$$f = \nu \frac{1}{N} \frac{E}{kT} \frac{2\Delta}{kT}, \quad N = \frac{c}{k}, \quad T \equiv T_0, \tag{8}$$

where N has a meaning of the number of particles (electrons) per cell (transistor). This dependence of f on N has been actually observed, as illustrated in the figure [4, 5]. It should be noted that the number of electrons per transistor was estimated [5] as the number of impurities in the base of a bipolar transistor used for the logical operations. The data for impurities have been extrapolated up to 2010 by Keyes [5]. A comparison of the behavior of N and f shows that the product Nf rather weakly varies with the time. This fact is probably due to a constant level of the material characteristics (ν) and insignificant changes in the characteristics of transistors (E, Δ).

In conclusion, it should be noted that the above considerations reject neither the results obtained in [2] nor the significance of that study, where the question of reversible computations was posed for the first time.

Acknowledgments. The author is grateful to V.V. Popov for fruitful discussions.

This study was supported by the Russian Foundation for Basic Research, project no. 03-02-17219.

REFERENCES

1. J. von Neumann, in *Theory of Self-Reproducing Automata*, Ed. by A. W. Burks (Illinois Univ., Urbana, 1966; Mir, Moscow, 1971).
2. R. Landauer, IBM J. Res. Dev. **5**, 183 (1961).
3. V. M. Bondarev, V. I. Rublinetskiĭ, and E. G. Kachko, *Fundamentals of Programming* (Folio, Kharkov, 1997) [in Russian].
4. V. L. Broĭdo, *Computation Systems, Networks, and Telecommunications* (Piter, St. Petersburg, 2002) [in Russian].
5. R. W. Keyes, IBM J. Res. Dev. **32**, 24 (1988).

Translated by P. Pozdeev

Technical Physics Letters, Vol. 31, No. 9, 2005, pp. 799–801. From Pis'ma v Zhurnal Tekhnicheskoĭ Fiziki, Vol. 31, No. 18, 2005, pp. 72–77.

Interferometer Using a Laser Pointer for Remote Microdisplacement Measurements¶

Zhong Ming Ming, Low Gin Hin, and Gopal M. Hegde*

Electronic and Communication Engineering Division, Ngee Ann Polytechnic, 599489 Singapore

** e-mail: hgm@np.edu.sg; hegopal@rediffmail.com*

Received March 25, 2005

Abstract—A portable Michelson interferometer for remote optical sensing with imaging capability is developed based on a laser pointer and experimentally studied. The setup has an open sensing arm with a mirror that can be attached to any object for the measurement of responses such as microdisplacement, strain, stress, and temperature. A mirror in the reference arm is mounted on an encoded stepper motor, which can operate under remote control via Web/Internet for reset and calibration. Remote microdisplacement measurements precise to within 5 μm have been performed. © *2005 Pleiades Publishing, Inc.*

Introduction. Remote measurement techniques are attractive and effective tools for use in hostile environments and industries, as well as in education and research. Internet facilities and computer-controlled instrumentation allow Web/Internet based techniques to be utilized for setting up distant laboratory access and performing remote online measurements and experiments. Educational laboratories functioning over the Internet have become available at several sites, particularly in the area of electronics and instrumentation engineering [1, 2].

Many remote electronic experiments have already been demonstrated. In recent years, there has been a lot of interest in developing remote photonics experiments. In this respect, interferometry is highly attractive because of a variety of applications. Optical interferometers are frequently used in contactless measurements of physical quantities such as microdisplacements, strain, temperature, and pressure. There have been some reports on remote optical interferometers in the literature [3–6]. A microwave interferometer for remote measurements of building displacements has also been demonstrated [7]. However, none of these systems could be operated or controlled over the Web. The reported interferometers used either He–Ne lasers [3–6] or microwave generators [7] as the probing signal sources.

This paper presents an optical system built around a Michelson interferometer based on a semiconductor laser pointer, which can be operated and controlled over the Web.

System architecture. A block diagram of the proposed remote interferometer system is given in Fig. 1. In this scheme, the remote part (see Fig. 1b) is a personal computer (PC) connected to the Internet and the local part includes the entire interferometer setup and a hosting computer. In our experiments, a laser pointer (AURORA, Model AL31) emitting at a wavelength of 670 nm with a power of 5 mW was used as the light source. Power supply to the laser was tapped from a power slot inside the computer, which made possible the interferometer on/off control via the remote computer.

One (reference) mirror of the Michelson interferometer (Fig. 2) was mounted on a micrometer screw head, which was connected to an encoded stepper motor through a lever. Thus, a motor drive controller circuit

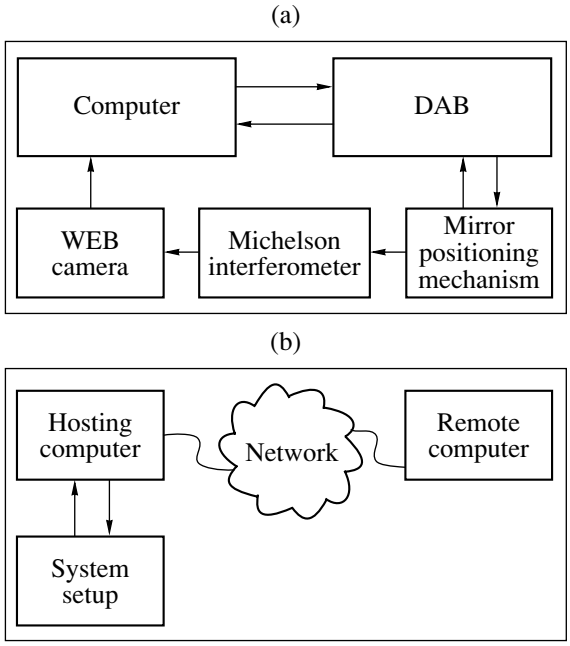

Fig. 1. Schematic diagram of (a) a local system and (b) a remote access system.

¶The text was submitted by the authors in English.

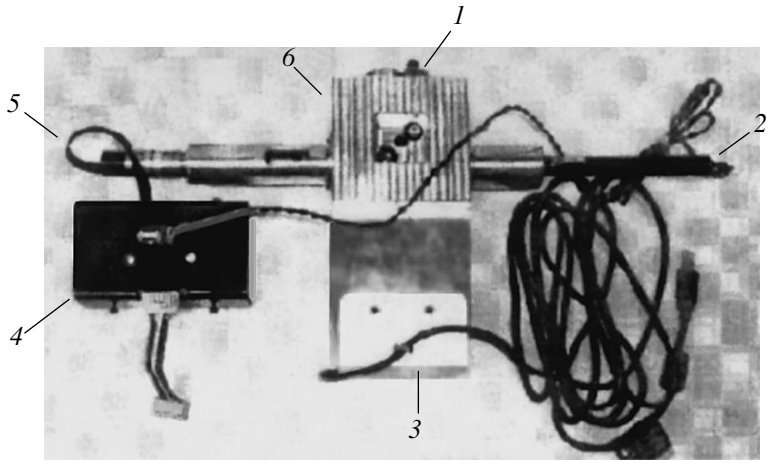

Fig. 2. Compact remote interferometer with control systems: (*1*) open sensing arm; (*2*) laser pointer; (*3*) Web camera unit; (*4*) stepper motor control unit; (*5*) encoded stepper motor; (*6*) interferometer.

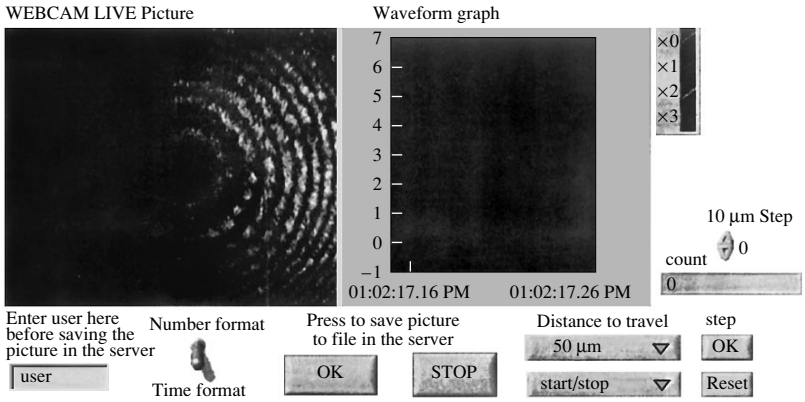

Fig. 3. Control panel and display window on a remote computer.

has been established, which was interfaced with a hosting PC. This arrangement was used to calibrate the instrument and reset the mirror position. A mirror in the sensing arm is connected to the object studied. An additional control interface circuit was built to interface the data acquisition board (DAB) and power supply unit to the laser. This control interface circuit was interconnected to the stepper motor circuit. A Web camera was attached to the setup to observe the interference pattern, which helped to measure and count fringes on the remote computer. This arrangement is also useful for phase shift measurements.

AIM-Lab and LabVIEW are the two frequently used software packages for remote electronic experiments and instrumentation. In our interferometer, we have used LabVIEW 6.1 software from National Instruments, which incorporates Internet communication capabilities and the functions necessary to access and control instruments and to obtain and process the response data. A system control and data acquisition program was also written in LabVIEW 6.1. The user can communicate with the server and the experimental setup using the LabVIEW player. Hence, we can perform the real-time online experiments using this interferometer by means of the Web and a remote PC. The general view of the portable remote interferometer setup with control systems is presented in Fig. 2.

Experimental results. We have successfully used the proposed remote setup in an experiment on real-time online laser coherence length measurements. The moving mirror position was controlled over the Internet, and the corresponding fringe pattern was displayed on a remote PC screen. Figure 3 shows the friendly user control window including remote control function and the interference fringe pattern observation using the LabVIEW software.

Using this remote interferometer, we were able to position the mirror with a 5 μm resolution. The micro-displacement of the object is determined proceeding from the number of pulses necessary to drive the stepper motor so as to compensate the phase shift caused by the object displacement. Figure 4 shows a plot of the measured displacement versus stepper motor pulse

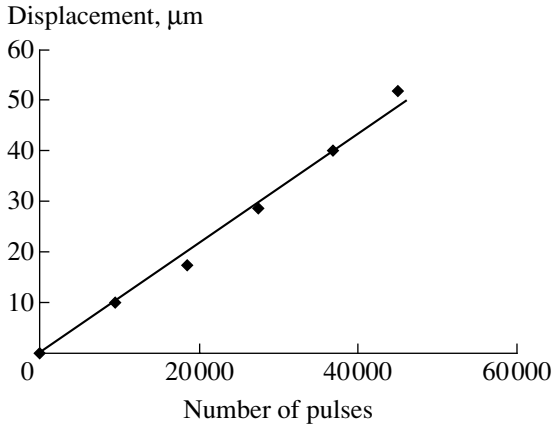

Fig. 4. A plot of the measured displacement versus stepper motor control pulse count.

count. As can be seen, the plot is linear, which confirms a very large dynamic range of the interferometer in remote experiments. We have evaluated the sensitivity of the instrument by inserting a 10-mm-thick glass cell with water of variable temperature into the optical path in the sensing arm. Heating the water caused a considerable phase shift due to a change in the refractive index, and the corresponding fringe counts were monitored on the remote PC display. Using our remote interferometer, we have successfully measured the refractive index. It was found that the instrument was insensitive to external noise.

The proposed instrument can be used as a teaching tool for remote optical experiments. The interferometer can measure microdisplacements in hazard environments in heavy industries. The portable interferometer can also be used for the remote measurement of mechanical strain, microdisplacements, and temperature in laboratories and industries. Introducing a LabVIEW–Web camera software improves the image quality and facilitates remote phase shift measurements. Remote optical sensing is another potential application.

In conclusion, the portable remote interferometer with imaging capability described in this paper is based on a laser pointer and can be easily transported and positioned. The system can be controlled over the Internet and can be used for remote online real-time photomechanical experiments in science, industries, and education. Further work on using this interferometer as a remote senor is in progress and the results will be published elsewhere.

REFERENCES

1. T. A. Fjeldly and M. S. Shur, *Lab on the Web: Running Real Electronics Experiments via the Internet* (Wiley–IEEE, 2003).
2. V. M. Khavinson, in *Proceeding of the 9th IPEF/UMNE-4 Conference, 1997*, pp. 119–122.
3. V. L. Fedorin and V. L. Shur, Izmer. Tekh., No. 9, 34 (1993).
4. O. I. Kotov, L. B. Liokumovich, S. I. Markov, *et al.*, Zh. Tekh. Fiz. **26** (10), 26 (2000) [Tech. Phys. Lett. **26**, 415 (2000)].
5. O. I. Kotov, L. B. Liokumovich, S. I. Markov, *et al.*, in *Proceedings of the 5th International Scientific and Technical Conference on Radiolocation, Navigation and Communications, Voronezh, 1999*, Vol. 3, pp. 1377–1388.
6. A. D. Kersey, Proc. SPIE **1797**, 161 (1993).
7. M. Pieraccini, G. Luzi, D. Mecatti, *et al.*, in *Proceedings of the International Symposium on Non-Destructive Testing in Civil Engineering (NDT-CE) Berlin, 2003.*

Technical Physics Letters, Vol. 31, No. 9, 2005, pp. 802–805. Translated from Pis'ma v Zhurnal Tekhnicheskoĭ Fiziki, Vol. 31, No. 18, 2005, pp. 78–86.

The Magnetic Anisotropy of Thin Epitaxial CrO_2 Films Studied by Ferromagnetic Resonance

B. Z. Rameev[a,b,*], A. Gupta[c], G. Miao[d], G. Xiao[d], F. Yildiz[b], L. R. Tagirov[a,e], and B. Aktaş[b]

[a] *Kazan Physicotechnical Institute, Russian Academy of Sciences, Kazan, Tatarstan, 420029 Russia*
[b] *Gebze Institute of Technology, 41400 Gebze-Kocaeli, Turkey*
[c] *University of Alabama, Tuscaloosa, Alabama 35487, USA*
[d] *Brown University, Providence, Rhode Island 02912, USA*
[e] *Kazan State University, Kazan, Tatarstan, 420008 Russia*
* *e-mail: rameev@gyte.edu.tr*

Received April 5, 2005

Abstract—The magnetic anisotropy of thin epitaxial films of chromium dioxide (CrO_2) has been studied as a function of the film thickness by the ferromagnetic resonance (FMR) technique. CrO_2 films with various thicknesses in the range from 27 to 535 nm have been grown on (100)-oriented TiO_2 substrates by chemical vapor deposition using CrO_3 as a solid precursor. In a series of CrO_2 films grown on the substrates cleaned by etching in a hydrofluoric acid solution, the FMR signal exhibits anisotropy and is strongly dependent on the film thickness. The magnetic properties of CrO_2 films are determined by a competition between the magnetocrystalline and magnetoelastic anisotropy energies, the latter being related to elastic tensile stresses caused by the lattice mismatch between the film and the substrate. In the films of minimum thickness (27 nm), this strain-induced anisotropy is predominant and the easy magnetization axis switches from the [001] crystallographic direction (characteristic of the bulk magnet) to the [010] direction. © *2005 Pleiades Publishing, Inc.*

The development of modern electronics toward the further miniaturization of devices, increasing operation speed, and functional variability implies the use of magnetoelectronic elements whose operation is based on the use of both the charge and spin of conduction electrons. The most important parameter determining the efficiency of such magnetoelectronic elements is the spin polarization of conduction electrons. The ideal materials in this respect are the so-called semimetal ferromagnets, whose unique feature is the completely spin-polarized conduction band. One of these materials is chromium dioxide (CrO_2), in which an extremely high (almost 100%) spin polarization of conduction electrons has been experimentally confirmed [see, e.g., [1, 2]). For this reason, the successful synthesis of thin epitaxial CrO_2 films [3] stabilized by the substrate structure has drawn the attention of researchers to this compound [4–7].

Previously, we studied thin CrO_2 films grown by chemical vapor deposition (CVD) on TiO_2 substrates [8–11]. Based on the results of ferromagnetic resonance (FMR) measurements, we optimized the CVD regimes for chromium dioxide epitaxy (preparation of rutile substrates, substrate temperature during film growth, deposition velocity, etc.). This study was devoted to the FMR measurements in CrO_2 films with reproducible magnetic and structural characteristics obtained using the optimum growth regimes. We have studied the magnetocrystalline and magnetoelastic anisotropy as dependent on the film thickness in a series of samples grown by CVD using CrO_3 as a solid precursor. Using the FMR technique, we have established for the first time that the easy axis in films of minimum thickness (27 nm) exhibits "switching" from *c* to *b* crystallographic direction under the action of the strain-induced anisotropy.

Sample preparation and FMR measurements. Thin epitaxial CrO_2 films were grown by CVD using CrO_3 solid precursor on (100)-oriented TiO_2 single crystal substrates with a rutile structure. The process was essentially the same as that described elsewhere [4]. A series of films with thicknesses of 27, 65, and 434 nm were grown on TiO_2 substrates cleaned by etching in an aqueous hydrofluoric acid (HF) solution. For comparison, we have also grown and studied a film with a thickness of 535 nm grown on the same substrate without preliminary etching.

The orientation of film samples was checked by X-ray diffraction on a Rigaku RINT 2000 diffractometer. The FMR spectra were recorded using an EPR spectrometer of the Bruker EMX type with a working frequency of 9.8 GHz. The FMR investigation was performed according to the standard procedure involving measurements in two geometries: (i) in-plane (whereby

1063-7850/05/3109-0802$26.00 © 2005 Pleiades Publishing, Inc.

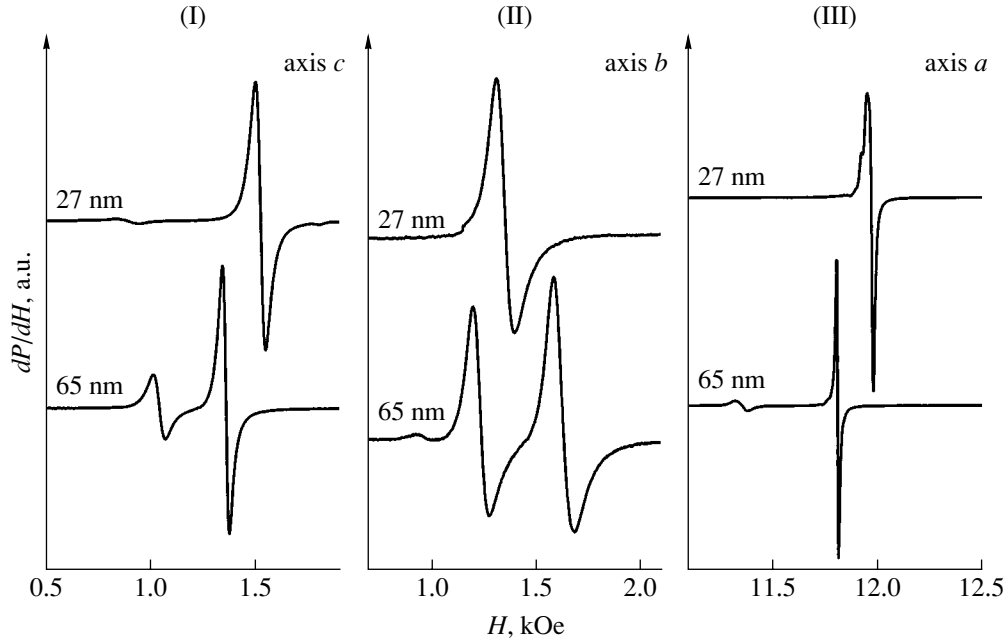

Fig. 1. FMR spectra of 27- and 65-nm-thick CrO_2 films measured with the magnetic field applied (I, II) parallel to the *c* and *b* axes, respectively (in the film plane) and (III) along the *a* axis perpendicular to the film plane.

the external magnetic field is rotated in the sample plane), and (ii) out-of-plane (the magnetic field is rotated in a plane containing the easy axis and the normal to the sample surface).

Experimental results. Figure 1 shows the FMR spectra of thin epitaxial CrO_2 films (27 and 65 nm thick) grown on etched Ti_2 substrates and measured in the in-plane and out-of-plane geometry. The spectrum of a film from the same series with a thickness of 434 nm exhibits splitting into several components, whereas the spectrum of a film grown on the unetched substrate exhibits a single FMR mode signal. Figure 2 shows the angular variation of the resonance field amplitude for all samples (except for the 434-nm-thick film on the etched substrate) measured in both the in-plane and out-of-plane geometry.

As can be seen from Figs. 1 and 2, the results of FMR measurements in the out-of-plane geometry reveal the typical angular dependence with the predominating effect of the demagnetizing field (shape anisotropy), whereby the easy axis occurs in the plane of the CrO_2 film. At the same time, the spectra measured in the in-plane geometry revealed a strong influence of the magnetocrystalline anisotropy. The maximum and minimum values of the resonance field correspond to the hard and easy magnetization axes, respectively.

The FMR spectrum measured in the in-plane geometry for a 535-nm-thick film grown on the unetched substrate exhibits the maximum (among the series of samples studied) anisotropy in the film plane. Apparently, the easy magnetization direction in this film corresponds to the *c* axis ([001] direction) of the crystal structure. A similar behavior was observed for the thickest (434 nm) film in the series of samples grown on the etched substrates, but the degree of anisotropy was somewhat lower. As for the 65- and 27-nm-thick films, their magnetic anisotropy was much less pronounced (Fig. 2), and the film of minimum thickness (27 nm) was characterized by a minimum resonance field for the *b* axis ([010] direction) of the crystal structure. Thus, the easy axis exhibits switching from *c* to *b* direction, in agreement with the results of static magnetic measurements [12]. The FMR measurements performed for a film of the intermediate thickness (65 nm) grown on the

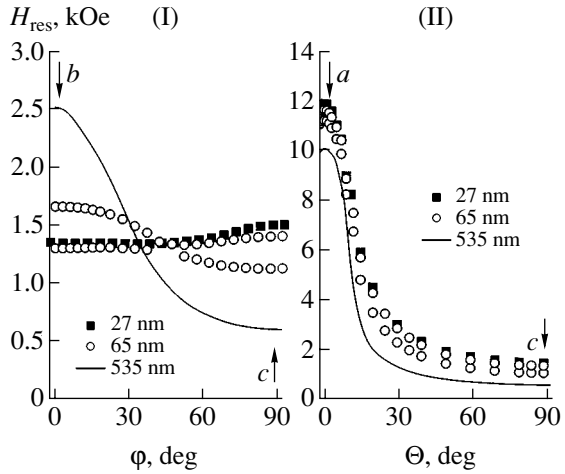

Fig. 2. Experimental angular dependences of the resonance field for CrO_2 films of various thicknesses measured in the (I) in-plane and (II) out-of-plane geometry.

unetched substrate (Fig. 2) showed an unusual angular dependence with the antiphase behavior of the main FMR modes: the minimum resonance field of the first mode corresponds to the maximum field for the second mode and vice versa. This behavior implies the existence of two magnetic phases with mutually perpendicular easy axes oriented in the [001] and [010] crystallographic directions.

Discussion. As is known, both the epitaxial CrO_2 film and the single crystal TiO_2(100) substrate possess a tetragonal rutile structure [3, 4, 6]. The lattice mismatch between the CrO_2 film and the TiO_2 substrate amounts to –3.79% in the [010] direction (*b* axis) and –1.48% in the [001] direction (*c* axis). This lattice mismatch results in the appearance of an anisotropic strain in the CrO_2 film plane [3]. The undistorted structure of chromium dioxide is characterized by a tetragonal magnetocrystalline anisotropy with an easy axis parallel to the *c* axis. The stress related to the lattice mismatch between the film and the substrate leads to the appearance of an additional, magnetoelastic contribution to the anisotropy. Thus, the magnetic anisotropy energy can be expressed as

$$E_{\text{ani}} = K_1 \sin^2\theta + K_2 \sin^4\theta + K_\sigma \sin^2(\theta - \delta), \quad (1)$$

where θ is the angle between the magnetization **M** and the *c* axis of the CrO_2 crystal, K_i is the crystal anisotropy parameter, K_σ is the magnetoelastic anisotropy, and δ is the angle between the *c* axis and the strain direction in the film plane [3, 6, 7].

The FMR spectrum of a CrO_2 film on the unetched substrate is the most simple for interpretation because the X-ray diffraction data [13] show that such films are virtually free from deformations and, hence, the last term in Eq. (1) can be ignored. The results of computer simulations of the resonance fields in both standard geometries gave the anisotropy fields $K_1/M_s = 510$ Oe and $K_2/M_s \sim 0$ Oe at a saturation magnetization of $M_s = 470$ Oe. These values are in very good agreement with the published data for bulk CrO_2 crystals [14] and single crystal CrO_2 films [3, 6].

The FMR spectra of the films grown on etched substrates show that these films are strained to a considerable extent because of a lattice mismatch between the CrO_2 epitaxial film and the single crystal substrate. As a result, the strained film features a competition between the energies of magnetocrystalline and magnetoelastic anisotropy, whose easy axes coincide with the [001] and [010] directions, respectively. As for the different FMR modes observed in the 65- and 434-nm-thick films, this behavior probably reflects inhomogeneity in the distribution of strain in the film plane.

An analysis of the angular dependences of the resonance field in the in-plane and out-of plane geometries shows that the contribution of the magnetoelastic anisotropy can be correctly described in terms of a simplified model,

$$E_{\text{ani}} = K_{1\text{eff}} \sin^2\theta + K_2 \sin^4\theta, \quad (2)$$

where a single parameter $K_{1\text{eff}}$ is used to take into account the quadratic terms of the magnetocrystalline and magnetoelastic anisotropy (the first and third terms in Eq. (1), respectively). In this model, the easy axis of the magnetoelastic anisotropy is oriented at an angle of $\delta = 90°$ relative to the *c* axis, that is, parallel to the *b* axis of the rutile structure as it was observed in [3]. The coefficient $K_{1\text{eff}}$ decreases with the film thickness and even becomes negative for the thinnest (27-nm-thick) film in a series with the strain-induced anisotropy. Numerical simulation yields –60 Oe for the effective anisotropy field $K_{1\text{eff}}/M_s = (K_1 - K_\sigma)/M_s$. It should be noted that the experimental angular dependence of the resonance field observed for the 27-nm-thick film can be reproduced by modeling only with allowance for the parameter K_2 at the fourth-order term of magnetocrystalline anisotropy. The best agreement was obtained for $K_2/M_s = 25$ Oe.

In considering the results of the FMR measurements performed in the out-of-plane geometry (Fig. 2(II)), it is necessary to point out an increase in the maximum resonance field in the thinnest films, which reflects a contribution of the out-of-plane anisotropy. This influence is manifested in the results of numerical modeling by an increase in the effective magnetization, which can be expressed as $M_{\text{eff}} = M_s - K_\perp/2\pi M_s$, where M_s is the room-temperature saturation magnetization and $K_\perp$, the strain-induced out-of-plane anisotropy. The appearance of an additional out-of-plane anisotropy with the asymmetry axis oriented in the normal direction is related to the fact that the tensile stress in the film plane produces a compensating compressive stress in the transverse direction perpendicular to the film plane. The negative sign of the out-of-plane anisotropy $K_\perp$ (which implies an increase in M_{eff}) indicates that the hard magnetization axis is also perpendicular to the CrO_2 film plane.

Conclusions. The results of our FMR investigation of the magnetic properties of thin epitaxial CrO_2 films by the FMT techniques showed that

(i) a lattice mismatch between the CrO_2 films and TiO_2 substrates gives rise to anisotropic elastic tensile stresses, which strongly influence the magnetic anisotropy parameters and even lead to switching of the easy axis from the *c* to the *b* direction in the thinnest (27-nm-thick) film;

(ii) the inhomogeneous character of the magnetoelastic anisotropy in CrO_2 films of an intermediate thickness (~65 nm) is manifested by the coexistence of two magnetic phases with mutually perpendicular easy axes in the [001] and [010] crystal directions;

(iii) by changing the conditions of synthesis, it is possible to control the magnetic anisotropy within

broad limits and to obtain thin CrO_2 films with desired magnetic parameters, which is of considerable importance for the possible applications of such films in magnetoelectronics.

Acknowledgments. This study was supported in part by the Gebze Institute of Technology (grant no. 2003-A-15). One of the authors (L.R.T.) also gratefully acknowledges the support from BRHE (grant REC-007).

REFERENCES

1. Y. Ji, G. J. Strijkers, F. Y. Yang, *et al.*, Phys. Rev. Lett. **86**, 5585 (2001).
2. A. Anguelouch, A. Gupta, G. Xiao, *et al.*, Phys. Rev. B **64**, 180408 (2001).
3. X. W. Li, A. Gupta, and G. Xiao, Appl. Phys. Lett. **75**, 713 (1999).
4. X. W. Li, A. Gupta, T. R. McGuire, *et al.*, J. Appl. Phys. **85**, 5585 (1999).
5. A. Gupta and J. Z. Sun, J. Magn. Magn. Mater. **200**, 24 (1999).
6. F. Y. Yang, C. L. Chien, E. F. Ferrari, *et al.*, Appl. Phys. Lett. **77**, 286 (2000).
7. L. Spinu, H. Srikanth, A. Gupta, *et al.*, Phys. Rev. B **62**, 8931 (2000).
8. B. Z. Rameev, R. Yilgin, B. Aktaş, *et al.*, Microelectron. Eng. **69**, 336 (2003).
9. B. Z. Rameev, B. Aktaş, A. Gupta, *et al.*, in *NATO Science Series II: Mathematics, Physics and Chemistry*, Ed. by B. Aktaş, L. R. Tagirov, and F. Mikailov (Kluwer, Boston, 2004), Vol. 143, pp. 273–282.
10. B. Z. Rameev, A. Gupta, A. Anguelouch, *et al.*, J. Magn. Magn. Mater. **272**, 1167 (2004).
11. B. Z. Rameev, A. Gupta, G. X. Miao, *et al.*, Phys. Status Solidi A **201**, 3350 (2004).
12. G. Miao, G. Xiao, and A. Gupta, Phys. Rev. B **71**, 064407 (2005).
13. A. Gupta, private communication.
14. D. S. Rodbell, J. Phys. Soc. Jpn. **21**, 1224 (1966).

Translated by P. Pozdeev

Technical Physics Letters, Vol. 31, No. 9, 2005, pp. 806–809. Translated from Pis'ma v Zhurnal Tekhnicheskoĭ Fiziki, Vol. 31, No. 18, 2005, pp. 87–94.

Criteria of the Thermal State of a Hot Cathode

B. D. Tsydypov

Department for Physical Problems, Presidium of the Buryatian Scientific Center, Siberian Division, Russian Academy of Sciences, Ulan-Ude, Buryatia, Russia

e-mail: imf@ofpsrv.bsc.buryatia.ru

Received May 11, 2005

Abstract—Criteria characterizing the contributions of the main energy sources and sinks to the complex process of heat exchange in thermionic rod cathodes of low-temperature plasma generators are determined within the framework of a quasi-one-dimensional model. Using relations between these criteria, it is possible to evaluate various thermal regimes of operation of long high-current cathodes. A method for the optimization of the thermal state of such electrodes is developed. The results of calculations according to the proposed scheme agree with experimental data. © *2005 Pleiades Publishing, Inc.*

Cathode units of plasma generators with high-current thermionic cathodes operate under conditions of extremely intense heat fluxes and load currents. The thermal state of this unit and the erosion resistance of a cathode determine the operation characteristics and working life of the entire plasma system [1–4]. However, the calculation and optimization of the thermal regime of a cathode unit encounter considerable difficulties related to meeting the high requirements to thermal contacts at the joints of various metals (possessing different thermal, electrical, and mechanical properties), selecting the optimum geometry, and providing for an effective heat exchange in the system [4, 5].

The typical scheme of a thermionic rod cathode unit used in low-temperature plasma generators is depicted in the figure. The most effective cathode units for high-current plasmatrons employ an assembly comprising insert I (a rod electrode made of activated tungsten) pressed into water-cooled sleeve II (a cylindrical holder made of copper) [6]. The cathode protrusion length L_c can be varied from $L_c = 0$ to $L_c/d_1 \geqslant 1$ (long cathode), where d_1 is the rod diameter. The working edge of the rod ($z = 0$) receives a thermal flux within a spot of radius r_0, which represents the thermal action q_0 of the discharge plasma III. Behind the cathode spot, the bulk metals and the cylindrical surfaces of the electrode and holder exhibit convective and radiative heat exchange with the working (protective and plasma-forming) gas V and the environment (coolant IV).

The thermal problem for a cathode unit of the typical design described above reduces to a nonstationary heat conduction equation with nonlinear boundary conditions in the two-dimensional insert–sleeve system [5, 7]:

$$c\rho\frac{\partial T}{\partial t} = \mathrm{div}(\lambda \mathrm{grad} T) + q_v. \qquad (1)$$

Here, T is the absolute temperature, c is the specific heat, ρ is the material density, λ is the thermal conductivity, and q_v is the volume density of internal heat sources and sinks related to various physicochemical processes of energy evolution and absorption. Calculations performed within the framework of a nonstationary model of cathode and near-cathode processes are aimed at determining the thermal state of the electrode unit corresponding to the maximum working life under preset external conditions.

In many cases of practical importance, it is expedient to consider simplified problems formulated by separating the main thermal factors. For example, the thermal state of a long rod cathode ($L_c/d_1 \geqslant 1$) can be determined within the framework of a quasi-one-dimensional model [8]. In this case, the influence of the massive cooled sleeve on the temperature field in the insert is weak and can be replaced by a boundary condition of the first kind, while the complicated heat exchange at the side surface of the electrode is

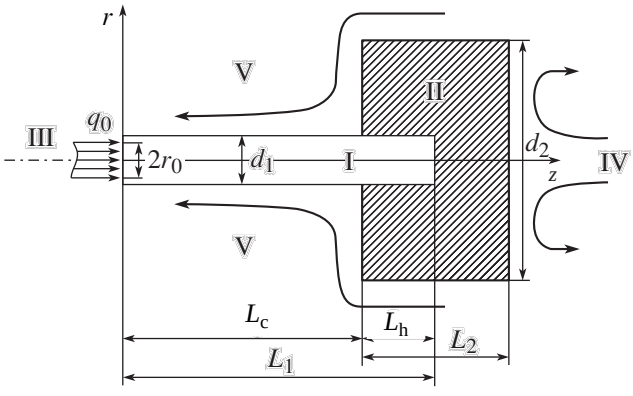

The model of a thermionic cathode unit: (I) cathode insert; (II) holder sleeve; (III) discharge plasma; (IV) cooling water; (V) working gas.

1063-7850/05/3109-0806$26.00 © 2005 Pleiades Publishing, Inc.

described by terms representing the so-called effective volume sources and sinks of energy in the one-dimensional heat conduction equation. This approximation is applicable to cathodes operating under conditions of a diffuse discharge with high load currents, when the contact area is close to the electrode cross section ($2r_0 \approx d_1$ in the figure) and the temperature variation in the radial direction can be ignored.

In the proposed quasi-one-dimensional model, Eq. (1) for insert I can be written as

$$c_1\rho_1\frac{\partial T}{\partial t} = \frac{\partial}{\partial z}\left[\lambda_1(T)\frac{\partial T}{\partial z}\right] - \frac{2\alpha(T)}{r_1}(T - T_g) - \frac{2\varepsilon(T)\sigma_B}{r_1}(T^4 - T_m^4) + j_1^2/\sigma_1(T), \quad (2)$$

where $\alpha(T)$ is the convective heat transfer coefficient, $\varepsilon(T)$ is the integral emissive power, σ_B is the Stefan–Boltzmann constant, and T_g and T_m are the temperatures of the working gas and ambient medium, respectively.

Steady-state thermal regimes are described by numerically solving the stationary heat conduction equation by the standard Runge–Kutta iteration technique for the known (experimentally determined) temperature profile $T(z)$ along the cathode with the corresponding boundary conditions [1, 9]:

$$T(z_1) = T_1, \quad T(z_2) = T_2.$$

The second boundary condition can be satisfied by varying the heat flux z_1 in the input cross section and assuming that $T_g = T_m = 300$ K.

Using the quasi-one-dimensional model, it is possible to optimize the temperature regime of the cathode and determine the contribution of each term in Eq. (2) to the overall energy balance [1, 9]. However, such optimization requires joint calculations and experimental investigations, which cannot always be realized in practice. The optimum thermal regime of a thermionic cathode can be found and its energy balance can be evaluated using the following rational scheme.

Assuming that all coefficients in Eq. (2) are constant and omitting the lower indices, this equation can be reduced to a dimensionless form as

$$\frac{\partial\tilde{T}}{\partial\tau} = Fo\frac{\partial^2\tilde{T}}{\partial\tilde{z}^2} - B(\tilde{T} - 1) - C(\tilde{T}^4 - 1) + G\tilde{j}^2, \quad (3)$$

where $Fo = \lambda\tau_0/(c\rho l^2)$ is the Fourier number; $B = 2\alpha\tau_0/(c\rho r)$, $C = 2\varepsilon\sigma_B\tau_0 T_c^3/(c\rho r)$, $G = j_0^2\tau_0/(c\rho\sigma T_c)$; $\tilde{T} = T/T_c$ is the relative temperature; $\tilde{j} = j/j_0$ is the relative current density; $\tau = t/\tau_0$ and $\tilde{z} = z/l$ are the dimensionless time and coordinate, respectively; τ_0 and l are the corresponding scales; $T_g = T_m = T_c$ is the characteristic temperature; and j_0 is the characteristic current density in the cathode.

The contributions of various components to the energy balance can be evaluated by comparing the dimensionless parameters Fo, B, C, and G in Eq. (3). Zimin *et al.* [10] considered the ratio $\theta = Fo/C$ to be a criterion reflecting the efficiency of heat removal by conduction relative to the Joule's heat evolution. Rewriting this criterion as $\theta = \dfrac{\lambda T_c/l}{j_0^2 l/\sigma}$, we can see that the numerator $\lambda T_c/l$ describes the conductive heat flux carried away from the cathode at $T_0 = 0$, while the denominator $j_0^2 l/\sigma$ is the effective incoming heat flux due to Joule's heating of the cathode. By analogy, we can also introduce the criteria

$$\chi = \frac{B}{G} = \frac{2\alpha T_c/r}{j_0^2 l/\sigma}, \quad \eta = \frac{C}{G} = \frac{2\varepsilon\sigma_B T_c^4/r}{j_0^2 l/\sigma},$$

which describe the efficiency of the convective (χ) and radiative (η) heat fluxes out of the cathode relative to the Joule's heat evolution.

In the quasi-one-dimensional approach, the above criteria can be interpreted in terms of volume processes. The energy balance for a thermionic cathode can be expressed in terms of the effective volume heat fluxes:

$$q_0 + q_1 - q_2 - q_3 - q_4 = 0, \quad (4)$$

where q_0 and q_1 are the volume heat sources representing the thermal action of the discharge plasma and the Joule's heat evolution, respectively; and q_2, q_3, and q_4 are the heat fluxes carried away by means of the conductive, convective, and radiative heat transfer, respectively.

Depending on the load current (i.e., on the Joule's heating power), a thermionic cathode can feature the following thermal situations [4]: $q_0 > 0$, $q_0 = 0$, and $q_0 < 0$.

Let us consider these cases separately for the quasi-one-dimensional model in the order of increasing load current.

Case 1: $q_0 > 0$, so that $q_2 + q_3 + q_4 > q_1$. In terms of the criteria introduced above, this condition can be expressed as $\theta + \chi + \eta > 1$, or, denoting the sum of three criteria by ξ, as $\xi > 1$. This condition shows the relation between the main volume heat sinks and the Joule's heat evolved and dissipated in the cathode. At a small load current, the relative contribution of Joule's heat to the energy balance is not large and $q_0 > 0$. In this situation, the main source heating the metal is a heat flux from the discharge plasma.

Dependence of the thermal regime criteria on the cathode length

L_1, cm	3	4	5	6	7	8	9
θ	1.93	1.08	0.69	0.48	0.35	0.27	0.21
ξ	2.67	1.82	1.43	1.22	1.09	1.01	0.95

Case 2: $q_0 = 0$, so that $q_2 + q_3 + q_4 = q_1$ or $\theta + \chi + \eta = \xi = 1$. This situation corresponds to the optimum thermal regime, whereby the thermal action of the discharge plasma (including ion bombardment, conductive and radiative components) is fully compensated by the flux of energy carried away by electron emission, evaporated metal atoms, and radiative heat transfer [11], so that a dynamic equilibrium is established between various competitive processes. The condition $\xi = 1$ corresponds to a correct choice of the characteristic parameters and scales in Eq. (3), ensuring the optimum thermal regime of cathode operation.

Case 3: $q_0 < 0$, so that $q_2 + q_3 + q_4 < q_1$ or $\theta + \chi + \eta = \xi < 1$. In this case, the thermal state of the cathode corresponds to the so-called Joule's overheating [3]. A special feature of this regime is that the temperature profile $T(z)$ becomes nonmonotonic because of a high power of the Joule's heating, so that the derivative $\partial T(z)/\partial z$ near the hot cathode edge becomes negative. In high-current cathodes of melting plasmatrons, the temperature field at the hot cathode edge is also nonmonotonic in the radial direction [12].

Thus, by comparing the introduced criteria, it is possible to evaluate the energy balance and establish the thermal regime of cathode operation. Note that, in addition to the θ criterion introduced previously [10], it is necessary to use the other criteria defined above.

From a practical standpoint, it is of interest to consider the optimum temperature regime corresponding to $\xi = 1$. Let us determine the characteristic values of parameters entering into the above criteria for this regime of cathode operation. The choice of the characteristic current density $j_0 = I/(\pi r_1^2)$ for long cathodes seems to be well justified. The optimum choice of a characteristic temperature T_c for the complicated heat exchange in the heated solid–working gas–ambient medium system is offered by the average cathode temperature. In the general case, calculations of this temperature using the formula $T_c = \frac{1}{F}\int_F T\,dF$ require a knowledge of the temperature distribution over the cathode surface F, which implies the need for experimental measurements of the $T(z)$ profile. However, the average cathode temperature can be estimated proceeding from the well-known fact that the $T(z)$ profile of a long rod cathode operating in the optimum current regime is described by a nearly linear function [5, 11, 14]. Then, the average temperature can be calculated as $T_c = (T_0 + T_1)/2$, where T_0 and T_1 are the temperatures of the cold and hot electrode ends. The temperature of the water-cooled cold end is $T_0 = 300$ K. The hot end temperature can be determined as follows. For a rod thermionic cathode with known geometry, the optimum working current (in amperes) obeys an empirical relation [14]

$$I_{opt} = 12d^2, \tag{5}$$

where d is the electrode diameter in millimeters; the corresponding optimum current density is $j_0 = 4I_{opt}/(\pi d^2)$. Then, the hot end temperature T_1 can be determined by assuming that the cathode current in the optimum regime is completely due to the thermoemission ($j_0 = j_e$) and using the Richardson–Dushman formula

$$j_e = AT_1^2 \exp[e\varphi/(kT_1)], \tag{6}$$

where j_e is the thermoemission current density, A is the Richardson constant, $e\varphi$ is the cathode surface work function, and k is the Boltzmann constant.

This procedure can be illustrated by the following example. Consider a cylindrical cathode of lanthanum-doped tungsten (VL-30 alloy) with a radius of $r_1 = 0.25$ cm and a length of $L_1 = 3$ cm operating in argon at atmospheric pressure [7, 14]. The optimum current according to formula (5) is $I_{opt} = 300$ A, and the optimum current density is $j_0 = I_{opt}/(\pi r_1^2) = 1.53 \times 10^3$ A/cm^2. The calculation of T_1 according to formula (6) can be simplified using $j_e(e\varphi, T)$ nomograms [3]. The VL-30 cathode with a work function of $e\varphi = 3.0$ eV operating at the optimum current density has an emission (hot end) temperature of $T_1 \approx 2900$ K. Thus, the characteristic temperature for this cathode is $T_c = (T_0 + T_1)/2 = 2600$ K. The thermal and electrical characteristics at this temperature are as follows [5]: $\lambda = 1.09$ W/(cm K); $\sigma^{-1} = 42.7$ μΩ cm; and $\varepsilon = 0.207$. The coefficient α strongly depends on the conditions of plasma device operation and may vary within broad limits, from 4×10^{-5} to 3.7×10^{-2} W/(cm^2 K) [15]. For this calculation, we use the average value of $\alpha = 10^{-3}$ W/(cm^2 K). It should be noted that the values of α in widely used plasma devices, such as melting and welding plasmatrons, are relatively small and the convective components of the energy exchange in thermionic rod cathodes can be ignored [14].

The values of the criteria θ and ξ for various cathode lengths L_1 at a fixed cathode radius $r_1 = 0.25$ are presented in the table (the criteria related to the cathode radius are also constant: $\chi = 0.61$ and $\eta = 0.13$). The optimum thermal regime at a current of $I = 300$ A is realized for a cathode with $L_1 = 7$–9 cm (depending on the depth L_h of electrode insertion into the holder

sleeve) and $L_c \sim 6$ cm. These results well agree with the experimental data reported in [1, 11].

As the cathode length L_1 is decreased, the optimum current I_{opt} grows and the error of calculations using formula (5) increases. Experiments showed that, for the cathode with $L_1 = 3$ cm, the optimum current amounts to 350 A [14]. The optimum current density for $r_0 = r_1$ is 1.79×10^3 A/cm^2, which correspond to the overstated criteria: $\theta = 1.41$, $\chi = 0.43$, and $\eta = 0.08$, so that $\xi = 1.92$. The discrepancy is explained by the fact that the discharge in cathodes with a relatively small protrusion length L_c is more contracted and $r_1 > r_0$, which implies the need for a more precise determination of the r_0 and j_0 values. Indeed, calculations performed for this cathode within the framework of a closed nonstationary model [7] yield an optimum current of 350 A at $j_0 = 2.53 \times 10^3$ A/cm^2, $r_0 = 0.21$ cm, and $T_1 = 2860$ K. Substituting these values into the expressions for the criteria, we obtain $\theta = 0.71$, $\chi = 0.22$, and $\eta = 0.04$, which yields $\xi = 0.97$, in agreement with the optimum thermal state of the electrode.

Thus, the numerical examples demonstrate the correctness of the proposed approach to optimization of the thermal regime and evaluation of the energy exchange components using the introduced criteria for long ($L_c/d_1 \gg 1$) rod high-current cathodes.

REFERENCES

1. M. F. Zhukov, A. S. An'shakov, and G.-N. B. Dandaron, in *Near-Electrode Processes and Electrode Erosion in Plasmatrons* (Institute of Thermophysics, Acad. Sci. USSR, Novosibirsk, 1977), pp. 61–84 [in Russian].
2. V. E. Korsukov, P. V. Patrievskiĭ, F. G. Rutberg, *et al.*, Zh. Tekh. Fiz. **56**, 1724 (1986) [Sov. Phys. Tech. Phys. **31**, 1026 (1986)].
3. V. F. Gordeev and A. V. Pustogarov, *Thermionic Arc Cathodes* (Énergoizdat, Moscow, 1988) [in Russian].
4. G. A. Dyuzhev, A. M. Zimin, and V. I. Khvesyuk, *Plasma Accelerators and Ion Injectors* (Nauka, Moscow, 1984), pp. 200–217 [in Russian].
5. *Theory and Calculation of Near-Electrode Processes*, Ed. by I. G. Panevin and V. I. Khvesyuk (Nauka, Novosibirsk, 1992) [in Russian].
6. *Encyclopedia of Low-Temperature Plasma*, Ed. by V. E. Fortov (Nauka, Moscow, 2000), Introductory Volume 2, pp. 280–328 [in Russian].
7. B. D. Tsydypov, *Dynamics of Nonstationary Processes in High-Current Plasma Systems* (Buryatian Scientific Center, Russian Academy of Sciences, Ulan-Ude, 2002) [in Russian].
8. H. Hugel and G. Krulle, Beitr. Plasmaphys. **9** (2), 87 (1969).
9. A. V. Pustogarov, A. N. Kolesnichenko, B. S. Gavryushenko, *et al.*, Teplofiz. Vys. Temp. **11** (11), 174 (1973).
10. A. M. Zimin, N. P. Kozlov, and V. I. Khvesyuk, Izv. Sib. Otd. Akad. Nauk SSSR, Ser. Tekhn. Nauk, No. 3 (1), 9 (1979).
11. M. F. Zhukov, N. P. Kozlov, A. V. Pustogarov, *et al.*, *Near-Electrode Processes in Arc Discharges* (Nauka, Novosibirsk, 1982) [in Russian].
12. V. S. Bortnichuk and M. M. Krutyanskiĭ, *Plasma-Arc Melting Furnace* (Énergoizdat, Moscow, 1981) [in Russian].
13. A. S. Telegin, V. S. Shvydskiĭ, and Yu. G. Yaroshenko, *Heat and Mass Transfer* (Akademkniga, Moscow, 2002) [in Russian].
14. A. S. An'shakov, E. K. Urbakh, and B. D. Tsydypov, Teplofiz. Aéromekh. **2** (2), 167 (1995).
15. M. F. Zhukov and V. S. Nikiforovskiĭ, *Experimental Studies of Plasmatrons* (Nauka, Novosibirsk, 1977), pp. 292–314 [in Russian].

Translated by P. Pozdeev